Lehrstuhl für Biomedizinische Physik
Technische Universität München

X-ray Vector Radiography for Biomedical Applications

Christoph Jud

December 2018

Supervisor:
Prof. Dr. Franz Pfeiffer

Technische Universität München

Technische Universität München
Physik Department
Lehrstuhl für Biomedizinische Physik

X-ray Vector Radiography for Biomedical Applications

Christoph Jud

Vollständiger Abdruck der von der Fakultät für Physik der Technischen Universität München zur Erlangung des akademischen Grades eines

Doktors der Naturwissenschaften (Dr. rer. nat.)

genehmigten Dissertation.

Vorsitzender:	Prof. Dr. Martin Zacharias
Prüfer der Dissertation:	1. Prof. Dr. Franz Pfeiffer
	2. Priv.-Doz. Dr. Tobias Lasser

Die Dissertation wurde am 23.01.2019 bei der Technischen Universität München eingereicht und durch die Fakultät für Physik am 04.03.2019 angenommen.

Abstract

X-rays can deeply penetrate matter, only a certain part of them is absorbed or scattered. The attenuation processes are well-known, the corresponding imaging techniques provide a cornerstone in clinical diagnostics nowadays. Grating-based interferometry provides differential phase-contrast and dark-field contrast in addition to the attenuation signal. The dark-field is strongly related to small-angle scattering and hence sensitive to gradients in electron density. A change in the scattering signal thus can be related to morphological changes without the need to directly resolve them. Dark-field imaging mainly detects scattering in one distinct sensitivity direction, which can be utilized to gain directional scattering information. In projection geometry, x-ray vector radiography (XVR) has been established as a method to measure the mean scattering, anisotropy, and orientation of scattering structures.

The first part of this thesis investigates XVR as a tool to detect bone microstructures. We demonstrate that the method is suitable for extended samples in a realistic setting by measuring a human cadaver hand. The scattering anisotropy is employed to detect changes in the trabecular microstructure which are not visible in the corresponding attenuation signal. On the basis of an *ex-vivo* porcine rib model, the influence of microfractures on the scattering properties is investigated. In a proof of principle study, radiographically occult microfractures are detected by means of an increased mean scattering signal. The second part of this thesis aims to improve the diagnosis of cracked tooth syndrome. X-ray Dark-Field Tomography is used to reconstruct the mean scattering signal in three dimensions. This makes it possible to indirectly detect microcracks teeth which are not visible in conventional imaging.

Zusammenfassung

Röntgenstrahlen können Materie leicht durchdringen, wobei ein Teil von ihnen absorbiert oder gestreut wird. Bildgebung auf Basis der Abschwächung von Röntgenstrahlen ist sehr gut verstanden und bildet heutzutage einen Grundpfeiler der klinischen Diagnostik. Gitterbasierter Phasenkontrast ermöglicht es, zusätzlich zur Abschwächung, den differentiellen Phasenkontrast und das Dunkelfeld-Signal zu detektieren. Letzteres ist sensitiv auf Röntgen-Kleinwinkelstreuung und damit auf Gradienten in der Elektronendichte. Eine Veränderung des Streusignals ist deshalb ein Hinweis auf morphologische Veränderungen, wobei diese allerdings nicht räumlich aufgelöst werden müssen. Da hauptsächlich Streuung in eine spezielle Sensitivitätsrichtung detektiert wird, kann die Richtungsabhängigkeit des Streusignals als zusätzliche Informationsquelle benutzt werden. Basierend auf dieser Information wurde die Röntgen-Vektorradiographie (XVR) entwickelt, um die mittlere Streuung, deren Anisotropie und die Richtung von streuenden Strukturen in Projektionen zu detektieren.

Im ersten Teil dieser Dissertation wird die Eignung von XVR für die Detektion von Knochenmikrostrukturen untersucht. Anhand der Messung einer *ex-vivo* menschlichen Hand wird gezeigt, dass die Methode für ausgedehnte Proben in einem klinisch relevantem Umfeld geeignet ist. Mithilfe der Anisotropie werden Unterschiede in der trabekulären Mikrostruktur festgestellt, die in der Abschwächung nicht sichtbar sind. Darüber hinaus wird anhand eines *ex-vivo* Modells von Schweinerippen gezeigt, dass okkulte Mikrofrakturen durch ein erhöhtes mittleres Streusignal detektiert werden können. Der zweite Teil beschäftigt sich mit der Detektion von feinen Rissen in Zähnen. Röntgen-Dunkelfeldtomographie wird dabei angewandt um das mittlere Streusignal in drei Dimensionen zu rekonstruieren. Da im Gegensatz zu einer konventionellen Tomographie die Risse nicht direkt aufgelöst werden müssen, können selbst feinste Risse in Zähnen sichtbar gemacht werden.

Contents

1 Introduction

The discovery of x-rays was without a doubt one of the most outstanding events in the 19^{th} century. Although they have been produced and even detected before, Wilhelm Conrad Röntgen was the first one to recognize x-rays and their ability to penetrate matter in late 1895. He immediately pointed out their importance for medical imaging and was awarded the very first Nobel prize in physics [Nobel Prize, 1901]. In 1912, diffraction patterns were observed by Laue which provided strong evidence that x-rays are electromagnetic waves. One year later, these discoveries led to the detection of crystalline structures by Bragg and hence to the foundation of crystallography. The possibility to observe structures on an atomic level gave the final clue for the DNA double helix structure, one of the biggest discoveries in the 20^{th} century. In the seventies, x-ray imaging revolutionized medical imaging for a second time by the development of computed tomography by Hounsfield *et al.* Up today, discoveries in the field of x-ray research led to a total number of 17 Nobel prices.

This scientific success was accompanied by a continuous improvement of x-ray sources. An ideal x-ray source should have a high flux radiated into a small solid angle. The x-rays should originate from a small source size, and be as monochromatic as possible, i.e., have a low polychromaticity. All these quantities can be subsumed into a single number, defining the x-ray source brilliance:

$$\text{brilliance} = \frac{\text{flux}}{\text{solid angle} \times \text{source size} \times \text{polychromaticity}} .$$

In the early days, Röntgen produced x-rays with a so-called Geisler discharge tube, which were very unstable and difficult to run reliably. A big step forward was provided by x-ray tubes with a glowing filament and a water-cooled anode, reaching a brilliance of about 10^5. To prevent the anode material from melting, the power was limited by the cooling power of the anode material. In the sixties, sources with rotating anodes improved the x-ray tube to a brilliance of 10^7 and provided the technical basis for most sources used in clinical applications nowadays. Large-scale synchrotron sources vastly improved the brilliance of x-rays by using synchrotron radiation and other insertion devices to produce x-rays. The highest brilliance nowadays is provided by free-electron lasers, reaching peak brilliance values of $> 10^{30}$. However, those devices are too large and too expensive for applications in clinical routine. One way to bring highly brilliant x-ray sources towards clinical applications are compact light sources [Huang, 1998].

They use the principle of inverse Compton scattering to improve the monochromaticity and coherence of the emitted x-rays. Most of the experiments reported in this thesis are conducted at the Munich Compact Light Source (MuCLS). The MuCLS is the first commercially sold x-ray source based on inverse Compton scattering. With a brilliance of about 10^{10}, it aims to close the gap in between lab-based sources and large-scale synchrotrons.

Although Laue had shown that x-rays are electromagnetic waves and therefore subject to refraction and scattering, those effects were not exploited for imaging purposes immediately. At synchrotron facilities, first x-ray interferometers were only built in the 1960s by Bonse and Hart [Bonse, 1965]. Subsequently, other techniques were developed to obtain phase-contrast images such as crystal-analyzer based imaging or propagation based imaging. They typically rely on a coherent x-ray beam or require high-resolution detectors. Another possibility to generate phase-contrast images is to exploit the so-called Talbot-effect to convert phase-information to a measurable attenuation signal [Talbot, 1836]. A second analyzer grating can be used to avoid the need of high-resolution x-ray detectors [Weitkamp, 2005]. If the spatial coherence is too low to observe self-interference effects, a third optical grating can be placed in front of the source [Pfeiffer, 2006]. Analog to optical light microscopy, grating-based phase-contrast interferometry provides three contrast modalities denoted as attenuation image, differential phase-contrast image and dark-field image Pfeiffer *et al.* [Pfeiffer, 2008]. The dark-field is a measure for the coherence reduction induced by a sample, leading to a reduced interference pattern visibility. The signal is strongly related to small-angle x-ray scattering (SAXS) events [Yashiro, 2011b; Strobl, 2014]. At synchrotrons, SAXS has been used as a two-dimensional imaging method since the 1990s [Fratzl, 1997]. Long measurement times and limited access to synchrotrons prevented the large-scale use of this method. Moreover, the directional dependence of the scattering signal provided a challenge for three-dimensional reconstruction, which has been resolved only recently [Schaff, 2015b]. Dark-field imaging can overcome some limitations of SAXS by providing a larger field of view and strongly reduced measurement times. Due to the use of one-dimensional gratings, the dark-field is mainly sensitive to scattering in one direction. Jensen *et al.* [Jensen, 2010b] investigated this dependence by rotating the sample around the optical axis. Revol *et al.* [Revol, 2012] and Malecki *et al.* [Malecki, 2013] proposed a sinusoidal model for the scattering dependence, which yields the mean scattering, its anisotropy, and the main scattering direction. The corresponding method is known as X-ray Vector Radiography [Potdevin, 2012] (XVR).

The aim of this thesis is to develop XVR towards medical imaging applications. Directional scattering yields information about subpixel structures for extended samples. Our hypothesis is that this can be used to improve the detection of subtle changes in bone microstructures. Building upon existing work which already showed that XVR can be related to mechanical properties [Eggl, 2015; Baum, 2015] and the trabecular

microstructure [Schaff, 2015a], we identify two main goals of this thesis as follows:

- Show the feasibility of XVR for extended samples
- Provide evidence that the additional contrast provided by XVR leads to valuable image information

Outline

Chapter 2 gives an overview of the fundamental interactions of x-ray with matter. The attenuation and coherent x-ray scattering are particularly crucial to understand the underlying physical principles that lead to the x-ray imaging methods applied in this thesis.

Chapter 3 deals with the origin of x-rays. Special attention is paid to non-target-based sources such as compact light sources. The MuCLS is described in detail as a link between large synchrotron facilities and conventional laboratory sources.

Grating-based phase-contrast imaging is described in chapter 4, describing the possibility to exploit the refractive index as well as small-angle x-ray scattering for imaging purposes.

The directional dependence of the dark-field signal is exploited in two dimensions by x-ray vector radiography. An introduction to the theoretical basis is given in chapter 5.

Chapter 6 describes the experimental setup which was mainly used for the measurements in this paper.

The first feasibility study for XVR applied to a larger sample is described in chapter 7. It provided evidence that the scattering anisotropy signal is sensitive to trabecular microstructure changes. Hence, a potential application for the detection of bone microfractures became apparent.

Such fractures are often radiographically occult and thus not detected in conventional radiography. In a follow-up study presented in chapter 8, microfractures were artificially induced in porcine loin ribs. Although cracks were not visible in the attenuation image, they caused an increased scattering signal.

In chapter 9, the scattering signal was applied for the detection of tooth microcracks. Such cracks are a common clinical finding and a diagnostic challenge up today.

Interactions with Matter 2

This chapter briefly introduces the fundamental interactions of x-rays with matter. From a variety of available textbooks [Buzug, 2008; Willmott, 2011; Attwood, 2016; AlsNielsen, 2011], we follow mostly Als-Nielsen *et al.* [AlsNielsen, 2011]. On an atomic level, x-ray photons can interact with an atom in two ways: they are absorbed or scattered.As shown in Fig. 2.1, the absorption is known as the photoelectric effect in which the photons transfer all their energy to an electron. Scattering without energy transfer (i.e., elastic scattering) is known as Thomson scattering or coherent scattering since the phase information is preserved in this case. If there is an energy transfer, the scattering process is inelastic and known as Compton scattering. In this case, all phase information is lost and the scattering process incoherent. The probability for an interaction generally depends on the energy of the x-ray photons as well as the chemical composition of the interacting matter, which is ultimately the source of contrast in x-ray imaging. Macroscopically, those effects lead to the attenuation and refraction of x-rays which are described more detailed in chapter 4.

2.1 Photoelectric Effect

In the photoelectric effect (cf. Fig. 2.1), a photon is completely absorbed by an electron. The prerequisite for this is that the photon energy is sufficient to overcome the

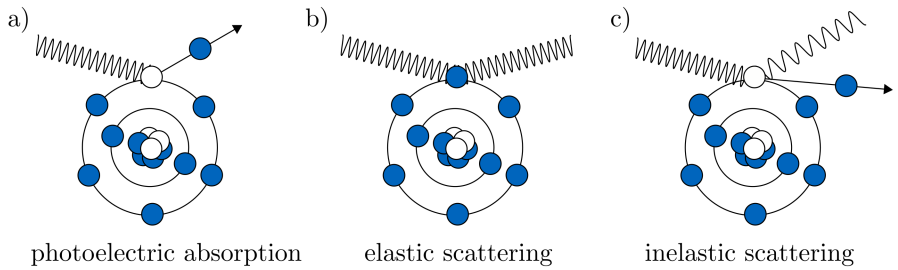

Figure 2.1: **Interactions of x-rays with matter.** a) In photoelectric absorption, an incoming photon is completely absorbed by an electron. b) X-ray scattering without energy transfer, i.e. no change in wavelength, is coherent, whereas inelastic scattering shown in c) is incoherent.

binding energy of the electron and hence to ionize the atom. If electrons from deeper shells can also be ionized with increasing photon energy, the absorption increases instantaneously. The most relevant of this so-called absorption edges originates from the innermost K-shell, as it is located in the x-ray range for many elements. The hole in the electron configuration can now be closed by an electron from a higher shell, emitting a fluorescence photon or an Auger electron. The probability for an electron being absorbed by a single atom can be described by the cross-section σ_a. Since photons are absorbed by electrons, it is intuitively clear that the cross section depends on the number of electrons and thus on the atomic number Z. Empirically it is found that [AlsNielsen, 2011, p. 239]

$$\sigma_a \propto Z^4 E^{-3}\,, \tag{2.1}$$

leading to a contrast between materials of different atomic numbers. The higher absorption of low energy photons shifts the mean energy of a polychromatic spectrum towards higher energies when passing a thick sample, leading to so-called beam hardening artifacts in tomographic reconstruction [Buzug, 2008, p. 425]. However, it can as well be exploited in a energy resolved measurement to gain additional image information.

2.2 Elastic Scattering

Elastic scattering can be described in a classical picture: an electron oscillates in the electric field of an incoming electromagnetic wave and hence emits radiation. If the electron can be considered a quasi-free particle, this scattering process is also known as Thomson scattering. This holds essentially true for x-rays with energies higher than the resonance frequencies of electrons bound in an atom. The differential cross-section for the scattering process is given by [AlsNielsen, 2011, p. 9]

$$\frac{\mathrm{d}\sigma_T}{\mathrm{d}\Omega} = \frac{8\pi}{3} r_0^2\,, \tag{2.2}$$

where $r_0 = 2.82 \cdot 10^{-15}\,\mathrm{m}$ is the classical electron radius. Since no energy is transferred, the frequency of the electromagnetic wave and the kinetic energy of the electron remain unchanged. Thomson scattering is a coherent scattering process and thus preserves the phase-information of the incoming wave, although a phase-shift of π is introduced. Hence, scattered photons can interfere with each other ultimately leading to the phase-contrast signal which is in more detail described in chapter 4.

2.3 Inelastic Scattering

Inelastic scattering or Compton scattering can only be described in a quantum-mechanical image by understanding light as a beam of quantized photons. Considering the conservation of energy and momentum, a connection between the change in wavelength and the scattering angle can be found as [AlsNielsen, 2011, p. 17]

$$\Delta\lambda = \lambda_c(1 - \cos\theta)\,, \tag{2.3}$$

where $\lambda_c = h/m_e c$ denotes the Compton-wavelength and θ is the angle between the incident and scattered photon. Elastic scattering can be considered as the low-energy limit of Compton scattering for $\lambda \gg \lambda_c$, i.e. wavelengths much larger than the Compton-wavelength. The scattering cross-section for Compton scattering is given by the Klein-Nishina equation [Klein, 1929].

3 Generation of X-rays

3.1 Figures of Merit

3.1.1 Brilliance

An ideal X-ray source should emit many photons per time into a small solid angle. In addition, a small source spot should ensure a high spatial coherence and the emitted photons should be monochromatic. The brilliance summarizes all those quantities into a single number and is given by [AlsNielsen, 2011, p. 32]

$$B = \frac{\Phi}{\Delta A \, \Delta\Omega \Delta E/E} = \frac{\text{Photons/second}}{(\text{mrad})^2(\text{mm}^2 \, \text{source area})(0.1\% \, \text{BW})} \, , \tag{3.1}$$

where Φ is the x-ray flux, ΔA the source size, Ω is the solid angle covered by the source and $\Delta E/E$ is the energy bandwidth. The right-hand side denotes the units conventionally used to calculate the brilliance. Figure 3.1 depicts its development over time. The first x-ray tubes could reach a brilliance of about 10^5. With rotating anodes, the target cooling was improved and the brilliance was increased to about 10^7. In the second half of the 20th century, synchrotron sources enormously increased the brilliance by many orders of magnitude. Free electron lasers represent the next step to higher brilliance with peak values of $> 10^{30}$ [AlsNielsen, 2011, p. 62]. Compared to those large-scale devices, compact light-sources such as the Munich Compact Light Source (MuCLS) have a lower brilliance of about 10^{10} comparable to 1st generation synchrotrons [Eggl, 2016].

3.1.2 Emittance

The emittance of an x-ray beam is defined by the product of the source size and its divergence [AlsNielsen, 2011, p. 54]. Thus, the emittance ends up in the denominator of Eq. (3.1) and is required to be small for a highly brilliant beam. The fundamental limit for the emittance can be derived from Heisenberg's uncertainty principle. Below this limit, a decrease in source size will lead to an increase of divergence and vice versa.

For synchrotron-based sources such as undulators and inverse Compton sources, the emittance of the x-ray beam is inherited from the electron beam emittance. In that

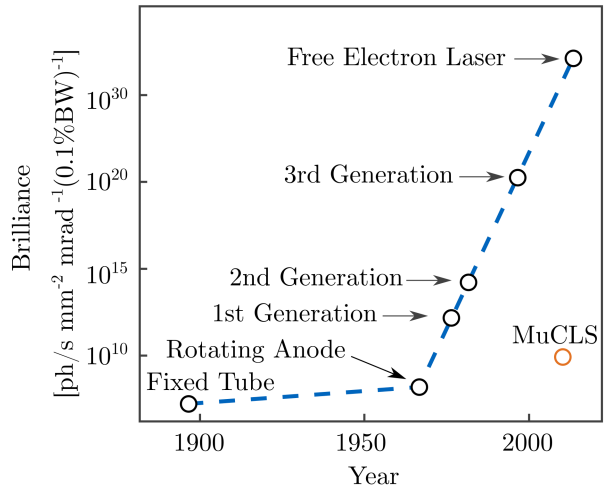

Figure 3.1: **The progress of brilliance over time.** The first fixed x-ray tubes were improved to Rotating Anode tubes used in clinical practice nowadays with brilliance of about 10^7. Large-scale synchrotron facilities vastly improved the brilliance, modern Free Electron Laser can exceed values of 10^{30}. Compact Light Sources such as the Munich Compact Light Source (MuCLS) close the gap between laboratory-based tubes and large-scale facilities by providing brilliance of 10^{10} comparable to a small synchrotron with a size fitting into a laboratory. Figure adapted from [AlsNielsen, 2011, p. 2].

case, it is given by the convolution of the electron beam emittance and the emittance of the x-ray source for the passage of a single electron [AlsNielsen, 2011, p. 54].

3.1.3 Coherence

For an ideal point source emitting a single wavelength λ, it is enough to know the amplitude and phase in one point in space and at one time to fully determine the wavefield. In reality, sources are never perfectly monochromatic and are not point-like but extended in space. Unless the emitter itself is coherent, it is hence only possible to predict the wave properties for a particular time (or equivalently longitudinal direction) and in a limited area transversal to the propagation direction. Quantitatively, these limits are given by the longitudinal and transversal coherence lengths, respectively. We shall define the lateral coherence length as [AlsNielsen, 2011, p. 27]

$$L_L = \frac{1}{2}\frac{\lambda^2}{\Delta\lambda}, \tag{3.2}$$

with wavelength λ and wavelength spread $\Delta\lambda$. This corresponds to the distance when two waves with slightly different wavelengths λ and $\lambda - \Delta\lambda$ are entirely out of phase.

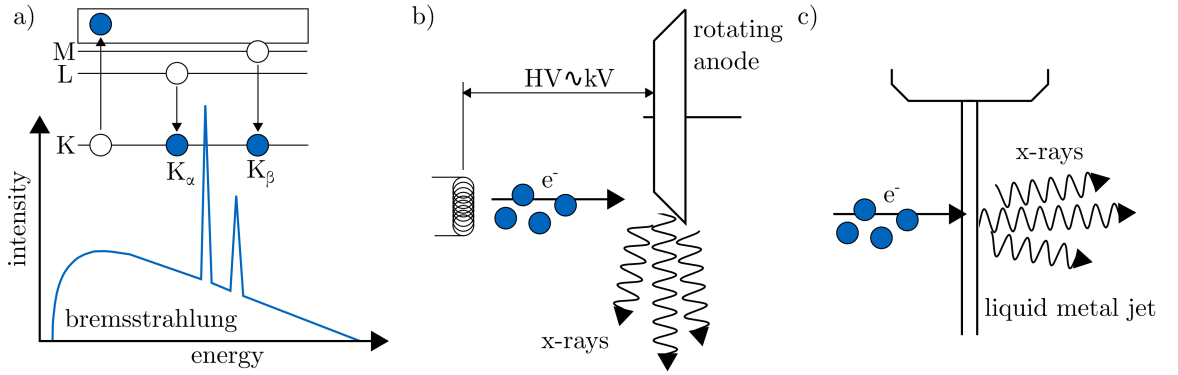

Figure 3.2: **Schematic illustration of target-based x-ray sources** a) Illustration of an x-ray spectrum emitted from a target-based source. A continuous part consisting of bremsstrahlung is overlaid with fluorescence lines. The most relevant transitions K_α and K_β are sketched on the top. b) In an X-ray tube, electrons are accelerated from a filament towards an anode material. For rotating anode tubes, the target can rotate allowing for more effective cooling. c) Liquid metal jet sources overcome the issue of heat transportation by using a liquid metal alloy as the target. Figure adapted from [AlsNielsen, 2011, p. 31].

Now consider two waves that are emerging from different ends of an extended source with source size D. Seen from a point $R \gg D$ far away from the source, they will become plane waves propagating in slightly different directions. The transversal coherence length at a distance R is then given by [AlsNielsen, 2011, p. 27]

$$L_T = \frac{\lambda}{2}\frac{R}{D}, \tag{3.3}$$

which corresponds to the distance perpendicular to the propagation direction when both waves are out of phase. Note that the transversal coherence not only depends on the source size but the distance to the source as well. For instance, light reaching us from distant stars is very coherent, whereas sunlight is incoherent.

3.2 Target-based X-ray Sources

The historically first and most straightforward way to produce x-rays is to accelerate electrons onto a target material [AlsNielsen, 2011, p. 30]. This generates a continuous spectrum of x-rays with overlaid fluorescence lines as sketched in Fig. 3.2 a). The continuous part is composed of bremsstrahlung which is generated by electrons deflected

and decelerated in the target material. It continuously contains all energies up to a maximum given by the electron kinetic energy. However, the incoming electrons can as well ionize target atoms by exciting inner shell electrons. When the resulting hole is filled by an outer shell electron, a fluorescence photon with the corresponding energy difference is emitted. For x-rays, the holes are typically filled from the L and M shell, leading to emissions denoted by K_α and K_β.

X-ray tubes as schematically shown in Fig. 3.2 b) use a filament to provide electrons, which are subsequently accelerated with a high voltage towards a target material like tungsten. They provide a cost-effective way to produce x-rays with a compact device. Hence they are widely used in medical imaging applications and non-destructive testing. The mean energy of the spectrum is tunable through the maximum acceleration voltage, and the flux can be increased by increasing the current of electrons hitting the target, usually at the cost of an increased source size. The flux is, however, limited by the cooling capacity of the anode material, as the largest part of the electron energy is converted into heat. This can be partially overcome by a rotating anode which allows periodic cooling of the non-exposed target material. In liquid metal jet sources as depicted in Fig. 3.2 c), the target material consists of a metal alloy which is liquid at room temperature, avoiding the issue of a melting target [Hemberg, 2003]. Moreover, it is immediately replaced after being hit by the electron beam, allowing for high intensities. A quasi-monochromatic spectrum with a decent flux can be achieved in such a source by choosing an appropriate metal liquid and by filtering the spectrum for one distinct fluorescence line.

3.3 Synchrotron Sources

Each charged particle, when accelerated, emits electromagnetic radiation. This is also the case in storage rings, where charged particles are kept on a circular trajectory by bending magnets. For this special case of relativistic charged particles accelerated in a magnetic field, the term synchrotron radiation is used [Iwanenko, 1944]. In particle physics, it is an unwanted effect which at some point limits the maximal energy that can be stored in a synchrotron given a certain radius. However, the energy of synchrotron radiation in typical storage rings is within the x-ray regime and can hence be exploited for imaging purposes. This is done in specialized facilities using relativistic electrons as charged particles to produce x-rays. This section gives a quick overview of how x-rays are produced at so-called synchrotrons, more details can be found in Als-Nielsen *et al.* [AlsNielsen, 2011, p. 30-60].

In 1^{st} generation synchrotrons, bending magnets were used to generate x-rays. They emit a polychromatic spectrum with a characteristic energy related to the bending radius of the magnet and the electron energy. Due to the Doppler-effect, the radiation

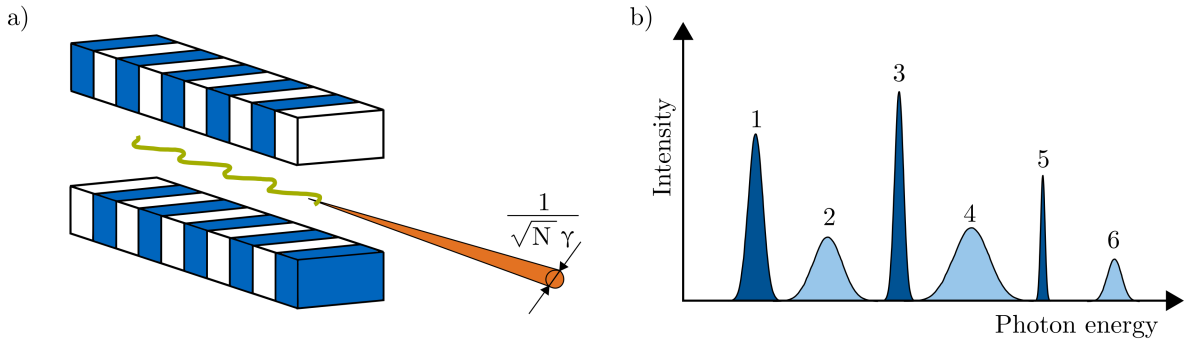

Figure 3.3: **Illustration of an undulator** a) shows an alternating magnetic field created by permanent magnets. Waves emitted in different undulator periods constructively interfere and lead to a cone of x-rays. b) The undulator spectrum consists of harmonic wavelengths. They can be tuned to different energies by changing K according to Eq. (3.4). Figure adapted from [AlsNielsen, 2011, p. 42, p. 58]

seen by an observer tangential to a bending magnet is confined in a cone related to the Lorentz factor via $1/\gamma$. For typical electron energies of $E \approx 1\,\mathrm{GeV}$, this leads to a small opening angle of $1/\gamma \approx 1\,\mathrm{mrad}$.

So-called insertion devices such as undulators are somewhat more advanced. From its schematic view in Fig. 3.3 a) it is clear that important parameters include the strength of the permanent magnets B_0, the period λ_u between two magnets of same polarity and properties of the electron. They are summarized by the dimensionless number [AlsNielsen, 2011, p. 44]

$$K = \frac{eB_0\lambda_u}{2\pi\, m_e c}\,, \tag{3.4}$$

where e is the electron charge, m_e its rest mass and c the speed of light. For specific harmonic wavelengths, x-rays emitted in each undulator period constructively interfere. Hence, the amplitudes add up and lead to an enormous intensity amplification. The first fundamental wavelength is given by [AlsNielsen, 2011, p. 45]

$$\lambda_1(\theta) = \frac{\lambda_u}{2\gamma^2}\left(1 + \frac{K^2}{2} + (\gamma\theta)^2\right)\,, \tag{3.5}$$

where θ is the angle between an observer and the undulator axis. Similar to the bending magnet, the opening angle $1/\sqrt{N}\gamma$ is related to the Lorentz factor but reduced by the number of undulator periods. Since constructive interference is only given for the harmonic wavelengths, the undulator spectrum features peaks which are intrinsically very monochromatic. A sample spectrum can be found in Fig. 3.3 b). It shows the

fundamental wavelength and higher harmonics, which can be used to get higher x-ray energies. Their wavelengths can be tuned as well by changing the undulator period λ_u.

Although the radiation of an electron in an undulator is coherent, different electrons in an electron bunch add up incoherently. This can be overcome by a free electron laser, which is in simple terms a very long undulator [AlsNielsen, 2011, p. 61]. For electron bunches with sufficiently short pulse lengths and respectively high intensities, so-called Self Amplified Spontaneous Emission sub-divides a single electron bunch into a set of microbunches which again coherently produce x-rays. The thereby produced x-rays have a brilliance several orders of magnitude higher than 3^{rd} generation synchrotrons (cf. Fig. 3.1). Moreover, pulse lengths of less than 100 fs allow time-resolved measurements of chemical processes and could provide new insights into the atomic structure of materials.

3.4 Compact Light Sources

Modern synchrotrons with several hundred meters in diameter and free electron lasers with kilometer-range length are large-scale and very costly facilities. Although they provide very brilliant x-rays for basic research, it is impossible to imagine a widespread use of such sources for clinical imaging, radiation therapy or non-destructive testing. For this reason, efforts have been made to create compact light sources which combine the benefits of highly brilliant synchrotron sources with the small size and lower relative cost of target-based sources [Huang, 1998; Loewen, 2003; Tang, 2009; Kuroda, 2011; Variola, 2011; Variola, 2014; Pogorelsky, 2016; Chi, 2017].The following sections provide a brief description of the working principle of a Compact Light Source (CLS) in both the wave picture and the particle picture. An example of such a device is given by the Munich Compact Light Source (MuCLS) which was used for the main experiments reported in this thesis.

Particle Picture: Inverse Compton Scattering

The most vivid way to imagine the working principle of a CLS is given using the particle picture. In chapter 2, the inelastic scattering of photons with an electron led to a decreasing energy proportional to the Compton wavelength λ_c (cf. Eq. (2.3)). In the inverse process, a low-energy photon is scattered by a highly energetic electron towards higher energies. This process is called *inverse Compton scattering* and depicted schematically in Fig. 3.4. Looking ahead to describe the Munich Compact Light Source (MuCLS), we denote the incoming photon as an infrared laser photon with Energy E_l and the scattered photon as x-ray photon with energy E_x. Applying the conservation

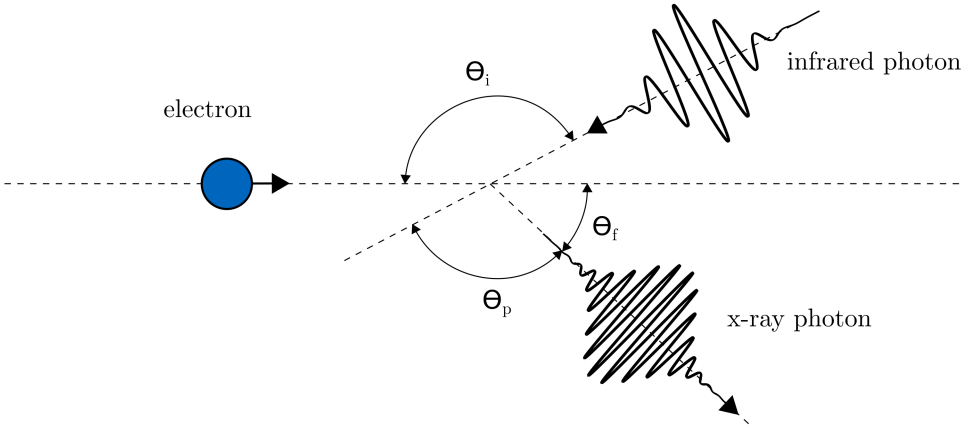

Figure 3.4: **Sketch of an inverse Compton scattering process for energies used at the MuCLS.** An electron and an infrared photon are scattered under a scattering angle θ_i. The scattered photon has a higher energy in the x-ray regime and is scattered by an angle θ_f.

of energy and momentum, the energy of the scattered photon is given by [Sun, 2011]

$$E_x = \frac{(1 - \beta \cos\theta_i) E_l}{(1 - \beta \cos\theta_f) + (1 - \cos\theta_p) E_l / E_e} \,. \tag{3.6}$$

With the electron trajectory defining the main axis, θ_i corresponds to the angle of the incident photon, θ_f to the angle of the scattered photon and θ_p is the angle between the incident and scattered photon. The factor $\beta = v/c$ is defined as the ratio of the electron energy to the speed of light. This equation can be simplified for the case of head-on collision ($\theta_i = \pi$, $\theta_p = \pi - \theta_f$) to read [Sun, 2011]

$$E_x = \frac{(1 + \beta) E_l}{(1 - \beta \cos\theta_f) + (1 + \cos\theta_f) E_l / E_e} \,. \tag{3.7}$$

For on-axis radiation ($\theta_f = 0$), ultra-relativistic electrons ($\gamma \gg 1$) and neglecting the recoil effect ($4\gamma^2 E_l / E_e \ll 1$), Eq. (3.7) can be rewritten as [Sun, 2011]

$$E_x = 4\gamma^2 E_p \,. \tag{3.8}$$

In this form, it is easy to see that relativistic electrons with Energies $E_e \approx 50\,\mathrm{MeV}$ and hence $\gamma^2 \approx 10^3$ can boost infrared photons with $E_l \approx 1\,\mathrm{eV}$ to the x-ray regime ($E_x \approx 1\,\mathrm{keV}$). Moreover, a change in electron energy allows to dynamically tune the x-ray energy. The intensity distribution of inverse Compton scattering is given by the

Klein-Nishina equation [Stepanek, 1998]:

$$\frac{\mathrm{d}\sigma}{\sin\theta_f \,\mathrm{d}\theta_f} = \pi r_e^2 \frac{1-\beta^2}{(1-\beta\cos\theta_f)^2} R^2 \left(R + \frac{1}{R} - 1 + \left(\frac{\cos\theta_f - \beta}{1-\beta\cos\theta_f} \right)^2 \right) , \\ R = \left[1 + \left((1+\beta)\gamma E_l / mc^2 \right) \left(1 + \frac{\cos\theta_f - \beta}{1-\beta\cos\theta_f} \right) \right]^{-1} . \tag{3.9}$$

Wave Picture: Undulator

In the wave picture, compact light sources can be modeled as miniature undulators. Recalling Eq. (3.5) for the fundamental wavelength of an undulator, it can be seen that for a weak undulator ($K^2 \ll 1$) and on-axis radiation ($\theta = 0$) it simplifies to

$$\lambda_1 = \frac{\lambda_u}{2\gamma^2} , \tag{3.10}$$

where λ_u is the undulator period and γ the Lorentz factor. Given typical undulator periods of $\lambda_u \approx 1\,\mathrm{cm}$, a Lorentz factor of about $\gamma \gtrsim 10^3$ is required to get radiation in the x-ray regime. A decrease of the undulator period, however, would relax the condition for γ and hence allow for a more compact storage ring design. For example, decreasing the undulator period to about 1 µm would reduce the Lorentz factor and hence the storage ring size by about a factor 100. Since this is not possible by using permanent magnets, compact light sources replace the magnets by a counter-propagating electromagnetic wave exerting a Lorentz force on the electrons. As derived by Als-Nielsen *et al.* [AlsNielsen, 2011, p. 62], the Lorentz force is equal to the one seen by an electron in a permanent magnet undulator if

$$\lambda_u = \lambda_l / 2 \,, \; B_u = 2 B_l \,, \tag{3.11}$$

where the index u denotes the undulator and l the laser. Inserting Eq. (3.12) into Eq. (3.10) and substituting the wavelength with energy yields

$$E_x = 4\gamma^2 E_l \,, \tag{3.12}$$

which is similar to Eq. (3.8) derived using inverse Compton scattering.

3.4.1 The Munich Compact Light Source

The principles of x-ray generation discussed in the previous sections are implemented in the Munich Compact Light Source (MuCLS), the first commercially sold compact synchrotron source. It was developed and produced by Lyncean Technologies Inc.,

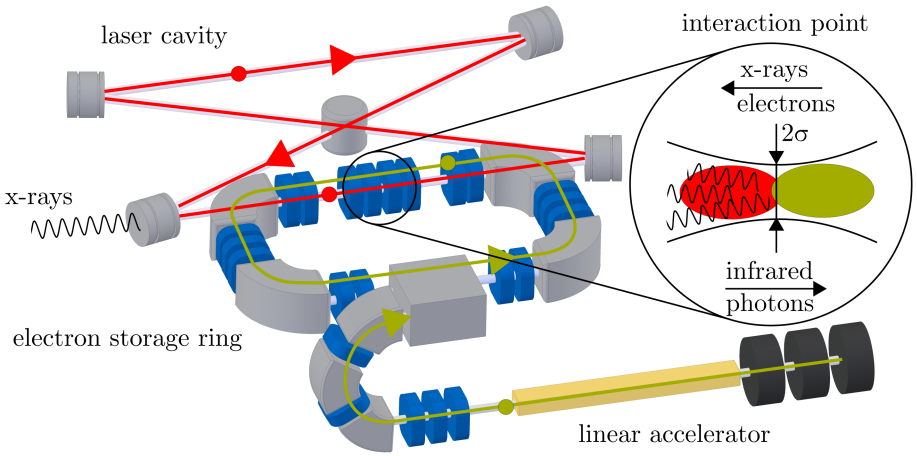

Figure 3.5: **Schematic overview of the Munich Compact Light Source.** On the top, the laser enhancement cavity stores infrared photons. Electrons are brought to relativistic energies by a linear accelerator and injected into a storage ring. In the interaction point, electrons and infrared photons collide and produce x-rays via inverse Compton scattering. The x-rays leave the MuCLS through an exit window in the laser enhancement cavity.

USA. It mainly consists of a small electron storage ring of about 4.6 m circumference and a high-finesse a laser cavity, as illustrated in Fig. 3.5. The laser enhancement cavity resonantly stores an infrared laser power up to 350 kW with a fixed wavelength of $\lambda = 1064\,\text{nm}$, corresponding to an energy of $E_l = 1.17\,\text{eV}$. Electrons are brought to relativistic energies between 29 MeV and 44 MeV by a linear accelerator and subsequently injected into a storage ring. The electron bunches cycle with a repetition rate of about 65 MHz and are replaced with a rate of 25 Hz. In the interaction point, focused laser bunches collide with the electron bunches in an area about diameter $2\sigma \approx 100\,\mu\text{m}$ and generate x-rays as described in the previous sections. Finally, x-rays leave the MuCLS through a transmissive window in one of the laser cavity mirrors, where they are confined to an opening angle of $\pm 2\,\text{mrad}$. The main x-ray energy used for experiments in this thesis was 25 keV, which according to Eq. (3.8) corresponds to an electron energy of $E_e = 37.43\,\text{MeV}$. In Fig. 3.6, the main characteristics of inverse Compton scattering for this configuration are shown. For the calculations, we derived $\gamma = E_e/511\,\text{MeV}$ and $\beta = \sqrt{1 - 1/\gamma^2}$ from the electron energy. Panel a) illustrates the x-ray energy depending on the scattering angle θ_f according to Eq. (3.7). The energy drops by about 2% at the maximal MuCLS opening half-angle of $\theta_f = 2\,\text{mrad}$. In practice, however, different opening angles are mixed due to the finite electron beam divergence which leads to an even smaller energy drop. In b), the dependency of the x-ray energy on the electron energy according to Eq. (3.8) is depicted. Dashed lines indicate the dynamic

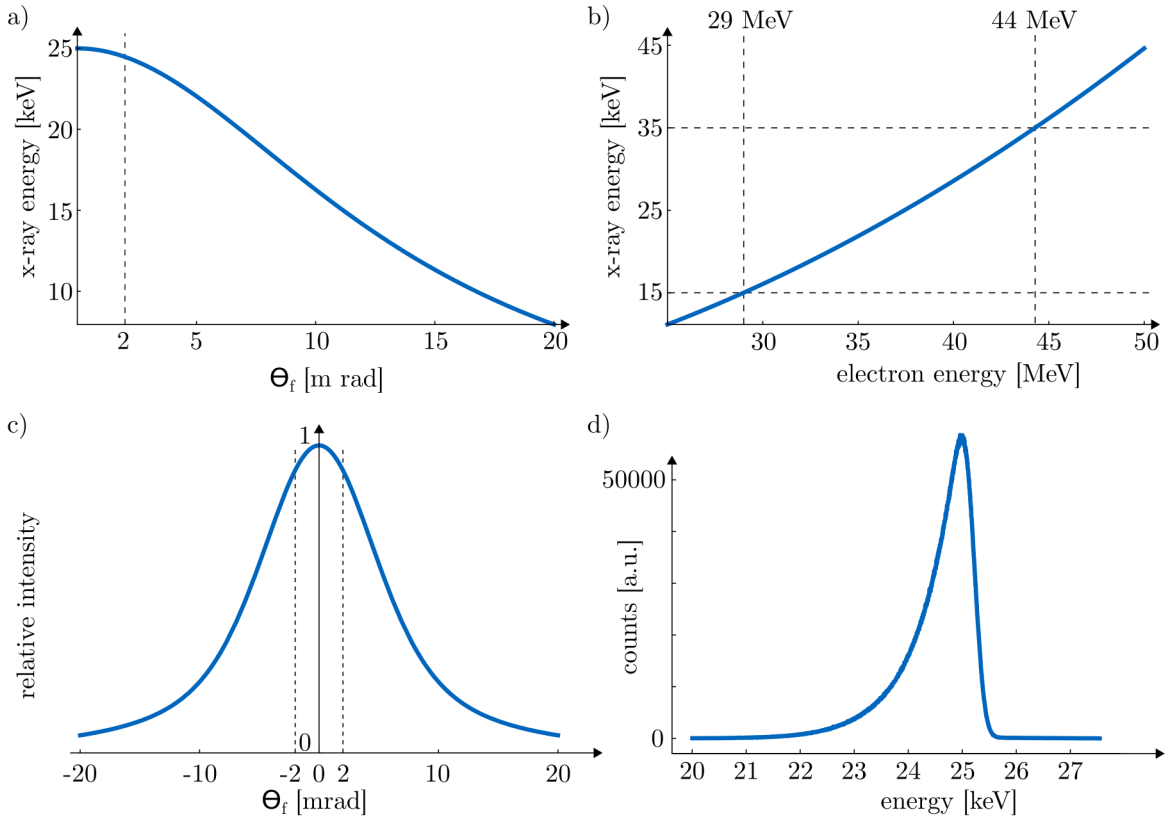

Figure 3.6: **Characteristics of inverse Compton scattering calculated using parameters of a MuCLS configuration.** a) X-ray energy depending on the opening half-angle θ_f according to Eq. (3.7). b) Tunable x-ray energyies are given by Eq. (3.8). For the MuCLS, x-ray energies between $15 - 35\,\mathrm{keV}$ can be reached. c) The relative intensity varies with θ_f according to Eq. (3.9) and drops by 7% for an opening angle of $\theta_f = 2\,\mathrm{mrad}$. d) Measured spectrum for the MuCLS with a bandwidth $\Delta E/E$ of a few percents.

range of the MuCLS corresponding to x-ray energies between 15 keV and 35 keV. In c), the relative x-ray intensity depending on the opening half-angle θ_f is illustrated according to Eq. (3.9). A dashed vertical line again indicates the maximal opening half-angle, for which the relative intensity decreases by about 7 %. Again, the finite electron divergence reduces the intensity drop to a value of about 2% []. The measured x-ray spectrum for this configuration is shown in d). It has a sharp peak at the designed energy, resulting in a small source bandwidth $\Delta E/E$ of a few percents. The spectrum is broadened towards both higher and lower energies due to the distribution in electron energies and laser photon energies. However, towards lower energies, there is an additional broadening due to the electron beam divergence which dominates on this side of the peak [Loewen, 2003].

When the MuCLS was installed in 2015, Eggl *et al.* [Eggl, 2016] found an average flux of about $\Phi \approx 1 \cdot 10^{10}$ photons s^{-1}, a source size of $\sigma = 42\,\mu\mathrm{m}$, a bandwidth $\Delta E/E = 0.03$ and an angular spread of $\theta = 4\,\mathrm{mrad}$. Using Eq. (3.1), this yields a brilliance of

$$B = \frac{\Phi}{\Delta A\,\Delta\Omega(\Delta E/E)(0.1\%\,\mathrm{bandwidth})} = 4.8 \cdot 10^9\,\mathrm{photons}\,s^{-1}\mathrm{mm}^{-2}\,\mathrm{mrad}^{-2}\,(0.1\%\,\mathrm{bandwidth})^{-1}\,, \tag{3.13}$$

where $\Delta A = \pi\sigma^2$ and $\Delta\Omega \approx 4\pi(\theta/4)^2$.

Grating-based Phase-contrast Imaging 4

X-ray phase-contrast imaging has been studied since the late 1960's at synchrotron facilities. Since then, several techniques have been established such as crystal interferometers, analyzer-based imaging, propagation-based imaging or grating-based phase-contrast imaging. A crystal-interferometer splits the beam into two different paths, one of which passes the sample. Phase-contrast is recorded after both beams are recombined and interfere with each other [Bonse, 1965]. For crystal analyzer-based imaging, a crystal is placed downstream the sample such that x-rays meeting the Bragg condition are recorded on a detector. The analyzer crystal is rotated, and the phase-contrast image can be extracted from the resulting intensity variations with respect to crystal orientation. In addition to the phase-contrast image, a signal related to small-angle scattering (SAXS) is recorded [Davis, 1995; Chapman, 1997]. Propagation-based imaging uses the effect of self-interference of a sufficiently coherent wave to generate phase-enhanced images. Although no special setup components are required, high-resolution detectors are typically needed to record the phase effects. If certain constraints like a low absorption or single material sample are fulfilled, the phase can be reconstructed from a single projection [Paganin, 2002].

Grating-based phase-contrast imaging exploits the so-called Talbot-effect to convert phase-information to a measurable attenuation signal [Talbot, 1836; Momose, 2003; Weitkamp, 2005]. In contrast to the previous techniques, it can be implemented at laboratory sources by adding an additional x-ray optical grating [Pfeiffer, 2006]. A single grating-based phase-contrast measurement provides three different contrast modalities, in analogy to visible light microscopy denoted as attenuation image, differential phase-contrast image and dark-field image [Pfeiffer, 2008]. The latter is related to (SAXS) with the advantage of a much bigger field of view compared to the corresponding synchrotron methods [Fratzl, 1997; Yashiro, 2011b; Strobl, 2014].

4.1 Complex refractive index

Like visible light, x-rays are macroscopically refracted if they pass through matter. However, refraction is a very small effect for x-rays which makes it more convenient to describe the refractive index by a deviation from unity $\delta \approx 10^{-6}$. Including attenuation,

the complex refractive index is given by Als-Nielsen *et al.* [AlsNielsen, 2011, p. 75]

$$n = 1 - \delta + i\beta\,, \tag{4.1}$$

where the real part accounts for the refraction of x-rays and the imaginary part for attenuation. Note that in contrast to visible light, the real part of the refractive index is smaller than one. This leads to effects like total external reflection for x-rays, which can be exploited by x-ray optics and imaging methods. The complex refractive index decrement δ is given by Als-Nielsen *et al.* [AlsNielsen, 2011, p. 71]

$$\delta = \frac{2\pi\rho\, r_0}{k^2}\,, \tag{4.2}$$

where ρ is the electron density and r_0 is the classical electron radius.

By comparing the wave number in vacuum k to nk in matter, it can be seen that the complex part of the refractive index β is related to the attenuation coefficient by $\mu = 2k\beta$ [AlsNielsen, 2011, p. 76]. The resulting exponential decay of x-ray transmission through a homogeneous sample of thickness z is known as Beer-Lambert law [AlsNielsen, 2011, p. 20]

$$T(z) = e^{-\mu z}\,. \tag{4.3}$$

In general, μ is proportional to the atomic number density and the attenuation cross-section $\sigma_t ot$, which is for biological tissues well approximated by the absorption cross-section described in chapter 2.

4.2 Talbot Effect

The Talbot effect states that a periodic and sufficiently coherent wavefront repeats itself after certain distances. These so-called Talbot distances d_T are given by

$$d_T = \frac{2p^2}{\lambda}\,, \tag{4.4}$$

where p is the wavefront periodicity and λ the wavelength [Talbot, 1836]. In practice, such a wavefront modulation can be achieved by placing periodic structures such as gratings in the beam [Momose, 2003]. Figure 4.1 illustrates the intensity modulation for three individual cases widely used in x-ray imaging. In a), the Talbot carpet shown for a pure absorption grating repeats itself after the Talbot distance d_T. For a pure phase grating with a phase-shift of $\pi/2$ as shown in b), the wavefront is only phase shifted and hence no intensity modulation is found right after the grating and at the Talbot distance. However, the phase information is transformed to an intensity modulation with the same periodicity at certain fractions of d_T, in this case, given

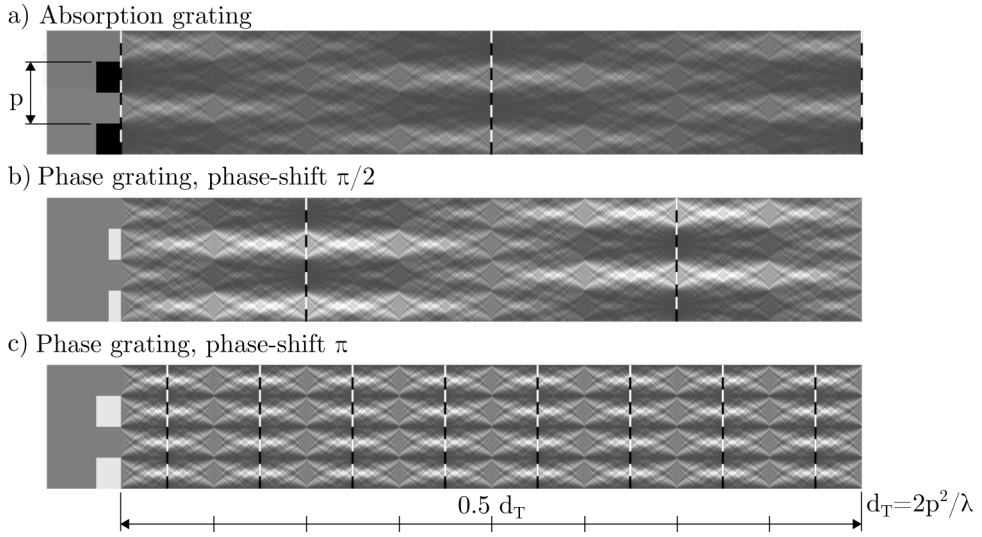

Figure 4.1: **Visualization of the Talbot effect for an incident plane wave for different gratings.** The intensity modulation for one Talbot distance is shown, positions with maximal contrast are indicated by black-and-white lines. a) For an absorption grating, the binary intensity pattern repeats itself at the Talbot distance and half the Talbot distance. b) Pure phase-grating with a phase-shift of $\pi/2$ has no intensity modulation at the full Talbot distance. At so-called fractional Talbot distances, however, the phase-shift is converted to a measurable intensity modulation. c) For a phase-shift of π, the intensity modulations at fractional Talbot distances have half the phase-grating period. Figure adapted from Weitkamp *et al.* [Weitkamp, 2006].

by $1/4d_T$ and $3/4d_T$. If the phase-shift is π, there are even more so-called fractional Talbot distances as can be seen in c). There are distances of high contrast, e.g. at $1/16d_T$ and $3/16d_T$ with twice the period of the phase-shifting grating. Quantitatively, the fractional Talbot distances d_n can be calculated as [Weitkamp, 2006]

$$d_n = \frac{1}{\eta^2}\frac{np^2}{2\lambda} = \frac{n}{4\eta^2}d_T \quad (n = 0, 1, 2, ...)\,, \tag{4.5}$$

where p is the grating period, and n denotes the Talbot-order. A factor of $\eta = 1$ is used for absorption gratings and $\pi/2$ phase-shifting grating whereas one should set $\eta = 2$ for π phase-shifting gratings. Maximal contrast is achieved at even Talbot-orders for absorption gratings and odd ones for phase gratings. If the incident wave is not a plane wave but originating in a point source with distance L upstream of the grating, the Talbot distances are stretched by a geometric magnification factor $M = (L + d_n)/L$.

Figure 4.2: **Schematic illustration of a Talbot interferometer.** The phase-grating G_1 is positioned at distance L downstream of the source. An attenuation grating G_2 is placed at an appropriate distance d in front of the detector, given by Eq.(4.5). The sample is placed at a distance L_s upstream of the detector, here exemplary between G_1 and G_2.

4.3 Image Extraction

As discussed in the previous section, a proper phase-grating G_1 with period p_1 converts phase information to a measurable intensity modulation at certain fractional Talbot-distances. For practical reasons, laboratory-sized setups are restricted to a length in the order of $L \approx 1m$. From Eq. (4.5) it follows that for x-rays ($\lambda \approx 10^{-10}$ m), the grating period should then be $p_1 \approx 10\,\mu$m. The intensity modulation at a fractional Talbot distance d_T will have the same periodicity $p_2 \approx p_1$, except for a factor given by the geometric magnification. For most commonly used x-ray detectors, the resolution is one order of magnitude lower and hence it is impossible for them to directly resolve the intensity modulation. One way to avoid the need for high-resolution x-ray detectors is to place an additional absorption grating G_2 at the fractional Talbot distance with a period p_2 matching the intensity modulation. This is shown in Fig. 4.2 for a point source at distance L upstream of G_1 and grating G_2 at distance d downstream of G_1. The sample position from G_2 is denoted by L_s, its influence on the dark-field signal will be discussed in section 4.4. If a series of images are recorded with different positions x_g of grating G_2 covering at least one period p_2, the intensity modulation can be detected indirectly. For each detector pixel, this so-called phase-stepping procedure yields a stepping curve, i.e., the convolution of the binary intensity modulation with the binary absorption grating G_2. Ideally, the convolution of two box-like functions leads to a triangle function, but grating imperfections, as well as the system point-spread-function, lead to a blurred stepping curve of sinusoidal shape described by Bech [Bech, 2009, p. 39]

$$I(x_g) = a_0 + a_1 \cos(2\pi\, x_g/p_2 + \varphi)\,. \tag{4.6}$$

Since intensities are positive, we can state that for stepping curves $a_0 \geqslant a_1$. If a sample is placed in the beam, attenuation, phase-shifts and x-ray scattering will alter this intensity modulation. The corresponding contrast modalities can be extracted by

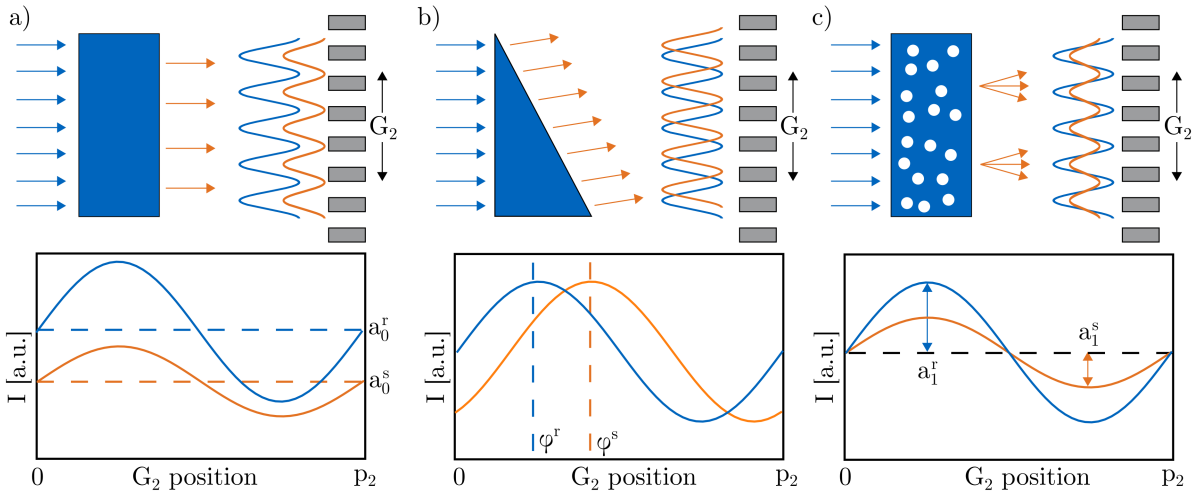

Figure 4.3: **Schematic overview of the signal extraction.** a) An attenuating object compresses the stepping curve and decreases its mean value. The transmission is then given by $T = a_0^s/a_0^r$. b) Phase objects do not attenuate x-rays but shift the stepping curve by an amount $dpc = \varphi_s - \varphi_r$ corresponding to the differential phase-contrast. c) Scattered x-rays decrease the stepping curve visibility. The resulting dark-field image is given by $df = a_1^s a_0^r/(a_0^s a_1^r)$.

comparing the stepping curve to a reference curve without a sample.

4.3.1 Transmission

In the case of an attenuating sample as shown in Fig. 4.3 a), the stepping curve will be compressed. Hence, the mean value a_0^s will be shifted to lower intensities with respect to the reference curve. The sample transmission is then given by Bech [Bech, 2009, p. 36]

$$T = \frac{a_0^s}{a_0^r}\,, \tag{4.7}$$

where the superscripts s and r correspond to the stepping curve recorded with and without a sample, respectively. It is worth noting that the transmission T is fully equivalent to a conventional attenuation image and that there is no trade-off between the conventional attenuation image and the additional contrast modalities in terms of achievable image quality.

4.3.2 Differential Phase-contrast

A pure phase-object will not change the intensity but deflect the wavefront by a certain refraction angle. As shown in Fig. 4.3 b), this leads to a shift of the stepping curve given by Bech [Bech, 2009, p. 36]

$$dpc = \varphi_s - \varphi_r \,, \tag{4.8}$$

which is proportional to the partial derivative of the phase-shift within the sample [Bech, 2009, p. 38] and hence denoted as the differential phase-contrast image. Since this thesis is not focusing on the differential phase-contrast signal, the reader is referred to the existing literature for more detailed information.

4.3.3 Dark-field

Pfeiffer *et al.* [Pfeiffer, 2008] introduced an additional contrast modality, the so-called dark-field. It mainly investigates the visibility of stepping curves, which is defined as

$$V = \frac{I_{\max} - I_{\min}}{I_{\max} + I_{\min}} = \frac{a_1}{a_0} \,, \tag{4.9}$$

where on the right side the definition was applied to a stepping curve defined by Eq. (4.6). Maximal visibility of $V = 1$ then indicates a stepping curve with zero intensity at one point or equivalently $a_1 = a_0$, whereas $V = 0$ describes a flat curve with $a_1 = 0$. Figure 4.3 c) depicts an idealized object whose only effect is to reduce the stepping curve visibility. The dark-field is defined as

$$df = \frac{V^s}{V^r} = \frac{a_1^s a_0^r}{a_0^s a_1^r} \,. \tag{4.10}$$

The dark-field is normalized with $df = 1$ corresponding to no visibility loss and $df = 0$ for a complete loss of visibility.

4.4 Origin of the Dark-field signal

Since its introduction by Pfeiffer *et al.* [Pfeiffer, 2008], many research papers investigated the origin of the dark-field signal [Yashiro, 2011b; Lynch, 2011; Yashiro, 2011a; Yang, 2012; Strobl, 2014; Wolf, 2015; Yashiro, 2015a; Yashiro, 2015b]. Yashiro et al. [Yashiro, 2011b; Yashiro, 2011a] and Lynch *et al.* [Lynch, 2011] provide an elaborate mathematical explanation for the dark-field. It was found that unresolvable edges [Yang, 2012; Wolf, 2015; Yashiro, 2015a] and beam-hardening [Yashiro, 2015b] also

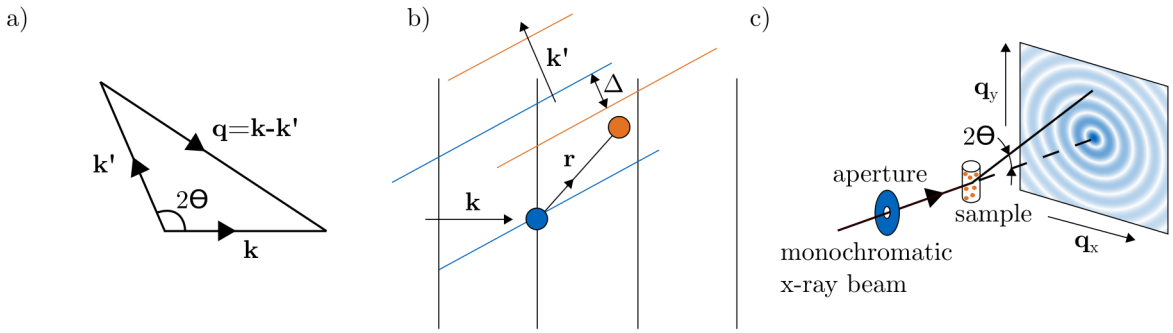

Figure 4.4: **Definition of important quantities used in SAXS.** a) Definition of wavevector transfer $\vec{q}$ for an x-ray scattered with scattering angle 2θ. b) In the Fraunhofer regime, x-rays scattered at different electrons will have a phase-difference $\Delta = \vec{q} \cdot \vec{r}$. c) In a SAXS-experiment, many $\vec{q}$-vectors are probed by an area detector. The measured intensity corresponds to the absolute value of the electron density Fourier transform. Figure adapted from Als-Nielsen *et al.* [AlsNielsen, 2011, p. 114, p. 135].

lead to a dark-field signal. The dominating signal source, however, was found to be small-angle x-ray scattering (SAXS). Similar to other x-ray imaging methods, an analogy of dark-field imaging to neutron imaging could be found in spin-echo small-angle neutron scattering (SESANS) [Andersson, 2008]. A neat explanation covering both neutrons and x-rays was provided by Strobl [Strobl, 2014] and experimentally verified by Prade *et al.* [Prade, 2015]. The derivation in this section will be mostly based on those papers.

4.4.1 Small-angle X-ray Scattering

X-ray scattering techniques exploit the interference of x-rays scattered at a sample. From the map of constructive and destructive interference, information about structures up to atomic length scales can be retrieved. Hence, the signal originates from elastic scattering processes which preserve phase information (cf. chapter 2), inelastic scattering is neglected. The scattered waves shall be recorded at an observation distance much larger than the probed structures. In this case, the scattered waves can be approximated as plane waves (Fraunhofer regime). Further, we assume that scattering is weak in the sense that multiple scattering can be ignored. This is known as the kinematic approximation or first Born approximation [AlsNielsen, 2011, p. 86,]. The natural unit to describe scattering processes is the wavevector transfer [AlsNielsen, 2011, p. 114]

$$\vec{q} = \vec{k} - \vec{k}' \,, \tag{4.11}$$

where $\vec{k}$ describes the incident wave and $\vec{k}'$ the wave scattered under an angle 2θ as shown in Fig. 4.4 a). Since the wavevector length is unchanged, its absolute value is given by [AlsNielsen, 2011, p. 114]

$$q = |\vec{q}| = 2k \sin\theta \,. \tag{4.12}$$

Figure 4.4 b) depicts the simple case where an incident wave is scattered by two electrons with finite distance $\vec{r}$. For elastic scattering, both electrons can be seen as sources of scattered waves with wave vectors $\vec{k}'$. Because of the finite distance between both electrons, there will be a phase difference between the scattered waves which is given by $\Delta = \vec{q} \cdot \vec{r}$. Thus, the product $\vec{q} \cdot \vec{r}$ is a measure for constructive or destructive interference.

Small-angle x-ray scattering (SAXS) is a particular technique that records scattering at very small angles $2\theta \ll 1$ and yields information about structures much larger than inner-atomic distances. The restriction to small scattering angles allows some simplifying assumptions such as the small-angle approximation $2\theta \approx \tan 2\theta \approx \sin 2\theta$. More importantly, it follows that only $\vec{q}$-vectors in a plane orthogonal to the incoming photon direction are probed. Generalizing the considerations regarding two electrons above to a sample with electron density $\rho(\vec{r})$, it follows that the scattered intensity is given by [AlsNielsen, 2011, p. 134]

$$I_{\mathrm{SAXS}}(\vec{q}) = |\mathcal{F}[\rho(\vec{r})]|^2 \,, \tag{4.13}$$

where $\mathcal{F}$ denotes the Fourier transform. The fact that the intensity corresponds to the absolute value squared of the Fourier transform inhibits a direct back-transformation of measured intensities to get the electron density and is known as the phase problem in crystallography. From the properties of Fourier transforms it follows that I_{SAXS} is point-symmetrical

$$I_{\mathrm{SAXS}}(\vec{q}) = I_{\mathrm{SAXS}}(-\vec{q}) \,, \tag{4.14}$$

which is known as Friedel's law [AlsNielsen, 2011, p. 290]. A schematic illustration of a SAXS-experiment is shown in Fig. 4.4 c): a monochromatic beam is spatially confined by a series of apertures and scattered by a sample. With an area detector, the intensities corresponding to different vectors $\vec{q} = (q_x, q_y, 0)$ are simultaneously recorded, spatial resolution can be achieved by scanning the sample through the beam.

4.4.2 Small-angle Scattering in a Grating Interferometer

In this section, a correlation between a dark-field image and a single scattering process according to Strobl [Strobl, 2014] is given. In addition, we restrict ourself to scattering perpendicular to the grating orientation and hence $q_y = 0$. Consider a Talbot grating-interferometer as sketched in Fig. 4.2, with a sample placed upstream of G_2 at a distance

L_s. If an x-ray photon is scattered by a sample, the interference pattern will be shifted by an amount x corresponding to a scattering angle

$$\tan 2\theta \approx 2\theta = x/L_s \,, \tag{4.15}$$

where in the first step we used the small-angle approximation $\tan 2\theta \approx \sin 2\theta \approx 2\theta$. From a scattering perspective, the same angle 2θ corresponds to a wavevector transfer in x-direction according to Eq. (4.12) and hence

$$q_x = 2k \sin\theta \approx \frac{4\pi\,\theta}{\lambda} \,. \tag{4.16}$$

The shift x of the interference pattern corresponds to a phase shift $\Delta\omega$. Using Eq. (4.15) and Eq. (4.16) this yields

$$\Delta\omega = \frac{2\pi\,x}{p_2} = \frac{2\pi\,2\theta L_s}{p_2} = \frac{\lambda L_s}{p_2} q_x \,, \tag{4.17}$$

where p_2 is the period of G_2 according to Fig. 4.2. Hence, the phase-shift of the interference pattern is directly proportional to the wavevector transfer q_x. The proportionality factor only depends on setup specific parameters such as the x-ray wavelength λ, sample position L_s and grating period p_2. Those quantities are summarized in the so-called setup autocorrelation length [Lynch, 2011; Strobl, 2014]

$$\xi_{\mathrm{GI}} = \frac{\lambda L_s}{\mathrm{p}_2} \,. \tag{4.18}$$

It is a measure for the length scales probed in a dark-field image and can be easily tuned, e.g. by changing the sample position. For a given setup, its maximal value is achieved for a sample close to G_1 and linearly decreases to zero for a sample close to G_2. If the sample is placed upstream of G_1, the variable L_s should be replaced by $L_s' = (L_1 + L_2 - L_s)L_2/L_1$. In practical units, the autocorrelation length is given by

$$\xi_{\mathrm{GI}}[\mu\mathrm{m}] = \frac{12.4\,L_s[\mathrm{cm}]}{\mathrm{E[keV]}\,p_2[\mu\mathrm{m}]} \,. \tag{4.19}$$

4.4.3 Correlation between Small-angle Scattering and Dark-field

Having established a connection between the phase-shift $\Delta\omega$ and the wavevector transfer in direction q_x, we can now investigate how a scattering event affects the measurement in a grating interferometer and ultimately the dark-field. Again, the derivation given in this section follows Strobl [Strobl, 2014]. We recall the stepping curve

$I(\omega) = a_0 + a_1 \cos\omega$ (cf. Eq. (4.6)), where ω was placed as the total phase with $\varphi = 0$ for convenience. From Eq. (4.17) it is clear that a scattered photon will phase shift the stepping curve by $\Delta\omega = \xi_{\mathrm{GI}} q_x$. Scattering in one direction q_x indicates, however, equal scattering in the opposite direction $-q_x$ according to Eq. (4.14). We are left with the superposition of two cosine waves shifted in opposite directions. Assuming that all the intensity is scattered by $\pm\vec{q}_x$, the stepping curve becomes

$$I_{\mathrm{tot}}(\omega) = \frac{1}{2} I(\omega + \Delta\omega) + \frac{1}{2} I(\omega + \Delta\omega) = \frac{a_0}{2} + \frac{a_1}{2}\cos(\omega + \Delta\omega) + \frac{a_0}{2} + \frac{a_1}{2}\cos(\omega - \Delta\omega)\,. \tag{4.20}$$

Using the addition theorem

$$(\cos(\Delta\omega) + \cos(-\Delta\omega))/2 = \cos(\Delta\omega)\,, \tag{4.21}$$

this equation can be simplified to

$$I_{\mathrm{tot}}(\omega) = a_0 + a_1 \cos(\omega)\cos(\Delta\omega) = a_0 + a_1 \cos(\omega)\cos(\xi_{\mathrm{GI}} q_x)\,. \tag{4.22}$$

Inserting into Eq. (4.9) for the visibility yields

$$V(\xi_{\mathrm{GI}}) = V_0(\xi_{\mathrm{GI}})\cos(\xi_{\mathrm{GsI}} q_x)\,, \tag{4.23}$$

where $V_0(\xi_{\mathrm{GI}})$ is the reference visibility without a sample. Hence, SAXS in a grating interferometer will lead to a loss in visibility and consequently to a reduced dark-field.

Until now, we allowed only scattering in the x-direction perpendicular to the grating bars. Our goal is now to correlate a generic SAXS-pattern $I_{\mathrm{SAXS}}(\vec{q})$ to a grating interferometer measurement. For the generalization we first recall the coordinate system with the z-axis along the beam direction, the x-axis perpendicular to the grating bars and the y-axis is chosen according to the right-hand rule as visualized in Fig. 4.2. For a SAXS-measurement, we can set the component in beam direction $q_z \approx 0$. A grating interferometer only detects shifts of the interference pattern perpendicular to the grating bars, i.e., in the x-direction. Hence, only the projected $\vec{q}$-vector onto the x-axis is detected which reads

$$I_{s,rel}(q_x) = \int I_{\mathrm{SAXS}}(q_x, q_y, 0)\,\mathrm{d}q_y\,. \tag{4.24}$$

The normalized fracture of scattered intensity scattered with a specific value q_x is then given by

$$S(q_x) = I_{s,rel}(q_x)\left(\int I_{s,rel}(q_x)\,\mathrm{d}q_x\right)^{-1}\,. \tag{4.25}$$

Given this equation, we generalize Eq.(4.23) to allow general $\vec{q}$-vectors:

$$V(\xi_{\mathrm{GI}}) = V_0(\xi_{\mathrm{GI}}) \int S(q_x)\cos(\xi_{\mathrm{GI}} q_x)\mathrm{d}q_x = V_0(\xi_{\mathrm{GI}})\, G(\xi_{\mathrm{GI}})\,. \tag{4.26}$$

In the last step, we exploited that the integral corresponds to a Fourier transform of a real-space correlation function $G(\xi_{\mathrm{GI}})$. Unscattered radiation can be included by taking into account the macroscopic scattering cross section Σ. If multiple scattering and a finite sample thickness is assumed, the dark-field is finally given by [Strobl, 2014]

$$df(\xi_{\mathrm{GI}}) = \exp\left(\int \Sigma\left(G(\xi_{\mathrm{GI}}) - 1\right) \mathrm{d}z\right) . \tag{4.27}$$

Note that both G and Σ are position-dependent functions.

5 X-ray Vector Radiography

In the previous section, a connection between microscopic scattering events and a decreasing dark-field signal was shown. However, it was derived that only x-rays scattered perpendicular to the grating bars fully contribute to the signal. Intuitively, this opens up a possibility for directional dark-field imaging, thus to investigate the directional dependence of scattering. This directional dark-field imaging was first investigated by Jensen *et al.* [Jensen, 2010b; Jensen, 2010a]. They scanned different scattering orientations by rotating the sample around the optical axis, a technique which is now mostly known as x-ray vector radiography (XVR) [Potdevin, 2012]. Based on that work, Revol *et al.* [Revol, 2012] and Malecki *et al.* [Malecki, 2013] proposed a sinusoidal dependence of the negative logarithmic dark-field signal, which allows distinguishing between isotropic and anisotropic scattering contributions. For trabecular tissue, a connection between XVR and trabecular microstructures have been shown [Potdevin, 2012; Schaff, 2015a]. A connection between the degree of anisotropy and femoral bone strength as well as an improved prediction of vertebral failure load indicate the potential of XVR for osteoporosis imaging [Eggl, 2015; Baum, 2015]. In this chapter, an overview of XVR, as well as its limitations, will be given.

We recall from the previous chapter that the dark-field signal is mainly connected to small-angle x-ray scattering (SAXS). First, we consider the simplest case of a uniformly scattering sample. The position-dependent scattering cross section σ, particle density N and correlation length of scattering structures R are connected by [Strobl, 2008]

$$\epsilon = \frac{\sigma N}{R^2} \,. \tag{5.1}$$

The quantity ϵ is proportional to a quantity referred to as linear diffusion coefficient [Bech, 2009], we will denote it as scattering strength. The measured dark-field signal is connected to the scattering strength by a Lambert-Beer like law [Strobl, 2008]:

$$df = \exp\left(-\int \epsilon \,\mathrm{d}t\right) \,. \tag{5.2}$$

In case of anisotropic scattering, its profile can sometimes by approximated by a Gaussian scattering function [Yashiro, 2011b], we will follow this assumption used by Revol *et al.* [Revol, 2012] and Malecki *et al.* [Malecki, 2013] to develop a useful model for XVR.

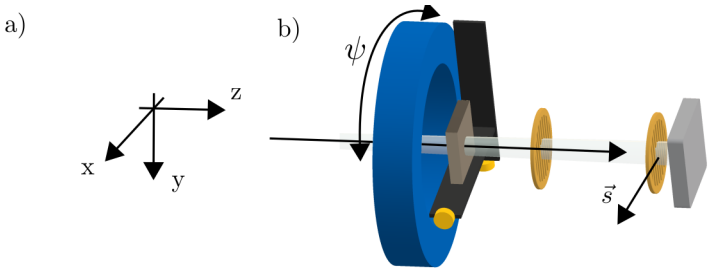

Figure 5.1: **Conventions used in x-ray vector radiography.** a) The z-axis is defined in the beam direction, the y-axis points downwards. The x-axis is defined according to the right-hand rule. b) Several stages allow rotating the sample around the optical axis. The rotation is denoted by ψ. Rotation is positive according to the right-hand rule along the z-axis.

In Fig. 5.1 a), the coordinate system is chosen such that the z-axis points in the beam direction, the y-axis points downwards and the x-axis horizontal corresponding to the right-hand rule. Since scattering is mainly detected perpendicular to the grating bars in an interferometer, we introduce the sensitivity vector $\vec{s}$. For vertically oriented gratings, $\vec{s}$ points in the x-direction (see Fig. 5.1).

The sample orientation around the optical axis (z-axis) is denoted by ψ, its sign is given by the right-hand-rule. To account for the grating interferometer sensitivity, [Revol, 2012] projected the Gaussian scattering function to the sensitivity-axis and altered an undisturbed stepping curve by a convolution. In the end, a sinusoidal dependence of the negative logarithm was found [Revol, 2012; Malecki, 2013]:

$$-\log(df) = b_0 - b_1 \cos(2(\psi - \alpha_s - \alpha)) \,, \tag{5.3}$$

where ψ is the sample orientation around the optical axis, α_s denotes the sensitivity orientation and α the orientation of scattering structures. The sensitivity orientation corresponds to the angle between the sensitivity vector $\vec{s}$ and the x-axis, i.e., $\alpha_s = 0$ for vertically aligned gratings and $\alpha_s = \pi/2$ for horizontally aligned gratings. Note that this curve has a form similar to the stepping curve defined in Eq.(4.6), we use a different notation to avoid confusion. Here, the parameter b_0 corresponds to the *mean scattering strength* averaged over different orientations:

$$\epsilon = b_0 \,. \tag{5.4}$$

Using the definition of the visibility from Eq. (4.9), we define the *degree of anisotropy* as

$$da = b_1/b_0 \,. \tag{5.5}$$

In addition to the sample orientation, the phase of the cosine function in Eq. (5.3) depends the orientation of sample structures, and the sensitivity orientation. For con-

venience, we assume that the sensitivity orientation is aligned with the x-axis, i.e., $\alpha_s = 0$. In that case, a *structure* orientation in the *horizontal* direction with $\alpha = 0$ correspond to maximal *scattering* in the *vertical* direction. Note that for other sign conventions in literature, the meaning of α can vary.

In Fig. 5.2, the dependence of the scattering strength on the sample rotation is illustrated for a simple phantom sample. It consists of an Eppendorf tube filled with water, a plastic rod filled with flour and two plates of carbon fibers. In a), the scattering strength for four sample orientations and hence senstivity directions is illustrated. Three pixels are marked by a blue cross, a green circle, and an orange triangle, respectively. Their scattering values for all thirteen angles are depicted in b). One can see the sinusoidal dependence with a periodicity of 180°, and the three fit parameters.

In Fig. 5.3, the resulting contrast modalities are presented. In a), the integrated attenuation coefficient allows the comparison with conventional x-ray contrast. Here, the water is most prominent, whereas the flour and the carbon fibers are not visible at all. The mean scattering strength in b) mostly highlights the flour and, to a lesser extent, the carbon fibers on the right. For the Eppendorf tube and the plastic rod, the edges are well visible which is consistent with previous findings that sharp edges lead to a scattering signal oriented perpendicular to the edge [Wolf, 2015]. The degree of anisotropy is illustrated in c). A value of $da = 0$ indicates isotropic scattering with a specific scattering strength given by b_0, $da = 1$ corresponds to maximal scattering in one direction and a complete loss of scattering in the orthogonal direction. This explains that both the water and the flour have a low degree of anisotropy, although their mean scattering strength differs a lot. The carbon fibers have are predominantly oriented in one direction. Hence, they mainly scatter perpendicular to the fiber orientation which leads to a high degree of anisotropy [Malecki, 2014]. The structure orientation is presented in d), where each color corresponds to an angle according to the color-wheel shown on the top right. The scattering signal at sharp edges such as the Eppendorf tube and the plastic rod is mainly oriented perpendicular to the edge, highlighting the structure along the edges. The measurement confirms the carbon fiber orientation in the horizontal and vertical direction, respectively. Note that this would be possible also without directly resolving the fiber bundles.

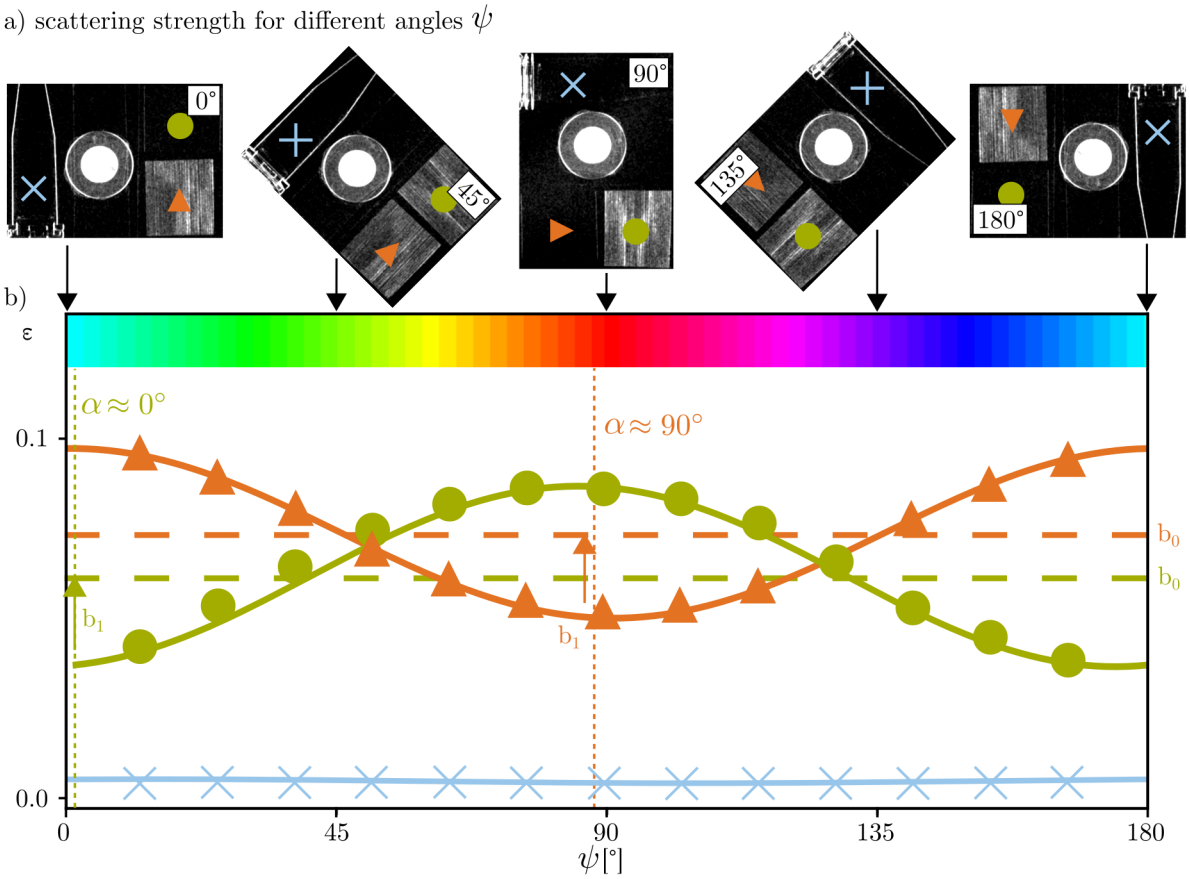

Figure 5.2: **Illustration of the XVR-processing.** a) The scattering strength, defined as $-\log(df)$, is illustrated for four different sample orientations ψ and illustrates its dependence on the sensitivity orientation. b) The sinusoidal dependence of the scattering strength on the sample orientation is plotted for three sample pixels marked in a). From this dependence, three fit parameters b_0, b_1 and α allow to calculate the mean scattering strength $\epsilon = b_0$, the degree of anisotropy da $= b_1/b_0$ and the orientation of scattering structures α. For XVR-measurements, the structure orientation is often color-coded as indicated on the top.

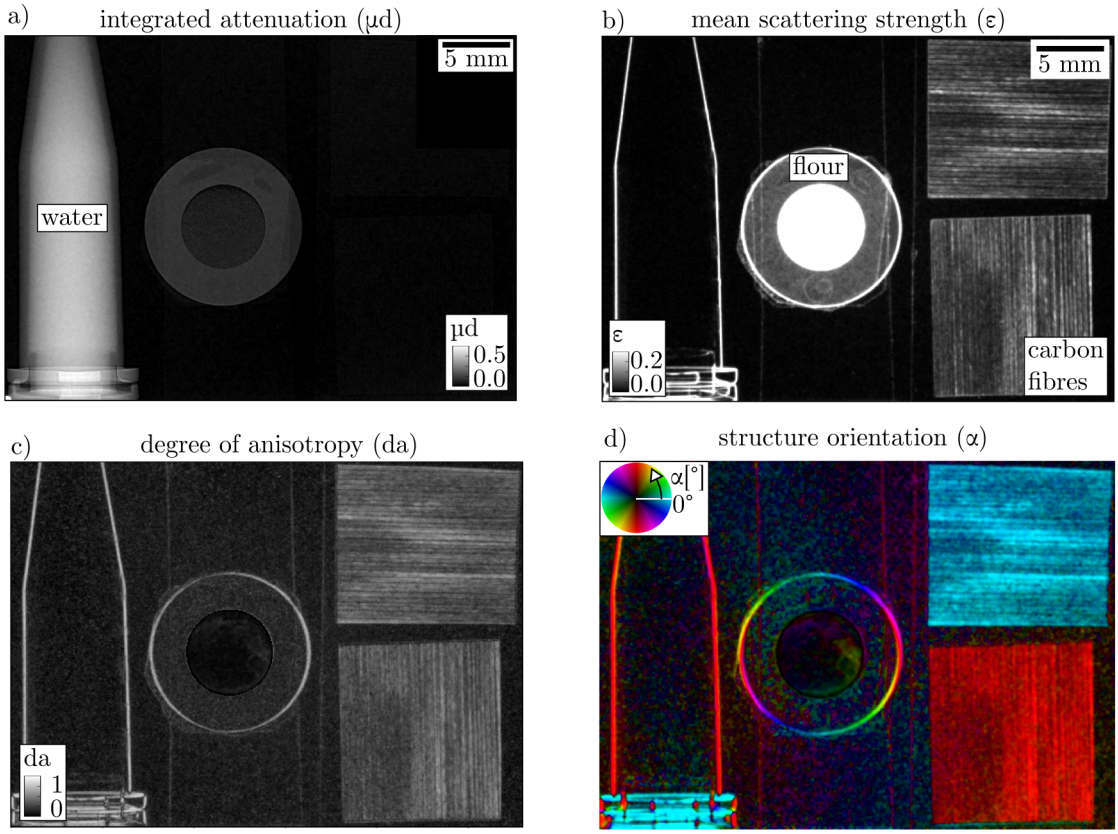

Figure 5.3: **Illustration of an XVR for a well defined sample consisting of water, flour and carbon fibers.** a) shows the integrated attenuation coefficient μd, which is simultaneously acquired in an XVR-measurement. b) illustrates the mean scattering strength ϵ. The water is homogeneous with no substantial changes in electron density. Hence, it is has a very low signal in all contrast modalities provided by XVR. The flour is homogeneous as well, but due to its powdery substructure, the electron density rapidly changes leading to a strong scattering signal. The carbon fibers on the right have a decent scattering signal as well. c) depicts the degree of anisotropy. The flour scatters very isotropic and hence leads to a very low degree of anisotropy in contrast to the carbon fibers, which have the highest degree of anisotropy. d) From the direction of least scattering, the structure orientation can be derived. It is shown color-coded in the bottom left, the brightness corresponds to the degree of anisotropy.

6 Experimental Setup

The Munich Compact Light Source, described in chapter 3, is mostly used for imaging research purposes. Since the beam is divergent with an opening angle of 4 mrad, distances closer to the source provide a high flux density whereas further away the field of view (FOV) increases. Accordingly, two experimental hutches have been installed at distances of about 5 m and 15 m from the source point. The first experimental hutch features a beam diameter of about $1.5 - 3.0$ cm and is mainly used for propagation-based phase-contrast imaging [Gradl, 2017; Gradl, 2018] and micro-beam radiation therapy [Burger, 2017]. The second one has a wider beam of about 6.5 cm in diameter and is well suited for larger samples due to its larger FOV. A higher spatial coherence compared to the first experimental hutch favors phase-contrast imaging as well. Applications include coronary angiography [Eggl, 2017] and low-dose phase-contrast mammography [Eggl, 2018]. All experiments reported in this thesis were conducted in the second experimental hutch, which is subsequently described in more detail.

6.1 Setup Design Considerations

For the design of a grating interferometer, a number of free parameters have to be chosen. The most fundamental concern for an interferometer is to ensure that spatial coherence is sufficiently high to observe interference effects. To get a measure for the coherence, we recall Eq. (3.3) where the transversal coherence length was defined as

Design Energy E [keV]	Wavelength $\lambda[\mathring{A}]$	G_1-period p_1[µm]	G_2-period p_2[µm]	Talbot distance d_1[cm]
25	0.50	4.92	5.0	24.8
35	0.35	4.89	5.0	34.5

Table 6.1: **Interferometer parameters for the experimental setup.** For both design energies, the source distance $L = 15$ m and a phase shift for G_1 of $\pi/2$ ($\eta = 1$) was given. For the first Talbot order $n = 1$, the Talbot distance and phase-grating period p_1 follow from Eq. (6.1) and Eq. (6.2), respectively.

$l_c = \lambda R/(2D)$. For the MuCLS (cf. section 3.4.1), experimental values are given for the source size $D \approx 2\sigma = 84\,\mu m$, the interferometer distance $L \approx 15m$ downstream of the source and the central energy of $E = 25\,keV$ ($\lambda = 0.5\,\mathring{A}$). This yields a spatial coherence of $l_c \approx 4.4\,\mu m$. Talbot grating interferometers with reasonable inter-grating distances, i.e., that would potentially fit into a compact medical device, have grating periods in the same order of magnitude. Hence, the spatial coherence is sufficient to detect interference effects. The coherence length could be further increased by a lower energy, but at the same time, it would make it more challenging to penetrate thicker samples. Therefore, two design energies of 25 keV and 35 keV were chosen for the grating interferometer at the MuCLS. Furthermore, the visibility of a setup should be maximized since it leads to a higher setup sensitivity [Birnbacher, 2016]. Following Weitkamp *et al.* [Weitkamp, 2006], the visibility for a given setup can be estimated from the coherence length, the Talbot order and the grating periods. Apart from the visibility, higher sensitivity can be achieved by longer interferometers. In Eggl [Eggl, 2017, p. 72], a summary of different design possibilities is given as well as their expected visibilities. Based on all previous considerations, a Talbot order of $n = 1$, a phase-shift for G_1 of $\pi/2$ (i.e. $\eta = 1$) and a period for the analyzer grating G_2 of $p_2 = 5\,\mu m$ were chosen. Using the notation given in Fig.4.2, we use Eq. (4.5), multiplied by the magnification factor $M = (L + d_n)/L$, and take into account the relation $p_2 = Mp_1$ between both grating periods. Solving the resulting system of equations for d_n and p_1 yields

$$d_n = \frac{-L\eta^2\lambda + \sqrt{L\eta^2\lambda(2np_2^2 + L\eta^2\lambda)}}{2\eta^2\lambda} \tag{6.1}$$

for the fractional Talbot-distance, and

$$p_1 = \frac{-L\eta^2\lambda + \sqrt{2Lnp_2^2\eta^2\lambda + L^2\eta^4\lambda^2}}{np_2} \tag{6.2}$$

for the grating period. Inserting the values described above, one gets $d_{1,25} = 24.8\,cm$ for 25 keV and $d_{1,35} = 34.5\,cm$ for 35 keV. In Tab. 6.1, all setup parameters are summarized.

6.2 Experimental Setup

Figure 6.1 illustrates the experimental setup. X-rays are generated by the MuCLS shown to the left. They are guided through the first experimental hutch and a beam tube (both not shown) to the second experimental hutch. The total distance from the interaction point to the detector plane is about 16 m. The sample stage is positioned 112 cm upstream of the detector plane and can be translated in the $xy-$plane as well as

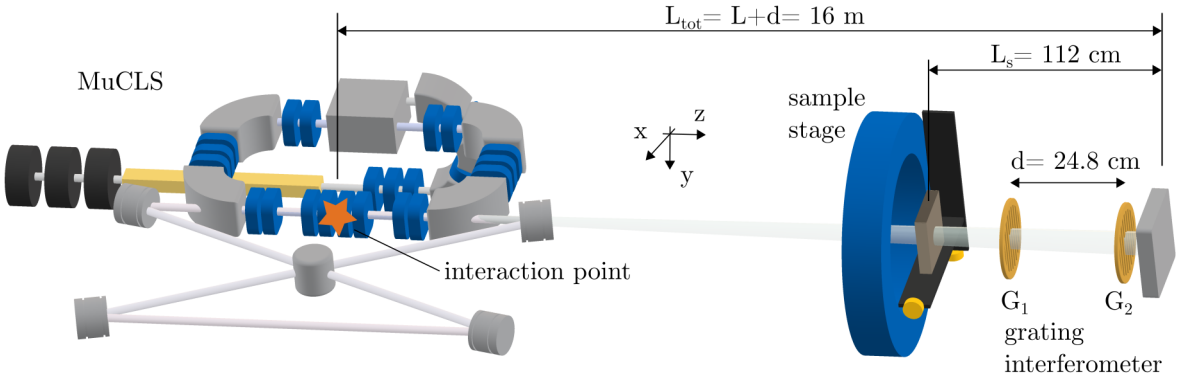

Figure 6.1: **Schematic overview of the experimental setup.** The MuCLS is sketched, x-rays are generated in the interaction point. The second experimental hutch is approximately 15 m downstream of the source point. The sample stage is positioned 112 cm upstream of the detector. The grating interferometer consists of a phase-grating G_1 and an attenuation grating G_2 located 24.8 cm downstream for the 25 keV configuration.

rotated around the optical axis. A photograph of the sample stage is shown in Fig. 6.2 a).

6.2.1 Grating Interferometer

The grating interferometer is sketched in Fig. 6.1 to the right, a photograph can be found in Fig. 6.2. Two different phase-gratings are available for design energies of 25 keV and 35 keV according to the specifications in Tab. 6.1. They were manufactured by the Karlsruhe Nano Micro Facility (KNMF) of the Karlsruhe Institute of Technology using the LIGA process [Becker, 1986; Bacher, 1995; Mohr, 2012]: a metallic seed layer and an x-ray photoresist are placed onto a flat substrate. The photoresist is then exposed to an x-ray beam which is partly blocked by a mask. Hence, the developed photoresist serves as a positive mask for the final structure. In the last step, the desired material is then plated upward from the metalized structure filling the voids left by the photoresist. In our case, the gratings are fabricated onto a silicon wafer. The phase-gratings G_1 are made of nickel with a height chosen such that a phase-shift of $\pi/2$ for the design energy is achieved. To simplify the fabrication process, the grating for 35 keV has a period of 4.92 µm similar to the phase-grating for 25 keV. A lower effective period matching the design specifications is achieved by tilting the grating by about 6.3°. The analyzer grating G_2 consists of gold bars with a height > 70 µm which attenuate over 90% of all x-rays emitted by the MuCLS. All gratings are round with a grating diameter of about 70 mm, which is sufficient to cover the full field of view.

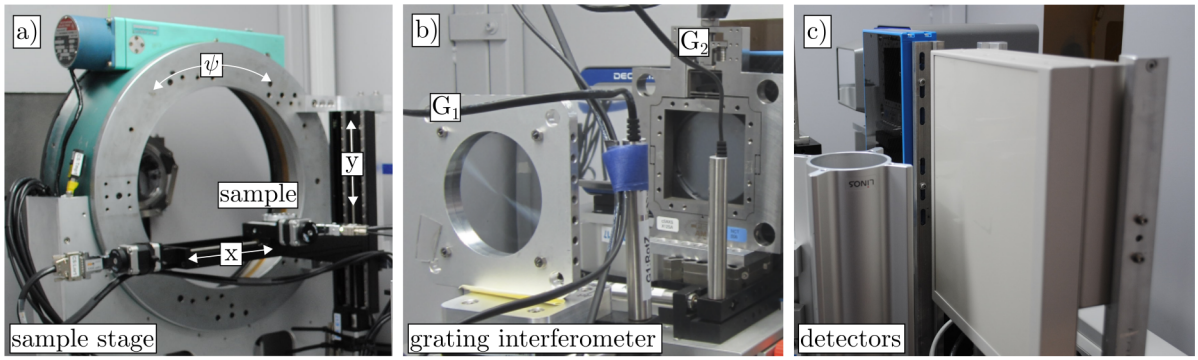

Figure 6.2: **Photographs of the experimental setup.** a) The sample stage is depcited. It is motorized in the xy-plane and can be rotated around the optical axis. b) A photograph of the gratign interferometer shows phase-grating G_1 and attenuation grating G_2. c) Up to three detectors can be mounted on a linear stage. Their parameters are described in Tab. 6.3.

A detailed overview of the grating parameters can be found in Tab. 6.2. All gratings are motorized to allow fine alignment of the interferometer, G_2 can be additionally translated in sub-micrometer steps along the x-axis to allow for the phase-stepping procedure.

6.2.2 Detectors

For the detection of x-rays, two flat-panel detectors and a photon-counting detector are available. A photograph is presented in Fig. 6.2 c), technical details are given in Tab. 6.3. Flat-panel detectors use scintillators to convert x-rays to visible light with an intensity proportional to the x-ray energy. Scintillator materials such as gadolinium oxysulfide (Gd_2O_2S) or cesium iodide (CsI) are chosen that have a high density and contain high-Z materials which lead to a high scintillator absorption efficiency. After conversion, the visible light is typically detected by an array of photodiodes. Flat-panel detectors are relatively inexpensive to produce, have a decent readout time and large field of views, which makes them the most common x-ray detectors. However, they cannot differentiate photons with different energies and hence intrinsically integrate different energies. Thicker scintillators with high scintillator absorption efficiency lead to a decreasing spatial resolution, dark-current, readout noise, and gain non-linearities reduce the image quality and have to be considered.

Photon-counting detectors directly convert an x-ray photon to a signal proportional to the photon energy. An incoming photon interacting with the sensor material causes some electron-hole pairs proportional to the x-ray energy. Dark-current as well as

	G_1(25 keV)	G_1(35 keV)	G_2
Period [µm]	4.92	4.92	5.0
Height [µm]	4.39	6.15	> 70
Material	Ni	Ni	Au
Duty cycle	0.5	0.5	0.5
Geometry	70 mm round	70 mm round	70 mm round
Substrate	525 µm Si	525 µm Si	525 µm Si

Table 6.2: **Grating parameters for the experimental setup.** For both design energies, the source distance $L = 15\,\text{m}$ and a phase shift for G_1 of $\pi/2$ ($\eta = 1$) were given. For the first Talbot order $n = 1$, the Talbot distance and phase-grating period p_1 follow from Eq. (6.1) and Eq. (6.2), respectively.

readout noise is avoided by only counting signals if a calibrated threshold is exceeded. Readout noise is avoided because photon-counting detectors are not integrating over a certain readout time but count every single photon. This leads to a box-like point spread function and high frame-rates which can exceed 100 fps. Spectral resolution is physically possible but currently very limited due to the low number of available energy bins. Disadvantages are the currently smaller FOVs and the complex detector technology.

For the MuCLS, the flat-panel detectors are equipped with a Gd_2O_2S scintillator of different thicknesses, the photon-counting detector has a silicon sensor. The resulting scintillator absorption efficiency is depicted in Fig. 6.3. It is relatively high at lower energies and for the flat-panel detectors. For 25 keV, efficiencies between 56% - 95% are achieved for the Pilatus 200k and Varian PaxScan 2520DX detector, respectively. The scintillator absorption efficiency decreases for higher energies to 15% - 68%. However, this could be overcome by using a different scintillator or sensor type. For the photon-counting detector, gallium arsenide (GaAs) provides an alternative to silicon with higher quantum efficiencies within the energy range relevant for the MuCLS.

6.3 Setup characterization

6.3.1 Simulation

The setup performance was also accessed using a simulation framework based on Fresnel propagation. Some theoretical foundations are described in [Bech, 2009, p. 13-16]. The implementation used for this simulation was implemented by Manuel Viermetz. According to the Huygens-Fresnel principle, each position of a propagating wave-front

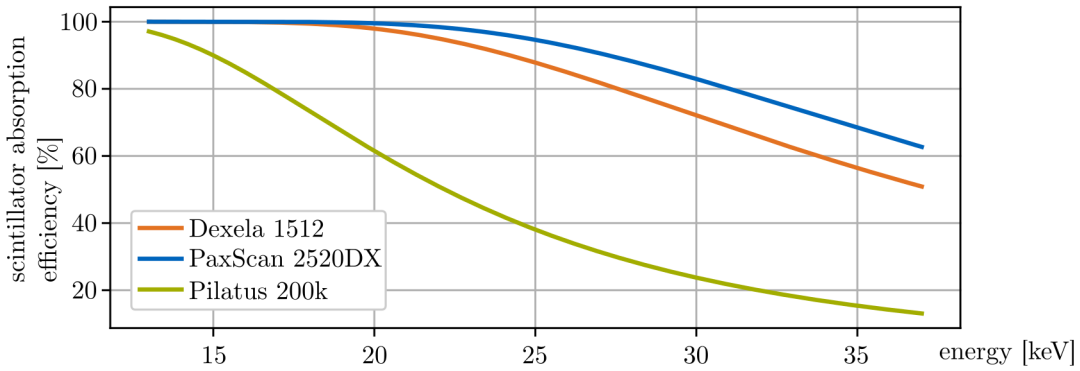

Figure 6.3: **Detector scintillator absorption efficiency vs. energy.** The flat-panel detectors both have a gadolinium oxysulfide scintillator with different thickness. At 25 keV, they have a high scintillator absorption efficiency up to 95%, whereas the Pilatus 200k only reaches 38% and drops to 15% at 35 keV. For this energy, the gadolinium oxysulfide scintillator has still efficiencies up to 68%.

is again a source of a spherical wavelet. The wave-front at a later point is than given by the superposition of all spherical waves, leading to the Fresnel diffraction integral. The simulation assumed plane waves which are emitted by an idealized source. To adapt the results for a cone-beam geometry, we used the Fresnel scaling theorem [Paganin, 2006]. A phase-stepping was simulated simply by a convolution of the wave-front intensity within one pixel with a box-function representing the analyzer grating G_2.

In Fig. 6.4, the simulation for a design energy of 25 keV and the corresponding grating parameters are illustrated in the upper half. On the bottom, a simulation is depicted for a design energy of 35 keV and grating parameters as described in Tab.6.2. The distance from the source to sample was set to 16 m. The visibility was calculated directly from the maximum and minimum intensity. This is favorable since stepping curves approach a triangular function for very high visibilities at the design energies [Bech, 2009, p. 29]. Away from the design energy, the assumption of a sinusoidal stepping curve is not valid as well. Hence, it is more accurate not to fit a theory curve to the simulated data. The error made by only using discretized points instead of a continuous theory curve can be minimized by using a large number of steps.

The simulated visibility had a value of 85.2% at the design energy of 25 keV, corresponding to the maximum visibility for both energy configurations. For the design energy of 35 keV, a visibility of 72.2% was simulated. Following a vertical slice for a constant inter-grating distance, the visibility slowly varies with changing energy. The maximum is found along the slice roughly at a straight line connecting both design

Manufacturer Model	Dectris Pilatus 200k	Perkin Elmer Dexela 1512	Varian PaxScan 2520DX
Type	photon counting	CMOS	thin film transistor
Scintill./Sensor	1000 µm Si	150 µm Gd_2O_2S	208 µm Gd_2O_2S
Field of view	487x407 px 17 px gap	1536 x 1944 px	1536x1920 px
Square pixel size	172 µm	74.8 µm	127 µm
Eff. pixel size	159.9 µm	69.6 µm	118.3 µm
Dynamic range	20 bit	16 bit	14 bit
Detector PSF	1x1 px rectangular	0.95x0.95 px Gauss	1.19x1.15 px Gauss

Table 6.3: **Overview of all detectors available for experiments.** Due to a gap in the FOV, the photon counting detector was mostly used for beam characterization but not for directional measurements.

energies. Linear interpolation in between both configurations leads to

$$d = 9.7\frac{\text{mm}}{\text{keV}}\,E + 5.5\,\text{mm}\,, \tag{6.3}$$

where d is the inter-grating distance and E is the x-ray energy. Eq. (6.2) can be used as a guide if the interferometer is operated at arbitrary energies between the design energies. In this case, the grating configuration closest to the current energy should be used.

6.3.2 Setup Stability

Any grating interferometer relies on precise alignment of its optical components. For the MuCLS, the magnified interference pattern downstream of G_1 should match the analyzer grating period. Since this cannot be achieved perfectly, a Moiré pattern will be visible. In this situation, even minor changes in the interferometer alignment can drastically alter a measurement. Hence, vibrations even with small amplitudes in the micrometer regime as well as thermal changes have to be considered and eliminated as far as possible. Source instabilities such as source drifts, changes in spot sizes and thus coherence and flux variations can influence the interferometer as well.

As a first step, the x-ray flux was recorded for an extended period without placing any optical elements in the beam path. The resulting mean flux within a region of interest is depicted in Fig. 6.5 for three different exposure times, the standard deviation within a single time frame is given by the shaded area around the curve. For very short exposure times of 0.1 s, variations of the mean flux of up to 10 % are observed. For

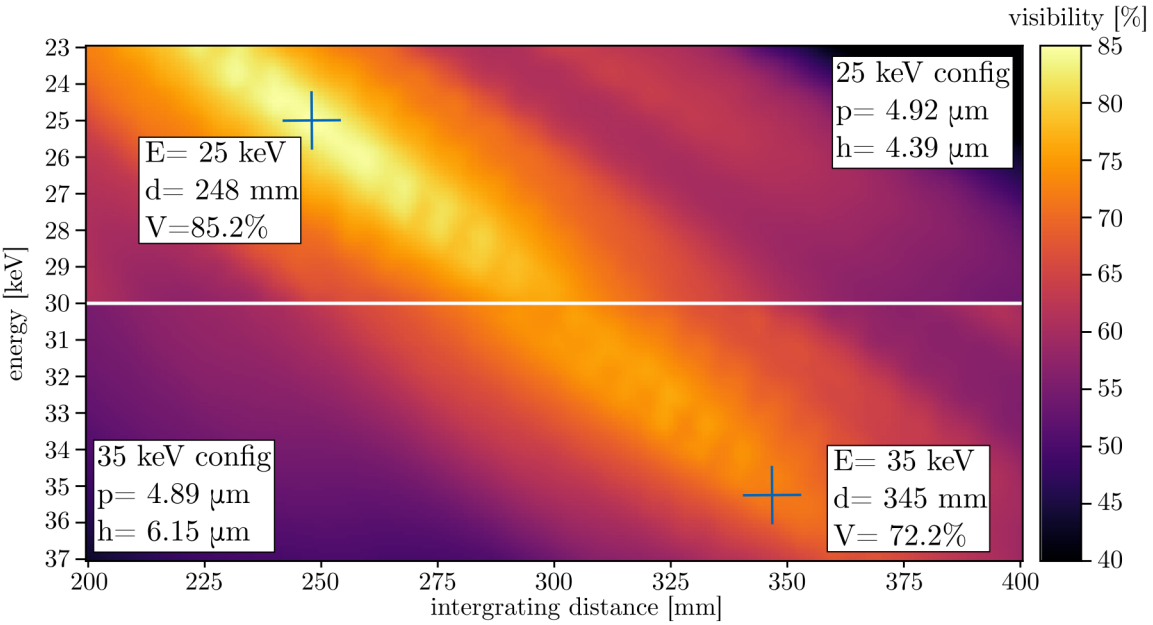

Figure 6.4: **Simulated visibility depending on the energy and inter-grating distance.** The simulation was based on values reported in Tab.6.1 and Tab. 6.2. For 25 keV, illustrated on the top, the visibility had a maximal value of 85.2%. This corresponds to the global maximum found for both simulation configurations. The design energy of 35 keV is shown on the bottom, and it yielded a maximal visibility of 72.2%.

the most commonly used exposure time of 1 s, the mean flux still varies for about 2.5 % and even for long exposure times of 10 s, a visible change in the mean flux is detected. To account for these variations, a reference area not altered by interference effects was used to normalize flux variations. Such a region can be found in the grating substrate (see Fig. 6.6 a)), which was subsequently used as flux reference in single phase-stepping curves as well as between sample scans and reference scans. To investigate source movements, the grating interferometer was installed. The center of mass of a line plot through the resulting Moiré pattern was now used as a measure for the source movement. In Fig. 6.6 a), different scenarios can be seen: curve i) depicts a reference curve where the setup was not influenced at all, showing a smooth drift of the center of mass. In a measurement, this would alter the measured phase signal in a phase-contrast measurement and can be corrected by taking frequent reference scans. Additionally, a simple offset or even a polynomial offset can be subtracted if a large enough background region is available with a known phase. Curve ii) depicts two discontinuities, which could be correlated to operator interactions with the MuCLS. Such interventions are often necessary to correct for thermal drifts or decreasing flux

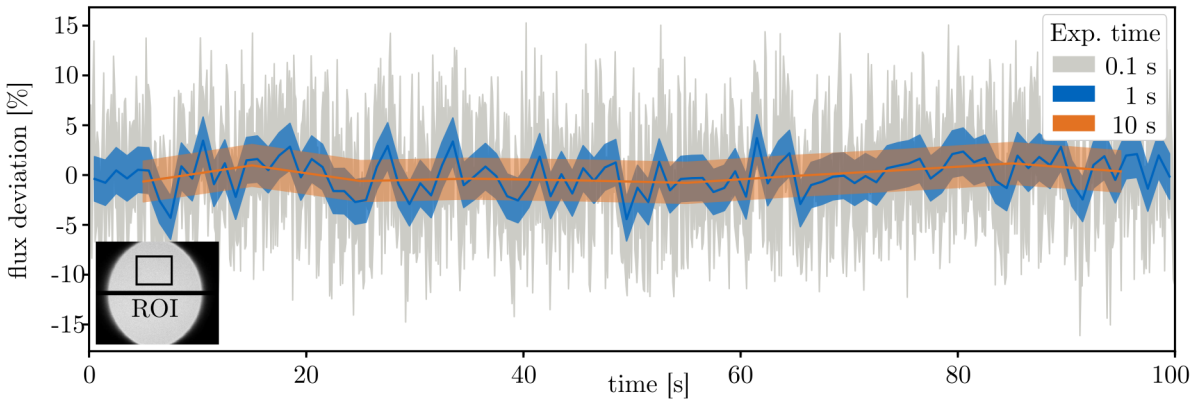

Figure 6.5: **Stability of x-ray flux over time.** The flux variation is plotted for exposure times of 0.1 s, 1 s and 10 s exposure time. Histogram data within a given region of interest was fitted by a Gaussian function for each time step. The solid line corresponds to the mean value, the colored area to the standard deviation. For clarity, only the area indicating the standard deviation is given for the exposure time of 0.1 s.

levels but can mostly be avoided during measurements. Live feedback loops that were stabilizing the x-ray source position, however, were found to have no influence. During the third measurement iii), the experimental hutch was mechanically disturbed. The higher magnitude compared to the other curves indicate the transmission of vibrations to the interferometer. This issue could be solved by installing additional damping feet for the optical table, although mechanical disturbances close to the setup could still be sensed. However, the soft table damping led to a coupling between the interferometer phase and motor positions, i.e., movement of masses on the table. This behavior was investigated by analyzing the phase of a reference phase-stepping, which was found to be a sensitive quantity. As can be seen in Fig. 6.6 b), motor movement without decoupling the sample stages, as shown in curve iv), induced a strong change in phase which would make it impossible to correlate two different measurements, e.g., a sample scan and a reference scan. As a consequence, all sample stages were mounted on a separate support structure and hence completely decoupled from the optical table. This drastically increased the setup stability as can be seen in plot v) and vi). As a reference, a scan without motor movement is presented in plot vii). It increases linearly over time, which can be corrected by frequent reference scans as mentioned before. This could be a result of thermal drifts which affect the interferometer on relatively long timescales. Such drifts are taken into account by regularly acquiring reference scans.

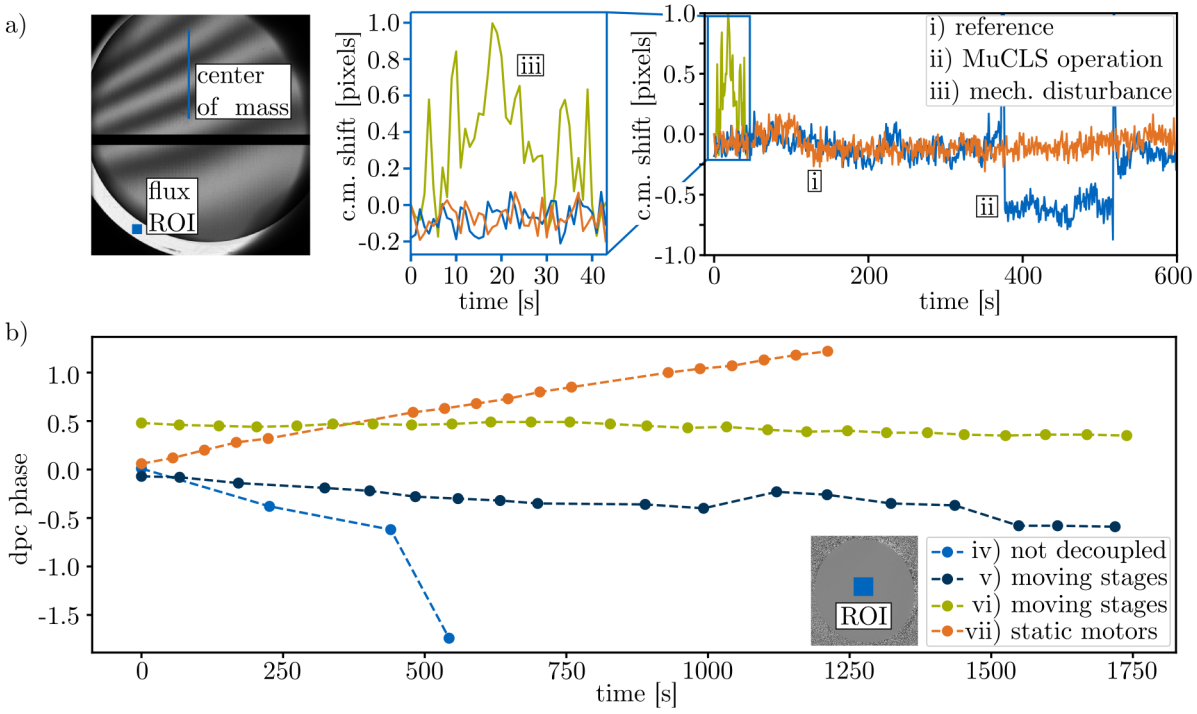

Figure 6.6: **Stability characterization of the grating interferometer.** a) Center-of-mass movement of a line-plot through the Moiré pattern without interfering with the setup i), with operator intervention at the MuCLS ii) or mechanically disturbing it iii). b) Average stepping-curve phase in a region of interest with moving sample stages directly mounted on the optical table iv) or decoupled v) and vi). Graph vii) is a reference without motor movement.

6.3.3 Phase-Contrast Imaging

The theoretical principles of phase-contrast imaging are described in chapter 4. In this section, the practical measuring routine is described as well as its processing. A schematic overview of the measurement routine is illustrated in Fig. 6.7.

Data Acquisition

To fit a sinusoidal curve with a known period, a minimum of 3 sampling points are required with different positions x_g of the analyzer grating G_2. This is done by a so-called nanoconverter, which mechanically transmits a stepper motor movement to a sub-micron lateral grating. In our case, typically 5 images are acquired equally distributed over a grating phase 2π, i.e., $x_g/p_2 = \{0°, 72°, 144°, 216°, 288°\}$. For a single phase-contrast projection, two image stacks are acquired in total. One with the sample in place and an empty one as a reference.

Preprocessing

Prior to the actual processing, the raw data must be corrected for dark-current, readout noise, and flux variations. Because count rates are always positive, those effects accumulate over time and lead to a signal even in the absence of a photon beam. Although it is negligible for photon-counting detectors, flat-panel detectors have significant dark-currents that need to be corrected. Hence, the dark-current and readout noise are experimentally determined by a measurement with similar exposure times as used for the actual measurement but with a closed shutter. The corresponding image is subsequently subtracted from the raw data, as can be seen in Fig. 6.7.

Depending on the exposure time, the flux might vary up to 15 %, as discussed in 6.3.2. This can be corrected by normalizing the flux in a given ROI for each measurement. Figure 6.7 shows an empty image with an ROI marked by an orange square. It is placed outside the overlapping region of both gratings to exclude interference effects from the flux measurement.

After the flux is corrected, it is possible to crop the data to a smaller size which only contains a region of interest. This reduces the amount of stored data and highlights interesting sample features.

Processing

At this point, we are left with two image stacks for sample scans and reference scans, respectively. In each pixel, this results in a sinusoidal stepping curve given by Eq.(4.6),

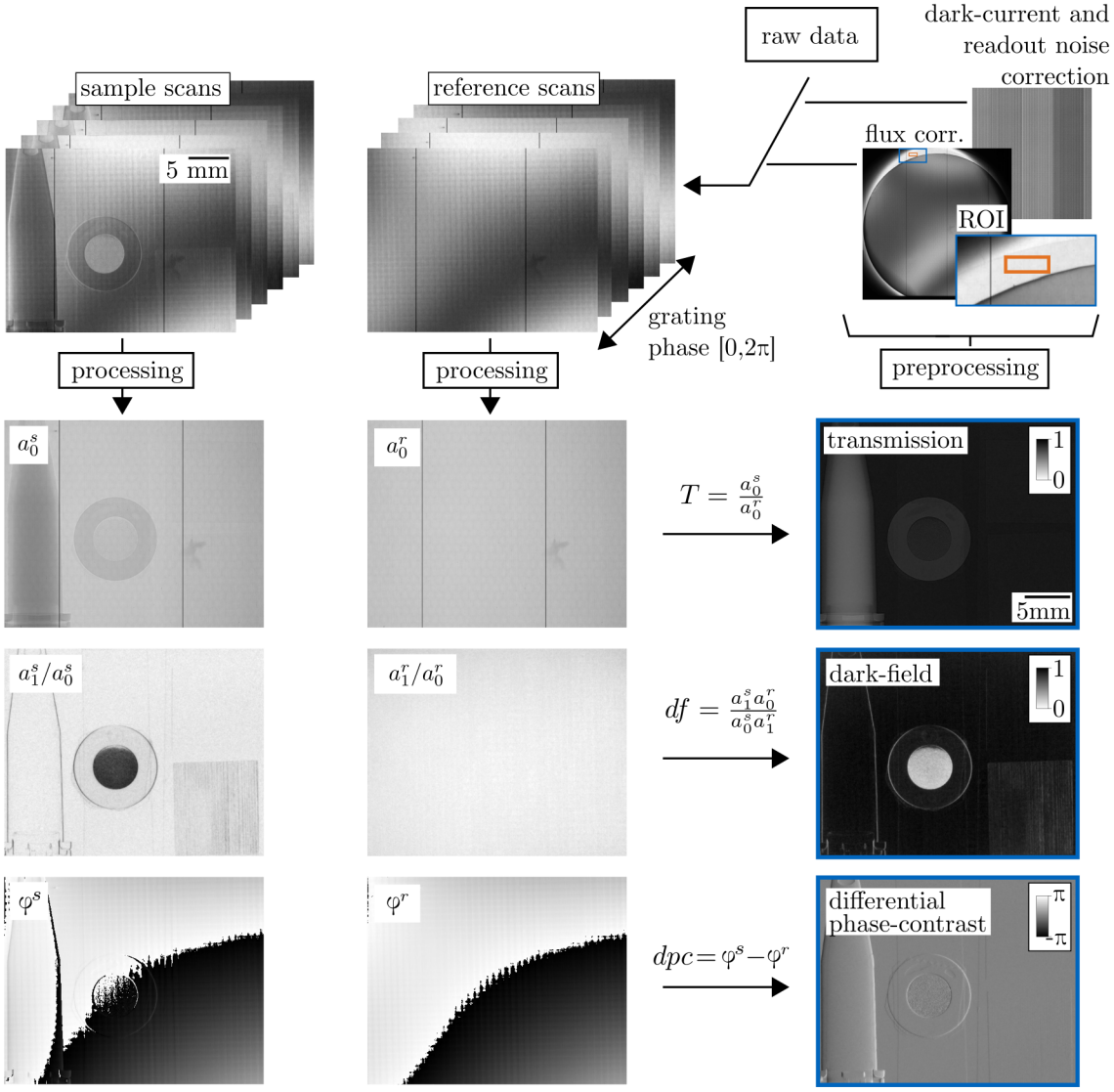

Figure 6.7: **Schematic overview of a phase-stepping measurement.** The raw data is corrected for dark-current, readout noise, and flux variations. This results in two image stacks, one with sample in place and an empty reference scans. Both stacks covers at least three different positions of the analyzer grating. A sinusoidal curve is fitted to the resulting phase-stepping curve in each pixel and yields the fit parameters a_0, a_1 and ϕ. A comparison of the fit parameters found for the sample scan and the reference scan yields the attenuation, dark-field and phase-contrast images.

which can be fitted by fit parameters a_0, a_1 and ϕ. There are several possibilities to get the fit parameters.

The most straightforward and fastest approach is to consider Eq.(4.6) as part of a Fourier power series, which would be a generalization to arbitrary stepping curves. If higher orders are negligible, the fit parameters are given by the first order Fourier coefficients [Bech, 2009, p. 35]. A least square fit to the data yields the same result but is more computationally expansive. However, the residuals provide a measure of the fit accuracy. The most elaborate algorithm, routinely used for data shown in this thesis, is based on expectation maximization [De Marco, 2015, p. 58]. A statistical model function $f(p)$ with parameters p is optimized by minimization of a particular cost function. This can correct for inexact grating positions and even missing steps and reduces remaining fringes and thus artifacts [Marschner, 2016].

Signal Extraction

Once the fit parameters are given for both the sample scans and the reference scans, they can be related to different physical quantities as described in section 4.3. The ratio of $T = a_0^s/a_0^r$ thereby corresponds to the transmission, the dark-field is defined as $df = a_1^s a_0^r / a_0^s a_1^r$, and the differential phase-contrast is defined as $dpc = \varphi^s - \varphi^r$. The corresponding final images are illustrated in Fig.6.7.

6.3.4 Visibility

The grating interferometer performance can be quantified by investigating a stepping curve with an empty beam. Figure 6.8 shows the result of such a measurement for 25 keV design energy to the left and 35 keV to the right. The data has been measured with the Dexela 1512 detector and illustrates four images for the fit parameters as well as the visibility. In the bottom of Fig. 6.8, a sample stepping curve is presented with the respective fit curve, the data is shown twice to emphasize the signal periodicity. For a region of interest in the center, the mean visibility is determined as 47 % for 25 keV and 32 % for 35 keV. This qualitatively matches the simulation, which predicts a visibility drop for the 35 keV configuration as well. However, an ideal source as assumed in the simulation leads to higher theoretical visibilities of up to 85.2% which are not met in practice. Quantitatively, also the relative visibility drop of 32% exceeds the simulated 16%. This can be explained by the tilted G_1-grating for the 35 keV configuration, which is necessary to achieve an effective period of 4.89 µm. Thus, it is not possible to align the grating perpendicular to the x-ray beam and to bring it in an optimized distance to G_2. Another factor is the finite source size, which in practice reduces the spatial visibility. Moreover, monochromatic measurements ignore the fact that the spectrum

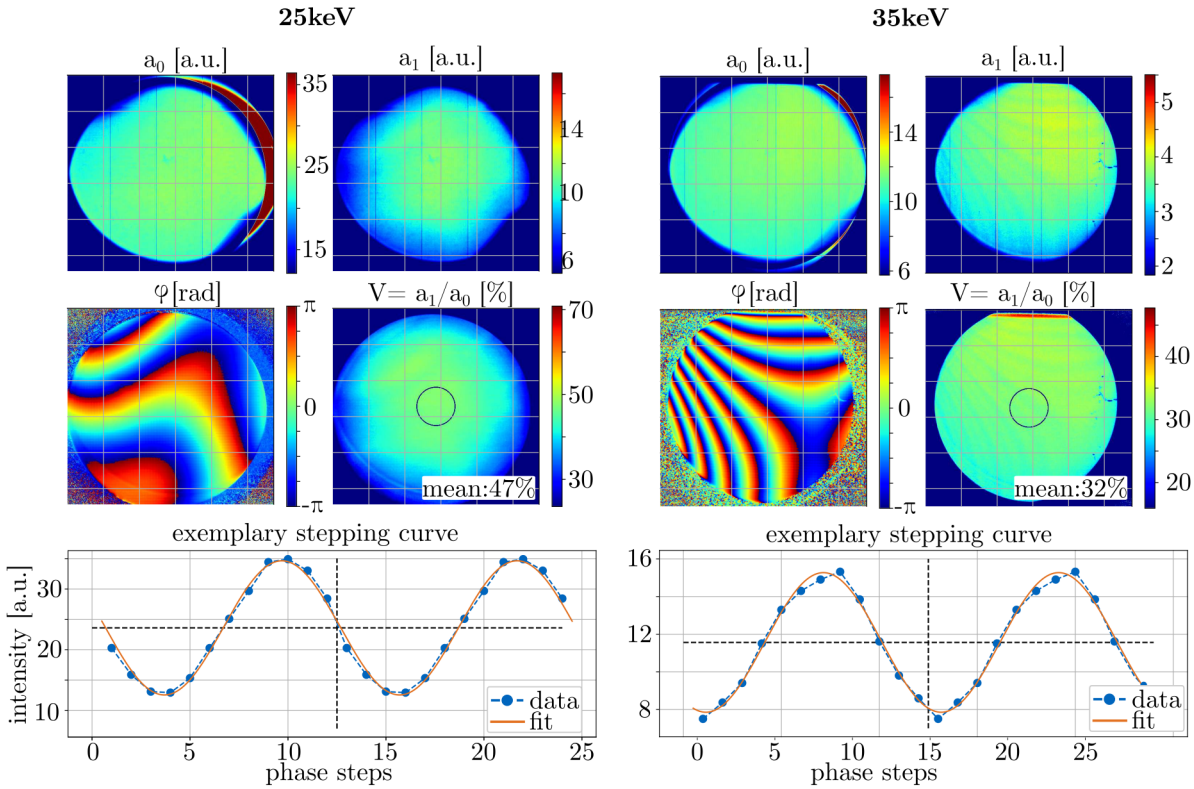

Figure 6.8: **Reference measurements for 25 keV and 35 keV design energy.** The images on the top correspond to different fit parameters of the sinusoidal stepping curve a_0, a_1, φ, and the visibility V (see Eq. (4.6)). The stepping curve visibility is homogeneous for both setups with a mean value in the center of 47 % for 25 keV and 32 % for 35 keV. At the bottom, a sample stepping curve is depicted for a single pixel together with a fit to the data.

at 35keV is broader compared to 25keV. Hence, low-visibility photons have a higher weight in the spectral average.

In Fig. 6.9, the visibility is depicted as a function of energy. The spectrum was detected with the spectral detector KETEK AXAS-D (KETEK GmbH, Munich, Germany). It is a silicon drift detector with a sensor of 450 µm thickness. To account for the detector dead time, an aluminum block with a thickness of 1.395 cm was inserted close to the source. Its thickness was chosen such that the ratio of the detector live time and the total measurement time was over 95%. The grating G_2 was moved by two periods (i.e., a phase of 720°) in 28 steps, a spectrum with 120 s exposure time was recorded for each step. In Fig. 6.9 a), four spectra are plotted for different G_2-phases. They are normalized to the maximum number of counts found for all spectra and corrected for the aluminum filter, i.e., they show the spectrum at the detector position. For each energy bin, a stepping curve is constructed by stitching together the corresponding phase positions, as depicted in Fig. 6.9 b) for four energies. The visibility is subsequently calculated from a fit to the stepping curve as described in section 4.3. Finally, this leads to the visibility as a function of energy presented in Fig. 6.9 c). The visibility rises with increasing energy, and the mean visibility integrated over the spectrum is 23.7%.

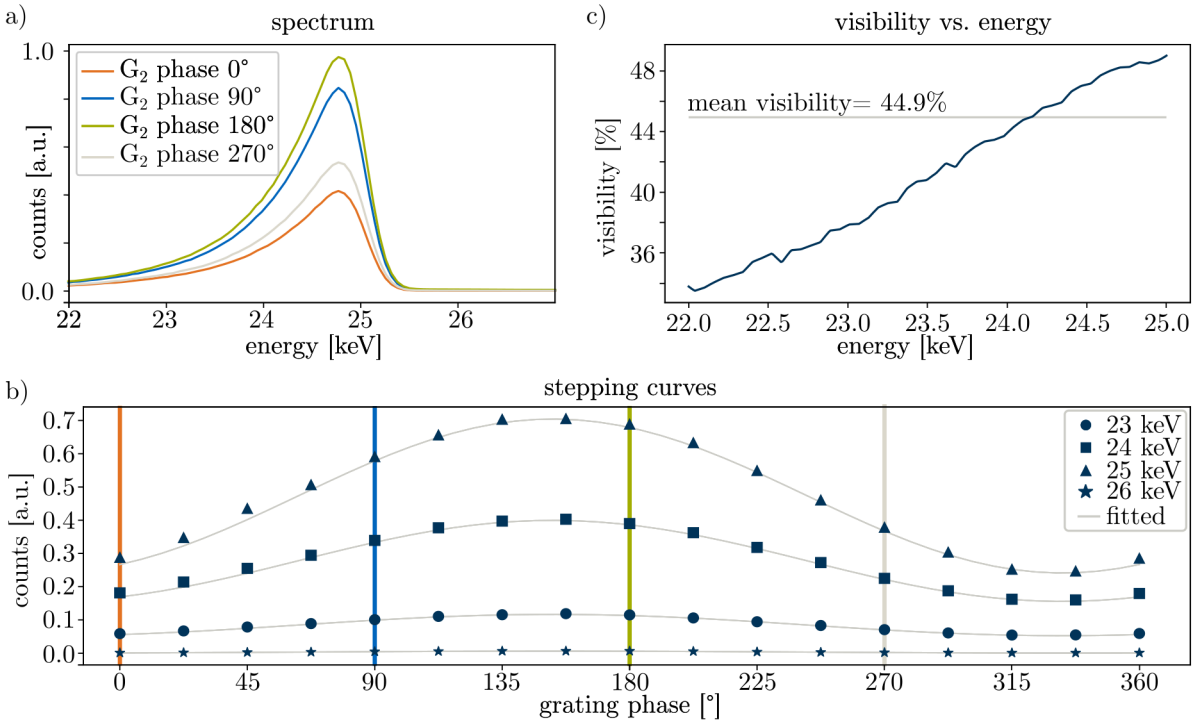

Figure 6.9: **Visibility as a function of Energy.** a) Four spectra with different grating positions are plotted. b) This leads to a stepping curve for each energy bin, shown for four different energies. c) The visibility grows linearly with increasing energy, the mean visibility for energies integrated from $22\,\mathrm{keV} - 27\,\mathrm{keV}$ is 23.7%.

Trabecular Bone Anisotropy Imaging 7

This chapter presents a proof of principle study highlighting the potential of x-ray vector radiography for bone imaging. The results have been previously published in the following article and parts of the following text are adapted from this article:

Jud *et al.* [Jud, 2017]

7.1 Motivation

Conventional x-ray radiography is a standard diagnostic technique in clinical trauma imaging, providing a high diagnostic accuracy for fractures of the cancellous bones of the extremities. In Germany, 1.7 x-ray investigations per person and year are made [Stelljes, 2016], but it is estimated that in such radiographs about 3.7 % of all fractures in the extremities might be missed [Wei, 2006]. Such radiographically occult or subtle fractures may delay the healing process or cause further complications. Hence, advanced imaging techniques such as grating-based x-ray imaging could be used in such cases.

Many pre-clinical studies have shown that DPC, DFC, and related imaging techniques can improve medical imaging tasks such as mammography [Stampanoni, 2011; Scherer, 2015b], kidney stone classification [Scherer, 2015a] or diagnosis of coronary atherosclerosis [Hetterich, 2017]. For lung imaging in mice, DFC could detect lung diseases at an early stage [Yaroshenko, 2013]. Although first studies demonstrate the feasibility of *in vivo* DFC lung imaging for larger animals [Gromann, 2017] and even human cadavers [Willer, 2018], there is still a need for clinical studies to ultimately show clinical utility. For the extremities, *in vivo* measurements of human fingers investigated metacarpolohangeal joints [Tanaka, 2013]. Focusing on the phase-contrast image, they detected cartilage which would be oblique in the attenuation contrast channel. Thuering et al. investigated dark-field radiographs of human cadaver hands and could show improved diagnostic value [Thüring, 2013b].

Single dark-field images, however, mostly detect scattering information in one distinct sensitivity direction orthogonal to the grating lines. As described in chapter 5, x-ray vector radiography (XVR) exploits this dependency to gain additional image information. Therefore, it yields both orientationally averaged mean scattering as well as

directional scattering information such as the degree of anisotropy and the main scattering orientation (see also chapter 5) [Jensen, 2010b; Jensen, 2010a; Revol, 2012; Malecki, 2013; Lauridsen, 2014]. Another advantage of XVR is that scattering properties of microstructures are probed without the need for high spatial resolution, which was shown by Potdevin *et al.* [Potdevin, 2012] for human vertebral bone samples. Later, Schaff *et al.* [Schaff, 2015a] directly correlated bone microstructures of human femur bones to XVR. A connection between the degree of anisotropy and femoral bone strength as well as an improved prediction of vertebral failure load indicated the potential of XVR for osteoporosis imaging [Eggl, 2015]. However, all investigations so far have been performed with isolated samples of limited size.

In our proof of principle study presented in this chapter, we show a correlation between XVR and bone morphology changes for an *ex vivo* human hand. The sensitivity to changes in microstructures highlights the potential of XVR for the detection of radiographically occult fractures.

7.2 Materials and Methods

The measured sample was an *ex vivo* human hand provided by a human donor who had given written consent to provide the body after deceasing for medical education and research according to international ethical guidelines and according to German law. From the hand, a single finger was separated, and both samples were embedded in 2 % formalin solution. During the measurement, the finger was fixated in a Falcon^{TM} tube, whereas the hand was fixated in a dedicated sample holder as shown in a photograph in Fig. 7.1 a).

The Munich Compact Light Source (cf. Chapter 2) was tuned for 25 keV with a flux of about $\phi = 0.42 \cdot 10^{10}$ photons/s and a source size (horizontal/vertical) of $\sigma = 42\,\mu m/46\,\mu m$. A grating interferometer was installed as described in chapter 6, i.e., a phase-grating with $p_1 = 4.92\,\mu m$ and an analyzer grating with $p_2 = 5.00\,\mu m$. The inter-grating distance was 248 mm, leading to a fringe visibility of 49 %. A photograph of the grating interferometer can be found in Fig. **??**. For the detection of x-rays, a Varian PaxScan 2520DX with an effective pixel size of 118.3 µm was used, its detailed specifications can be found in Tab. 6.3.

For the finger, a single phase-contrast projection was acquired using 12 phase-steps with an exposure time of 1 s each. In total, 16 sample orientations around the optical axis with $\psi = \{0°, 12°, 24°, ..., 168°, 180°\}$ were recorded over a range of 180°, summing up to a total number of 192 acquisitions. The human hand was measured with the same setup. However, in this case, 7 phase-steps were used with exposure times manually varied between 0.5 s and 10 s to take into account sample thickness variations. Four

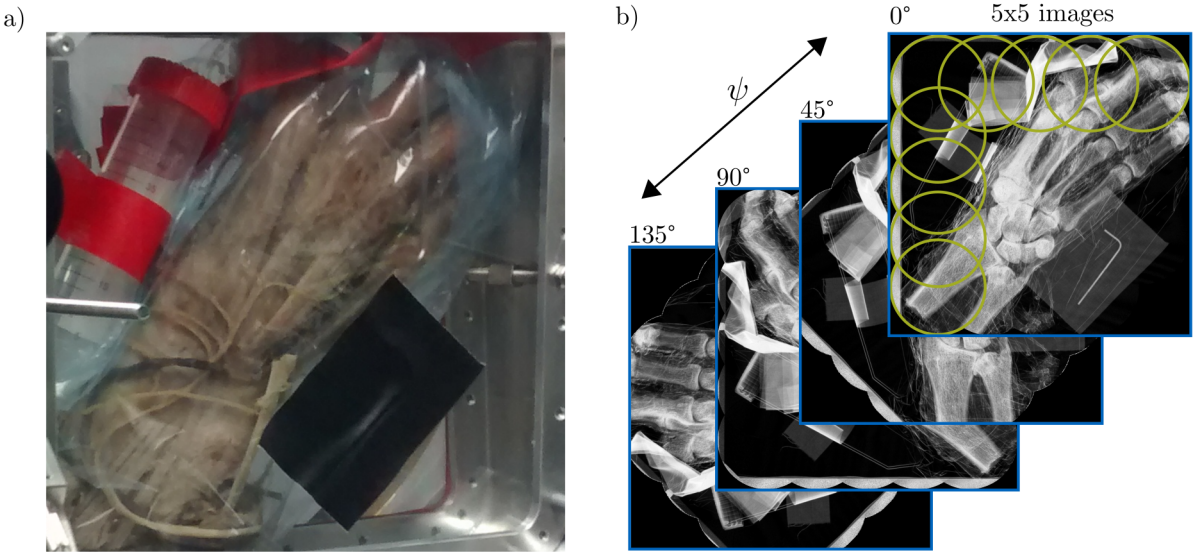

Figure 7.1: **Photograph of human cadaver hand sample and image acquisition.** a) The sample is fixed in between two plates in a dedicated sample holder, several well-defined objects are used as reference to improve image stitching. b) The sample was covered by 5×5 stitched phase-contrast projections, four different sample orientations around the optical axis were acquired for the XVR.

different sample orientations with $\psi = \{0°, 45°, 90°, 135°\}$ were measured as illustrated in Fig. 7.1 b). Since the field of view (FOV) of a single phase-contrast projection could not cover the whole sample, a raster of 5×5 projections was stitched together. The stitching algorithm relied on the effective pixel size and the known sample displacement to calculate the shift in pixels.

Finally, the sinusoidal dependence of the dark-field signal was analyzed as described in chapter 5, which yielded the mean scattering strength, degree of anisotropy and the orientation of scattering structures in addition to the attenuation.

7.3 Results

Figure 7.2 on page 59 shows the index finger of the *ex vivo* human hand. Different anatomical details such as the intermediate phalanx, the distal phalanx, and the proximal phalanx are visible as indicated in part e). The first row depicts a frontal view and the second row a lateral view. In a) and e), the integrated attenuation coefficient shows the typical anatomy of long bones with outer cortical bone and internal trabecular structure. Two colored regions of interest (ROIs) are used to extract quantitative values from a Gaussian fit to the histogram data within the ROI. The same ROIs were used for all frontal projections to extract quantitative data, the values are summarized in Tab. 7.1. The mean scattering strength ϵ, shown in part b) and f), is low in the diaphysis compared to a higher value in the epiphysis, i.e. close to the joint. The difference between diaphysis and epiphysis is most pronounced for the degree of anisotropy, depicted in c) and g). However, unlike the other contrast modalities, it is lowest in the epiphysis and higher in the diaphysis. The quantitative evaluation yields mean values of $da_{red} = 0.25 \pm 0.03$ and $da_{blue} = 0.09 \pm 0.09$, respectively. The highest anisotropy value is found at the transition from the bone to the liquid-filled joint. Part d) and h) present the orientation of scattering structures color coded according to the color wheel shown in the bottom left, the brightness encodes the degree of anisotropy. The scattering structures are predominantly oriented in the longitudinal direction. An exception is the transition between bone and joint, where the highly anisotropic signal is oriented parallel to the surface.

The *ex vivo* human hand measurement is shown in Fig. 7.3 on page 61. Its bones can anatomically be divided into long bones like the metacarpals, radius, ulna, and short bones including all carpals. In the attenuation image shown in a), it can be seen that the index finger covers the thumb. Hence, the sample was not fully penetrated in this region and contains less information. In the mean scattering signal depicted in b), no clear variation is found between different bone parts. As can be seen in part c), however, the degree of anisotropy strongly varies in different bone regions. ROIs for quantitative evaluation are indicated similar to the previous sample, their

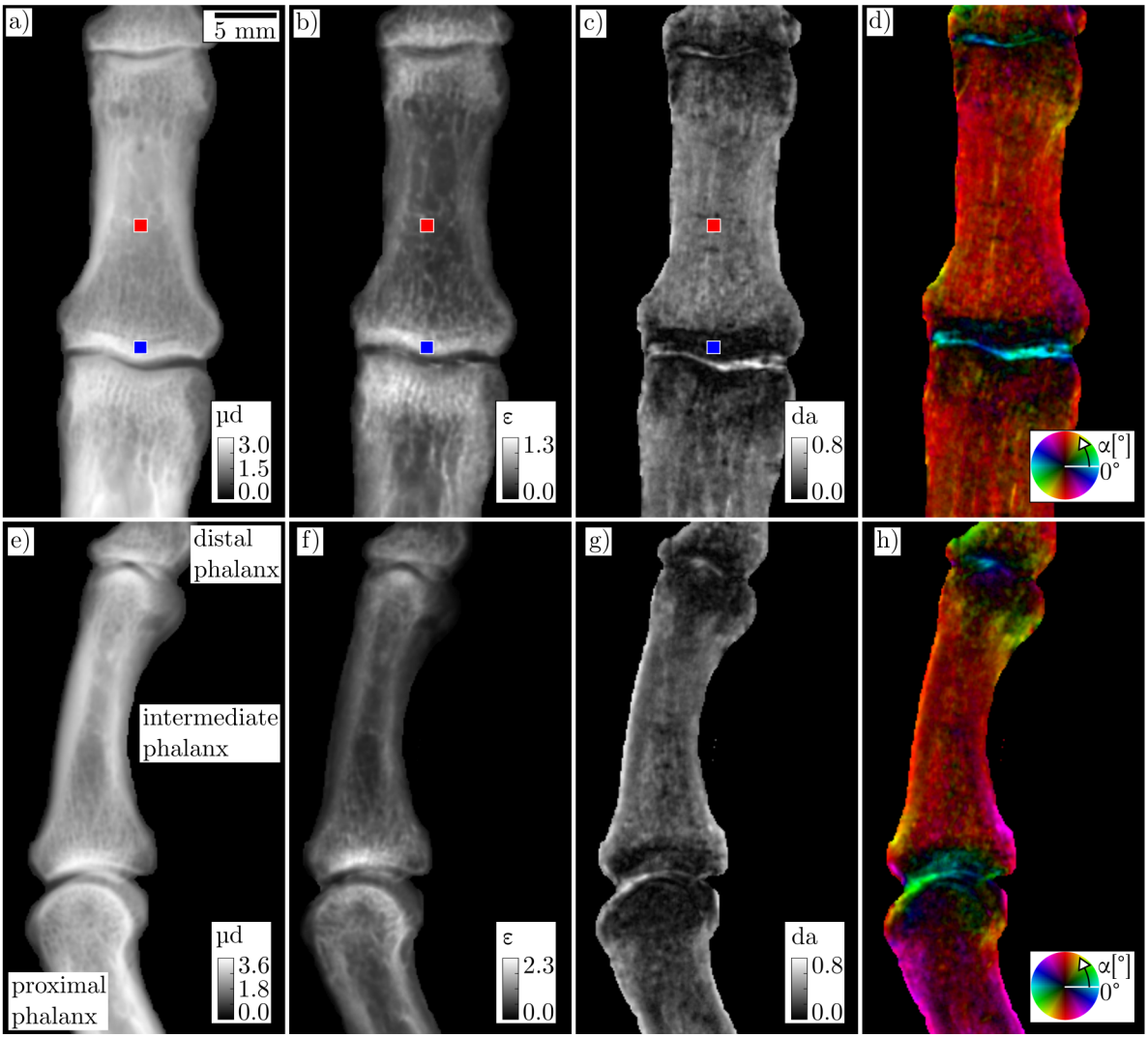

Figure 7.2: **X-ray vector radiography of a human index finger.** A frontal view is presented in the first row (a-d), the second row depicts a lateral view. The head of the proximal phalanges, the intermediate phalanges and the base of the distal phalanges are visible. Part a) and e) show the integrated attenuation coefficient, the mean scattering strength is depicted in b) and f). Parts c) and g) illustrate the degree of anisotropy, its mean values in the colored ROIs are $da_{\text{red}} = 0.25 \pm 0.03$ and $da_{\text{blue}} = 0.09 \pm 0.09$. Quantitative values for all contrast modalities are given in Tab. 7.1. d) shows the orientation ϕ of scattering structures color-coded according to the color wheel. The brightness corresponds to the degree of anisotropy.

ROI	$\mu\, d$	ϵ	da
Finger (red)	1.8 ± 0.4	0.30 ± 0.02	0.25 ± 0.03
Finger (blue)	2.3 ± 1.3	0.99 ± 0.04	0.09 ± 0.09
Hand (cyan)	3.06 ± 0.08	0.33 ± 0.13	0.26 ± 0.04
Hand (purple)	4.82 ± 0.18	2.03 ± 0.16	0.09 ± 0.05
Hand (green)	3.72 ± 0.11	0.85 ± 0.19	0.39 ± 0.11

Table 7.1: **Quantitative image values in different regions of interest (ROIs).** The attenuation, mean scattering strength and degree of anisotropy are depicted for the ROIs in Fig.7.2 and Fig.7.3. The mean value and standard deviation was obtained by a Gaussian fit to the image histogram.

respective values can be found in Tab. 7.1. While the epiphysis has a low degree of anisotropy of $da_{purple} = 0.09 \pm 0.05$, it is higher in the diaphysis with a value of $da_{green} = 0.39 \pm 0.11$. A high value can be found in the metacarpal bones as well with a value of $da_{cyan} = 0.26 \pm 0.04$, which is comparable to the intermediate phalanges already shown in Fig. 7.2. The carpals all have a low degree of anisotropy without strong variation. In accordance with the observation for the human finger, a high degree of anisotropy is found at the transition from the bone to the joint. Part d) shows the orientation of scattering structures. In order to suppress isotropic sample regions, the brightness is encoded by the degree of anisotropy. The carpal bones have a very isotropic orientation of scattering structures in contrast to radius, ulna and the metacarpal bones which have longitudinally oriented structures. Regions with a low degree of anisotropy have a less pronounced orientational preference. The joint regions, the scattering structures are oriented along the bone edge as found in Fig. 7.2 d) for the finger.

7.4 Discussion

In contrast to attenuation, the mean scattering provided by XVR is sensitive to ultra-small-angle scattering and hence to sample morphology. The bony structure mainly consists of a spongy trabecular matrix with multiple interfaces, which are responsible for a high scattering effect on the x-ray beam. Cortical bone consists of a dense arrangement of multiple cylindrical units, so-called osteons. Each osteon has a central canal which serves as a vascular channel for bone nutrition. Thus, multiple interfaces between individual osteons with central canals lead to a high scattering signal of cortical bone. All of this results in a homogeneous mean scattering signal of the epiphysis and diaphysis in the long bones and within the carpals. Variations in the mean scattering

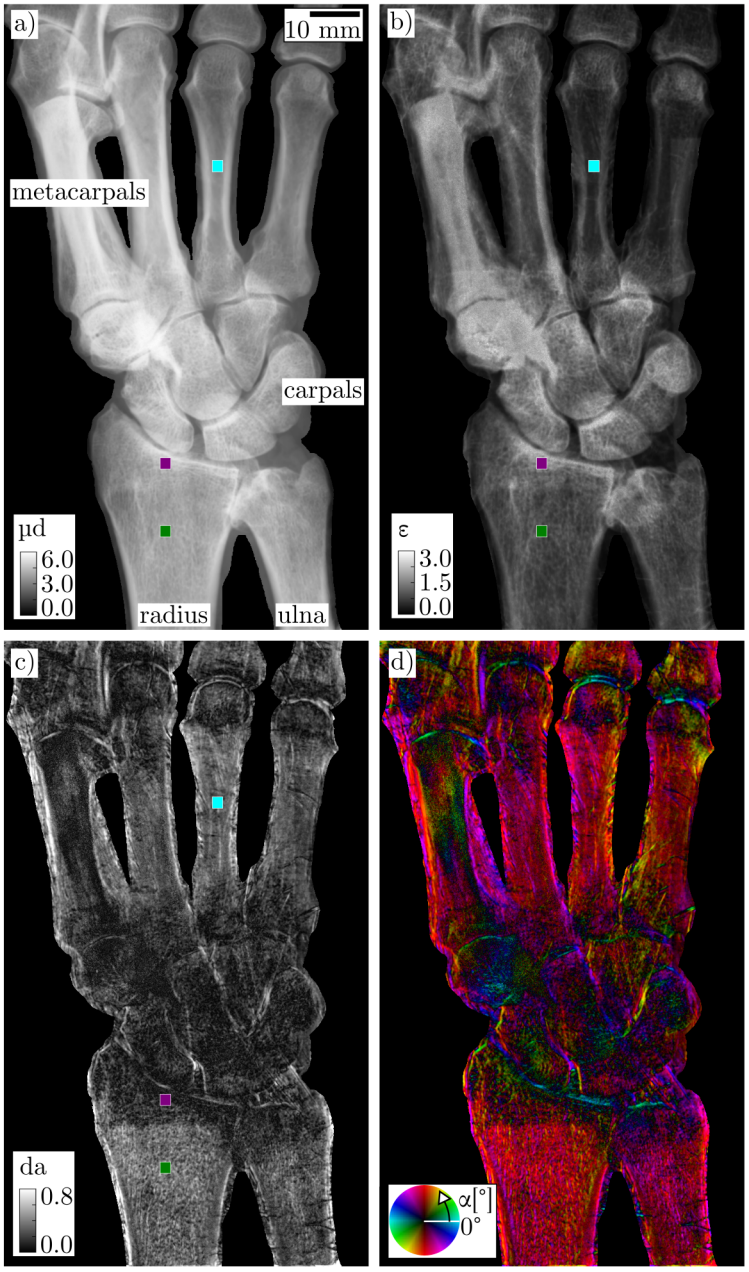

Figure 7.3: **X-ray vector radiography of a human hand.** The sample includes the radius, ulna, carpals and metacarpals. a) presents the integrated attenuation coefficient μd, the mean scattering strength is shown in b). c) illustrates the degree of anisotropy with mean values of $da_{\text{cyan}} = 0.26 \pm 0.04$, $da_{\text{purple}} = 0.09 \pm 0.05$ and $da_{\text{green}} = 0.39 \pm 0.11$ in the corresponding ROIs d) The orientation ϕ of scattering structures is depicted according to the color wheel with brightness encoding the degree of anisotropy. Quantitative values for all contrast modalities are given in Tab. 7.1.

signal correlate to the variations in the attenuation contrast and are therefore most likely due to density and thickness variations.

The XVR signal, on the other hand, shows a clear difference of the degree of anisotropy within the different parts of the long bones, corresponding to the microstructure of the bony anatomy. The osteons within the cortical bone are arranged in a linear order, lying parallel to each other and parallel to the long axis of the long bones [Standring, 2008]. In the diaphysis, the orientation of the trabecular bone is mainly lamellar as well, with a reduction of the total bone mass due to the spongious structure. Linear orientation of the osseous mineralized microstructure of cortical bone and trabecular bone of the diaphysis of long bones results in high anisotropy with a longitudinal internal orientation. In contrast, the trabecular bone within the epiphysis shows no linear but radial orientation of the bony microstructure. The growth process of the epiphysis follows a radial orientation of the cell columns, resulting in a radial orientation of the trabecular structure of the mature bone [Standring, 2008]. As a result, epiphyseal areas show a low degree of anisotropy with a divergent orientation of bony microstructures, explaining the different quantitative values observed in Fig. 7.2 and Fig. 7.3. The sharp transition between anisotropic scattering and the isotropic one consequently corresponds to the epiphyseal line which divides the diaphysis from the epiphysis. Short bones such as the carpalia do not have longitudinal orientation but consist of trabecular structure without any orientational preference. This results in a low degree of anisotropy, as can be seen in Fig. 7.3. The anisotropic signal oriented along the joint surface is mainly caused by the transition between the bone tissue and the liquid filling the joints. Such interfaces on a scale below the spatial resolution lead to a scattering signal in the orthogonal direction to the surface, and hence the detected orientation follows the joint surface.

Microfractures with a resulting discontinuity of the trabecula and included hematoma should result in a loss of the anisotropic scattering signal in XVR. Therefore, in acute trauma diagnostics, XVR may help to increase sensitivity in so-called radiographically occult fractures of the trabecular bones.

However, several limitations have to be addressed in order to clinically apply this technique. The energy of 25 keV should be increased in order to reduce beam starvation and dose. On the downside, higher energies require gratings with even higher aspect ratios if they effectively block high energies. In general, this leads to a lower setup visibility and hence sensitivity. The setup autocorrelation might also change towards higher values and hence be sensitive to different structure sizes. In addition, the number of phase steps required for one DFC-image should be reduced as well as the number of different sample orientations to a minimum of three points necessary to fit a sinusoidal curve of a known period. Another approach could be a so-called single shot technique, requiring that the fringes are directly resolved by the detector. It has been shown that

this technique can reveal DFC-images for *in vivo* objects with a dose comparable to conventional chest radiographs [Wen, 2010; Bennett, 2010; Kagias, 2016]. In contrast to conventional radiography, XVR detects subpixel-sized information. This could allow a reduction of spatial resolution and lead to a decreased dose level as well. Recently developed phase grating far-field interferometers could avoid absorption gratings and thus further reduce the dose [Wen, 2013; Miao, 2015; Miao, 2016]. For mammography applications, it has already been shown that a Talbot interferometer can get equal contrast in attenuation as a conventional setup at a comparable dose level [Scherer, 2015b] without even considering the additional contrast modalities. In order to reduce the measurement time, the field of view should be increased in order to fully cover a single hand within one acquisition. The MuCLS is a well-suited source for XVR since the quasi-monochromatic radiation mostly avoids beam-hardening artifacts and could allow to further reduce the dose with respect to a polychromatic setup [Thüring, 2013a]. However, XVR has been successfully applied in laboratory setups as well, showing the feasibility of clinical application [Baum, 2015; Eggl, 2015].

In conclusion, XVR provides a suitable tool for directly detecting the anisotropy and orientation of scattering structures. It is sensitive to the bone microstructure and thereby has the potential to improve the diagnostics of so-called radiographically occult fractures.

X-ray Vector Radiography Reveals Bone Microfractures 8

In this chapter, the detection of microfractures with x-ray vector radiography (XVR) is shown by measuring four bone samples. The results have been published previously in the following article, parts of the following text are adapted from this article:

Jud *et al.* [Jud, 2018b]

8.1 Motivation

Previous work has already shown the feasibility for in-vivo measurements of the extremities as well as an improved diagnostic value of the dark-field signal due to its correlation with bone microstructure [Tanaka, 2013; Schaff, 2015a; Eggl, 2015].

In chapter 7, a correlation between x-ray vector radiography (XVR) and bone structure changes was shown for a human cadaver hand, investigating the potential of XVR to detect microfractures without macroscopic displacement [Jud, 2017]. Our hypothesis is that XVR can detect radiographically occult fractures. However, the detection of radiographically occult fractures has not been shown explicitly. Here, we evaluate its potential using a porcine rib model and compare the additional contrast modalities to conventional radiography. The results are verified by comparison to high-resolution μCT-data and the benefits of a directional measurement are emphasized by comparison of different single scattering directions.

8.2 Materials and Methods

The hypothesis was tested using a porcine rib model with artificially induced plastic deformations. The Munich Compact Light Source (MuCLS) provided a simplified experimental setup with quasi-monochromatic and coherent X-rays. The XVR provided various contrast modalities including conventional attenuation which are compared with each other and with ground-truth data obtained using a high-resolution μCT.

A total number of four porcine loin ribs were measured, a photograph of a single rib can be found in Fig. 8.1 a). After they had been freshly purchased at a local store, the bone was separated from the soft tissue. To damage the ribs, both ends were inserted into

a metal pipe. With the resulting leverage, a controlled bending against the curvature of the ribs could be carried out until a plastic deformation was suspected. However, a complete fracture of the ribs was carefully avoided. After the bending force has been removed, the specimens elastically returned to their original overall shape. An upper bound of the applied torque was estimated by completely fracturing three reference ribs. For these samples, a maximum torque of 12 Nm led to a complete bone fracture.

The measurement was performed at the Munich Compact Light Source, described in more detail in section 3.4.1. For this experiment, the energy was tuned to 25.0 keV, the total flux was $\Phi_{tot} = 1.3 \cdot 10^{10}$ photons/s with a Gaussian root mean square source diameter of about 50 µm. The Talbot grating-interferometer described in chapter 4, was used to generate dark-field contrast (DFC) and differential phase-contrast (DPC) in addition to the attenuation. X-rays were detected using a Dexela 1512 detector with a gadolinium oxysulfide scintillator and a pixel pitch of 74.8 µm. A Gaussian point spread function with a root mean square width of about 1 pixel and a geometric magnification of 1.075 yielded a half-period resolution of approximately 70 µm. For each rotation, attenuation, DFC and DPC were acquired using 7 phase-steps with an exposure time of 2.4 s per step.

For the XVR, 16 DFC-images with different sample orientations around the optical axis and hence sensitivity directions of $\psi = \{0°, 12°, 24°, \ldots, 168°, 180°\}$ were acquired. As described in chapter 5, the DFC-images were registered to one another and the scattering strength calculated as the negative logarithm of the DFC [Revol, 2012; Malecki, 2013].

The μCT was performed with a commercial setup (GE phoenix|X-ray v|tome|x,General Electric, USA). A direct tube with an acceleration voltage of 60 kV and a source power of 15 W was used to generate x-rays. A total number of 1601 projections were recorded with an exposure time of 333 ms each, the reconstruction had a voxel size of 20 µm^3.

8.2.1 Dose Calculation

The kinetic energy released per unit mass in air (air-KERMA) was calculated to provide a measure for the applied dose in the experiment. As the name indicates, KERMA is defined as the sum of the kinetic energy transmitted by ionizing radiation to charged secondary particles per mass [Bille, 2002]:

$$K = \frac{\mathrm{d}\bar{E}_{tr}}{\mathrm{d}m} = \int E\,\Phi(E)\frac{\mu_{tr}(E)}{\rho}\,\mathrm{d}E\,, \tag{8.1}$$

where μ_{tr}/ρ is the mass energy-transfer coefficient and $\Phi(E)$ is the spectral flux. Conventionally, the KERMA in air K_{air} is used to get a measure for dose independent of

the used sample, which leads to

$$K_{air} = \int E\,\Phi(E)\left(\frac{\mu_{tr}(E)}{\rho}\right)_{air} \mathrm{d}E\,. \tag{8.2}$$

On the right-hand side of the Eq. (8.2), the mass energy-transfer value can be extracted from tabulated data [Buhr, 2012]. Hence, we only need to determine the spectral flux $\Phi(E)$ in order to calculate the air-KERMA. The spectrum $S_{exp}(E)$ was detected with the spectral detector KETEK AXAS-D (KETEK GmbH, Munich, Germany). The detector has a silicon sensor with a thickness $d_{si} = 450\,\mu\mathrm{m}$. Attenuation values were taken from the Python package xraylib [Schoonjans, 2011], based on the XCOM database [Berger, 2010]. With the tabulated attenuation coefficient for photo-effect $\mu_{si,pe}(E)$, we calculate the detector efficiency

$$\eta_k(E) = 1 - \exp(-\mu_{si,pe}(E)\,\rho_{si}\,d_{si})\,, \tag{8.3}$$

where $\rho_{si} = 2.335\,\mathrm{g/cm^3}$ is the density of silicon. The spectrum was filtered with a thickness $d_{al} = 1.395\,\mathrm{cm}$ of aluminum and $\rho_{al} = 2.72\,\mathrm{g/cm^3}$, leading to a transmission of

$$T_{al}(E) = \exp(-\mu_{al}(E)\,\rho_{al}\,d_{al})\,, \tag{8.4}$$

where $\mu_{al}(E)$ again corresponds to tabulated data. Similarly, the transmission in air is given by

$$T_{s,k}(E) = \exp(-\mu_{air}(E)\,\rho_{air}\,d_{s,k})\,, \tag{8.5}$$

where $d_{s,k}$ is the distance between source and KETEK-detector. Putting everything together, we can calculate the normalized source spectrum

$$S_0 = \frac{1}{C}\frac{S_{exp}}{\eta_k\,T_{al}\,T_{s,k}}\,, \tag{8.6}$$

where the constant C is chosen such

$$\int S_0(E)\mathrm{d}E = 1\,. \tag{8.7}$$

To get the source spectrum, $S_0(E)$ is multiplied with the total flux Φ_0, which is experimentally determined. Analog to Eq. (8.2.1), we calculate the transmission $T_{s,sam}$ from the source to the sample at distance $d_{s,sam}$. Hence, we get the flux density from

$$\Phi(E) = \Phi_0\,\frac{S_0(E)\,T_{s,sam}}{A}\,, \tag{8.8}$$

where A is the beam size at the sample position. Finally, we can use Eq. (8.2) to calculate the air-KERMA. Taking into account flux variations for different samples, this yields between $(0.26 \pm 0.03)\,\mathrm{mGy/s}$ and $(0.21 \pm 0.03)\,\mathrm{mGy/s}$ and hence between $(70 \pm 8)\,\mathrm{mGy}$ and $(56 \pm 8)\,\mathrm{mGy}$ with the total measurement time of 268.8 s.

8.3 Results

8.3.1 Full XVR Imaging Information

Four porcine loin ribs labeled R1-R4 were measured in our study. Figure 8.1 depicts the full information gained from an XVR for sample R1. In Fig. 8.1 a), a photograph shows the sample when mounted in the experimental setup. The location of the bone fracture is indicated by a black mark, the horizontal bars of the sample holder on top and bottom approximately indicate the field of view. Figure 8.1 b) presents the integrated attenuation image, its value is relatively constant for the whole bone region with a mean value of $\mu d = 1.44 \pm 0.27$ for the orange region-of-interest (ROI). The spatial resolution of approximately 70 µm allows seeing the trabecular bone structure, which is predominantly aligned in the vertical direction.

The sample scattering properties, i.e. mean scattering strength, degree of anisotropy and direction of scattering structures, are depicted in Fig. 8.1 c)-e). In Fig. 8.1 c), the mean scattering strength allows to easily distinguish the damaged sample region from the rest. Quantitatively, the undamaged sample within the green ROI has a mean scattering strength of $\epsilon_{ref} = 0.26 \pm 0.07$, while the damaged bone region has about twice the scattering strength with a mean value of $\epsilon_{dmg} = 0.81 \pm 0.17$ in the blue ROI. Figure 8.1 d) depicts the scattering degree of anisotropy (da), defined as the difference of maximal to minimal scattering strength divided by its mean. A value of one hence indicates a scattering distribution with a maximum in one direction and no scattering orthogonal to it while a value of zero corresponds to isotropic scattering. The degree of anisotropy is very homogeneous, with a mean value of $da = 0.54 \pm 0.08$ within the orange ROI (cf. Fig. 8.1 b). The mean structure orientation, corresponding to the direction of least scattering, is color-coded in Fig. 8.1 e) according to the color wheel on the bottom right, the brightness corresponds to the degree of anisotropy. The sample structure is predominantly aligned in the vertical direction with a mean orientation of $\alpha = 86^\circ \pm 5^\circ$ in the orange ROI, corresponding to a red color. The DPC in Fig. 8.1 f) shows the differential phase-contrast. In this contrast modality, the damaged sample region shows a modified signal as well.

8.3.2 Mean Scattering Strength

For the samples R2-R4, the mean attenuation and the scattering strength are depicted in Fig. 8.2. Similarly to sample R1, the integrated attenuation coefficient is once again quite homogeneous over the whole bone region. However, the mean scattering strength in the damaged bone region exceeds the scattering strength within the undamaged bone. The corresponding quantitative values are summarized in Tab. 8.1. The signal

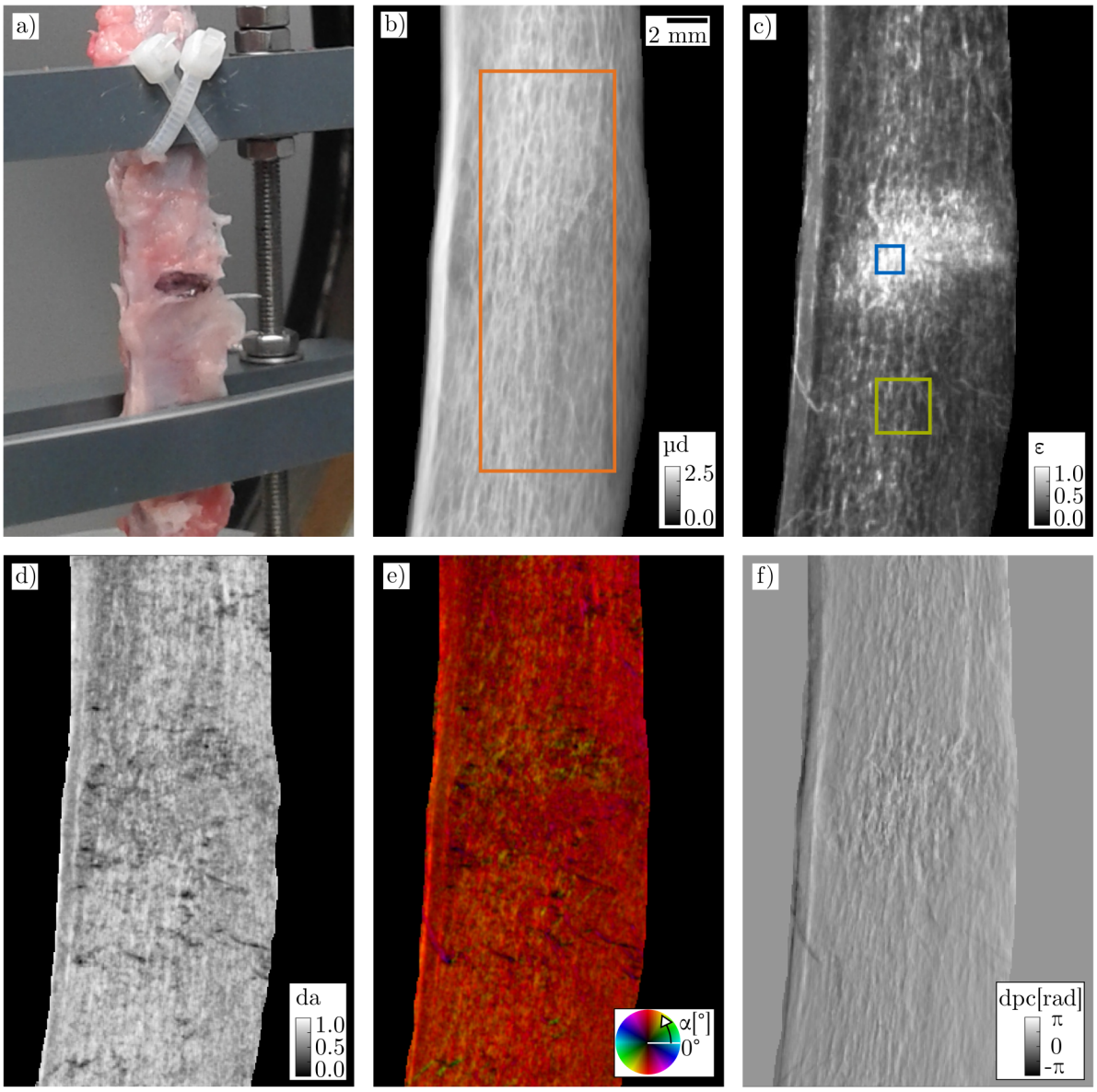

Figure 8.1: **XVR of porcine rib (sample R1).** a) Photograph of the sample. The sample holder approximately indicates the field of view, the damaged bone region is indicated by a black mark. b) Integrated attenuation coefficient, a scale bar of 2 mm length indicates the sample size. c) Mean scattering strength ϵ, defined as the negative logarithm of the dark-field signal averaged over different orientations. d) Degree of anisotropy, i.e. the difference between maximal and minimal scattering divided by its mean. e) Orientation of scattering structures are color-coded according to the color wheel, brightness corresponds to the degree of anisotropy. f) Differential phase-contrast image showing the angle of refraction. The colored ROIs indicate the area used to calculate the mean values shown in Tab. 8.1.

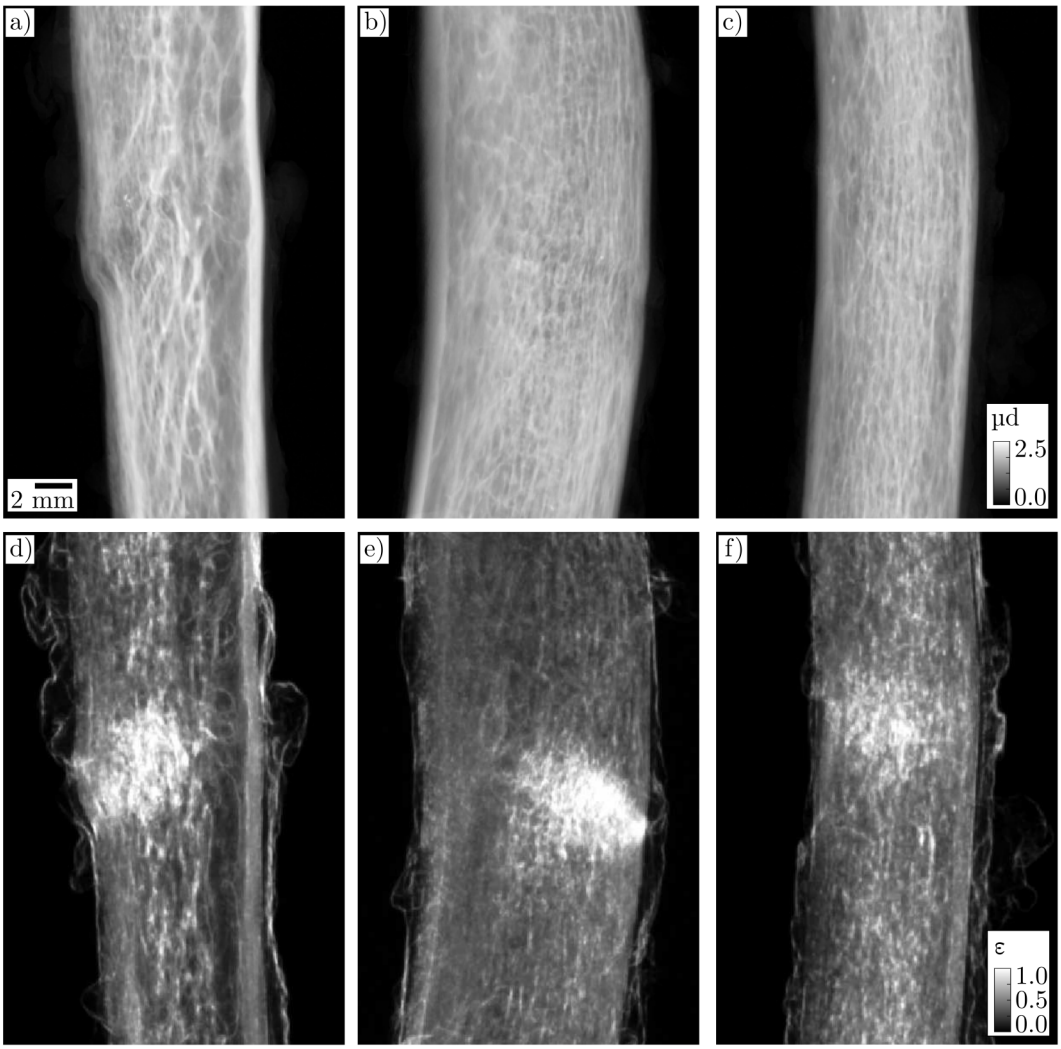

Figure 8.2: **Attenuation and mean scattering strength for samples R2-R4.** The first row (a-c) depicts the integrated attenuation coefficient, the second row (d-f) the mean scattering strength. A scale bar of 2 mm length indicates the sample size.

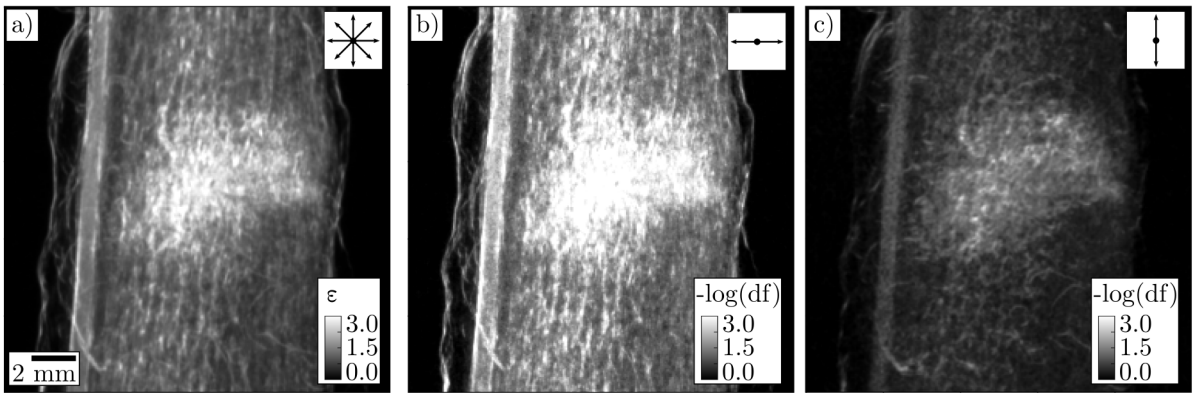

Figure 8.3: **Mean scattering strength vs. dark-field for sample R1.** a) Illustrates the mean scattering strength averaged over different sensitivity directions. Part b) shows horizontal scattering sensitivity (i.e. vertical grating orientation) and c) vertical scattering sensitivity.

in the damaged bone region is thereby increased by an average factor of 2.6 with respect to an undamaged reference ROI. To get a more quantitative measure for the image quality, the contrast between both ROIs is compared to the variance in the undamaged bone region. This yields an average feature visibility of 7.9 in the mean scattering strength images and 0.6 in the attenuation images, using similar ROIs as for the mean scattering strength. The ratio of the contrast to the background noise level has an average value of 350 for the mean scattering images.

In Fig. 8.3, the mean scattering strength (a) is compared to single DFC images that are mainly sensitive to the horizontal scattering direction (b) and the vertical scattering direction (c). The image sensitive to horizontal scattering has the strongest signal and primarily detects vertical structures. Analogously, the image sensitive to vertical scattering detects horizontal sample structures and yields the weakest signal.

8.3.3 Micro Computed Tomography

To prove the microstructural sample changes, all samples were measured using state-of-the-art μCT. Fig. 8.4 shows a vertical and a horizontal slice; their approximate position is indicated in Fig. 8.4 a), which again shows the mean scattering strength of sample R1. Three main phases corresponding to trabecular bone structure, soft tissue, and air can be identified as indicated by respective orange, blue and gray triangles. The vertical slice shows an abnormal deformation of the trabecular structure on the front side, as indicated by a blue arrow. The location corresponds to the point of force application. In the horizontal slice, small cracks in the cortical bone are visible,

Sample	μd	da	ϵ_{dmg}	ϵ_{ref}	ϵ_{bg}	α [°]
R1	1.44	0.54	0.82	0.26	0.0064	86
	±0.27	±0.08	±0.17	±0.07	±0.0011	±5
R2	1.49	0.50	0.82	0.35	0.0023	92
	±0.17	±0.10	±0.15	±0.09	±0.0012	92 ± 7
R3	1.46	0.47	0.89	0.28	0.0047	82
	±0.11	±0.09	±0.12	±0.04	±0.0015	82 ± 5
R4	1.47	0.63	0.65	0.41	−0.0110	87
	±0.17	±0.08	±0.14	±0.09	±0.0026	87 ± 3

Table 8.1: **Quantitative values for samples R1-R4.** A large ROI similar to the orange one shown in Fig. 8.1 B was used to calculate the integrated attenuation coefficient μd as well as the degree of anisotropy (da) and the orientation of scattering structures α. Smaller ROIs such as the blue and green one in Fig. 8.1 c) were used for the mean scattering in the damaged bone region ϵ_{dmg} and the undamaged region ϵ_{ref}, respectively. A ROI ϵ_{bg} outside the sample region (not shown) was used to determine the background noise level. The values represent the mean of a Gaussian fit to the histogram of the respective ROIs, the uncertainty corresponds to the standard deviation.

as indicated by green arrows. On the opposite side, the trabecular structure is not strongly affected.

8.4 Discussion

The samples were damaged by bending using two metal pipes. The bending moment was opposed to the rib curvature, causing a compression on the front side and strain on the back side. As can be seen in the μCT results (cf. Fig. 8.4), this dislocated the trabecular structure on the front side and introduced small cracks.

Changes in the trabecular microstructure, however, did not change the bones' overall composition. In particular, the trabecular structures were dislocated mostly in the beam direction, leading to an unchanged projected density and a minor change in attenuation. In contrast, the distribution of soft tissue changed, due to its low average atomic number and density the effect on the attenuation remains minimal. In total, this leads to very little contrast in the attenuation signal, which can be seen in Fig. 8.1 and Fig. 8.2.

Small-angle x-ray scattering and thus the dark-field images are sensitive to gradients

Sample	Air-Kerma [mGy/s]	Feature vis. int. att.	Feature vis. mean scattering	Contrast to bg. noise
R1	0.26 ± 0.03	0.55	8.0	509
R2	0.22 ± 0.03	0.57	5.9	392
R3	0.22 ± 0.03	1.00	15.3	407
R4	0.21 ± 0.03	0.18	2.7	92

Table 8.2: **Derived values for samples R1-R4.** The first column shows the air-kerma as derived in section 8.2.1. The feature visibility is defined as the signal difference in between two ROIs, divided by the signal variance in the undamaged reference ROI. For the mean scattering strength, this leads to $(\epsilon_{dmg} - \epsilon_{ref})/\sigma_{ref}$. Analogously, the feature visibility for the integrated attenuation coefficient is calculated. In the last column depicts the contrast between the mean scattering strength normalized to the background noise level, i.e., $(\epsilon_{dmg} - \epsilon_{ref})/\sigma_{bg}$.

in electron density and thus sample morphology. Small cracks and air-filled voids both induced such interfaces and let to an increased scattering strength. In all samples, the mean scattering strength in the undamaged bone region had a comparable value of about $\epsilon = 0.26 - 0.41$. Hence, the average morphological structure is comparable for different samples and the scattering value can be used for comparison. With respect to this reference value, the signal increases roughly by a factor of 2.6 in the damaged bone region, resulting in a good contrast as can be seen in Fig. 8.1 c) and Fig. 8.2. This can be seen as well by comparing the contrast to the average variance in the bones, which is dominated by the signal variance due to the trabecular structure. This so-called feature visibility is > 1 for the mean scattering signal, indicating a good detectability of the broken bone region. In contrast to the mean scattering signal, the difference of the attenuation values is smaller than the signal variance, reflecting the observation that the damaged bone region cannot be identified in this contrast modality.

The structure orientation in Fig. 8.1, however, is not affected by the sample damage, which indicates an unchanged trabecular structure in the vertical direction (see also Fig. 8.3). That is reasonable since the displacement of the trabecular structure in projection direction has only a minor effect on the structure along the sample's main axis.

This could explain as well that the degree of anisotropy is homogeneous throughout the sample with values of $da = 0.47 - 0.63$. As illustrated in Fig. 8.5, this is considerably higher than for isotropic human bone samples such as femoral heads ($da = 0.07 - 0.32$) [Schaff, 2015a], human vertebra ($da = 0.12 - 0.17$) [Eggl, 2015] and the epiphysis in

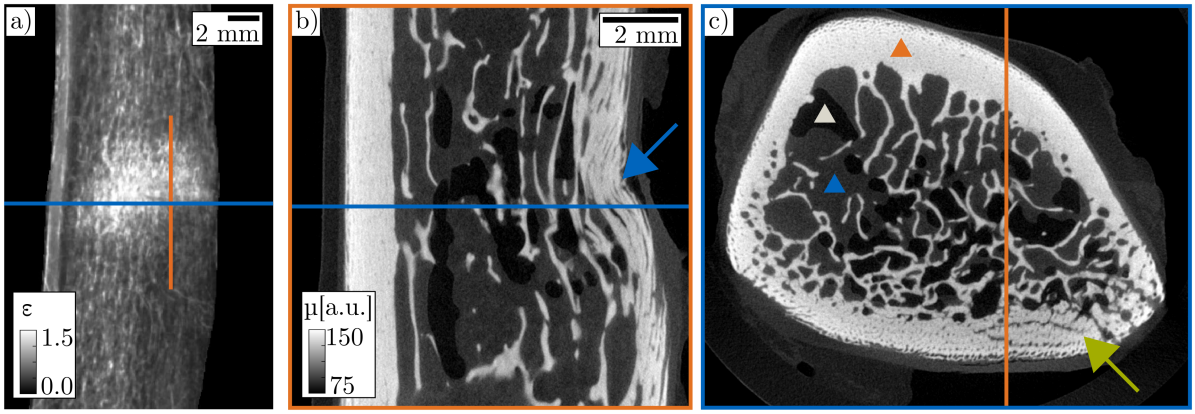

Figure 8.4: μCT **images of sample R1.** a) Mean scattering strength with two lines indicating the approximate position of the μCT slices. b) depicts a vertical slice and c) a horizontal one. The cortical bone and trabecular structure are indicated by an orange triangle. The blue triangle indicates soft tissue; the gray triangle indicates air inclusions. The trabecular structure is deformed and compressed in beam direction, as indicated by the blue arrow. Some small cracks have been induced as indicated by the green arrow.

metacarpal bones ($da = 0.09$) [Jud, 2017]. Even more anisotropic bones such as the diaphysis of metacarpal bones ($da = 0.25 - 0.26$) or the radius ($da = 0.39$) have lower anisotropy values. This observation can be explained by the higher anisotropy of rib structures compared to other bones. The high anisotropy value emphasizes the need for a directional measurement which can be seen in Fig. 8.3, where the signal for horizontal scattering is much stronger than for vertical scattering. In the extreme case of a completely anisotropic sample, choosing the wrong scattering direction would lead to no signal at all. If, however, the sample orientation is known a priori, one could measure only in the direction of highest scattering without doing a full XVR. On the one hand, this would be beneficial in terms of dose, measurement time and setup complexity. On the other hand, structures scattering orthogonally to the main scattering orientation would be missed entirely, potentially leading to a wrong or incomplete image interpretation. In addition, information contained in the anisotropy or structure orientation would not be available as a potential source of information.

Another quantity is probed by the differential phase-contrast image in Fig. 8.1 f) (cf. chapter 4). Although the damaged bone region can be vaguely identified, the contrast is much lower than for the mean scattering strength.

One of the limitations of XVR is the increased dose level compared to state of the art techniques. As already discussed in chapter 7, the energy should be increased from the 25 keV used in this study to values of $60 - 75$ kVp currently used for bone imaging.

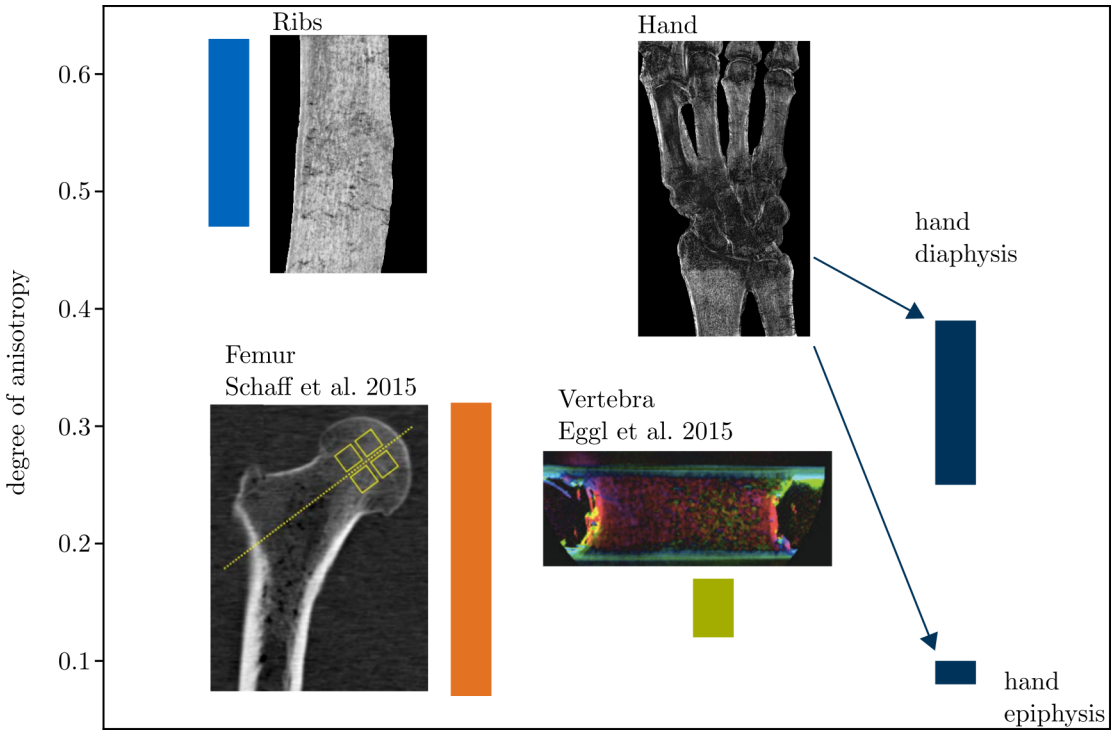

Figure 8.5: **Comparison of different degree of anisotropy values in literature.** To the left, ribs are depicted with a very high degree of anisotropy of $da = 0.47 - 0.63$. This reflects their anisotropic structure, which is even more pronounced than the diaphysis in human hands with $da = 0.25 - 0.39$. Isotropic structures such as human femur ($da = 0.07 - 0.32$) or human vertebral bones ($da = 0.12 - 0.17$) have a lower degree of anisotropy, comparable to the epiphysis in the human hand ($da = 0.09$) [Schaff, 2015a; Eggl, 2015].

Challenges when increasing the energy are that increased energies require gratings with even higher aspect ratios if they effectively block high energies. In general, this leads to a lower setup visibility and hence sensitivity, and the setup autocorrelation might also change towards higher values and therefore be sensitive to different structure sizes. Advantages of an increased energy are the decreased dose and reduced beam-hardening. Additionally, the number of projections needed for an XVR should be minimized. A single phase-contrast image and the directional information are mathematically both extracted respectively from a fit of a sinusoidal curve of a known period. For such a fit, a minimum of 3 points would be sufficient, corresponding to a minimum number of 9 single images required for an XVR. For phase-contrast imaging, so-called single-shot techniques could even extract all information from a single image and further decrease

this number [Wen, 2010; Diemoz, 2017]. The contrast between the broken and unbroken bone region is increased by an average factor of 350 with respect to the background noise level (see Tab. 8.2). This high value indicates a possible reduction of the total exposure time without losing the diagnostic image relevance. Moreover, phase-contrast imaging with clinically compatible doses has been demonstrated for mammography applications and lung imaging [Scherer, 2015b; Gromann, 2017; Olivo, 2013; Willer, 2018]. In contrast to conventional radiography, XVR does not rely on directly resolving the examined structures since its signal is caused by subpixel sized structures. Hence, the resolution and thus the required dose could be lowered with respect to conventional setups. In addition, quasi-monochromatic x-ray sources like the MuCLS can provide the same image quality at a lower dose level [Thüring, 2013a]. The superposition of different signals due to the projection geometry might conceal information because certain soft-tissue types such as the lung cause a strong scattering signal. In particular, this might be a challenge for spine imaging. However, certain imaging tasks such as radiographs of the extremities are not much affected by soft tissue, it has already been shown that human hands can be imaged with XVR. Moreover, foreign bodies such as glass or wood have been investigated using X-ray scattering, which could be combined with XVR to obtain additional information in the case of open fractures [Braig, 2018].

In conclusion, our study demonstrates the increased diagnostic value of XVR for bone fracture detection.

Anisotropic X-ray Dark-Field Tomography Reveals Tooth Cracks

9

In this chapter, an advanced method for the detection of tooth cracks is presented. The results have been published previously in the following article, parts of the following text are adapted from this article:

Jud *et al.* [Jud, 2018a]

9.1 Motivation

Cracked tooth syndrome (CTS) affects about 5% of all adults each year and is one of the most common clinical findings for teeth [Bader, 2008]. In about 15% of all cases, the crack either affects the pulp or leads to tooth extraction [Bader, 1996]. CTS is most common in mandibular molars [Cameron, 1964; Jun, 2016], whereas about 65% of all cracks are found in teeth with restorations [Hiatt, 1973], since the amount of supporting tooth structure is reduced and may no longer withstand masticatory forces [Talim, 1974; Cameron, 1976; Eakle, 1986]. However, tooth crowns are used to prevent cracks as well, which was found by a study in North Carolina [Bader, 1996]. Apart from iatrogenic causes such as restorations, natural risk factors include bruxism, occlusion habits, extensive attrition and abrasion [Geurtsen, 1999; Lynch, 2002]. Older patients over 40 years are more affected by CTS, making it a problematic side-effect of a growing average lifespan [Cameron, 1964; Cameron, 1976; Eakle, 1986; Roh, 2006].

The symptoms can include pain, bite problems and sensitivity to bitterness or heat. It is not ideal to use them as the sole source of information since they are not uniquely identified with CTS. Despite the vast number of cases, however, there is still no standard procedure for an evidence-based diagnostic tool to confirm CTS. A standard diagnostic procedure is a visual inspection. Although this technique is limited by the resolution of human eyes of about 200 µm [Alberts, 2014], microscopic examination and contrast enhancers such as methylene blue dye can overcome this challenge. In the transillumination method, a fiber optic is used to illuminate the tooth. If some crack extends to the dentin, the light gets distorted which can be inspected using a magnifying optic [Cameron, 1976; AbouRass, 1983; Slaton, 2003]. To reproduce the symptoms, percussions, thermal pulp tests or bite-tests can be performed, whereas pain upon release is an indicator for cracks [Lynch, 2002]. Other alternatives for the diagnosis of CTS are

ultrasound testing [Culjat, 2005], infrared thermography [MatsushitaTokugawa, 2013], or optical coherence tomographic imaging [Imai, 2012]. X-ray radiography is routinely used to diagnose the pulp health and the gums but rarely detects cracks [AbouRass, 1983]. Cone-beam computed tomography provides additional 3D-information but has a limited spatial resolution [Kalyan Chakravarthy, 2012]. Even high-resolution micro-CTs can typically identify cracks only if they are larger than 80 µm [Tanimoto, 2009]. However, the early detection of microcracks is crucial to prevent secondary infections and further crack propagation [Hiatt, 1973].

Analog to x-ray vector radiography (XVR, see chapter 5), x-ray dark-field tomography (XDT) exploits the directional dependent dark-field signal. However, it is not restricted to projection geometry but reconstructs scattering tensors in three dimensions. This is possible by measuring a large number of different sample orientations and thus sensitivity directions. An optimized way to cover a maximum of different sensitivity directions was investigated by [Sharma, 2017]. A first reconstruction was presented by [Malecki, 2014] and further developed by [Wieczorek, 2016]. It has been shown that the signal correlates well with the orientation of fibrous structures and can be used to detect the orientation of dentinal tubules [Jud, 2016].

In this chapter, we evaluate XDT as a tool for the detection of tooth microcracks. The complementary information provided by x-ray scattering is investigated and compared to the simultaneously acquired attenuation signal we demonstrate that we can indirectly detect microstructure features for a whole tooth in a non-destructive measurement.

9.2 Materials and Methods

The measured samples were three human teeth which have been extracted in a clinic for maxillofacial surgery in Munich. After extraction, the samples have been conserved in a buffer solution.

9.2.1 Sample Fixation

To conserve the samples, they were embedded in an araldite epoxy resin. Hence, the specimens were gradually dehydrated to a 100% acetone solution. The used concentrations (all vol/vol) for the dehydration series were in %: 30, 50, 70, 80, 90, 95 and 100 acetone balanced with distilled water. The dehydration incubations were performed for 1 hour each. Subsequently, the sample was embedded in Araldite A, i.e. a mixture of Araldite M and Hardener in a weight ratio of 1:1. This process was repeated in a ratio of Araldite A and Acetone of 1:3 for 1 hour, 1:1 for 4 hours, 3:1 for 2 hours and

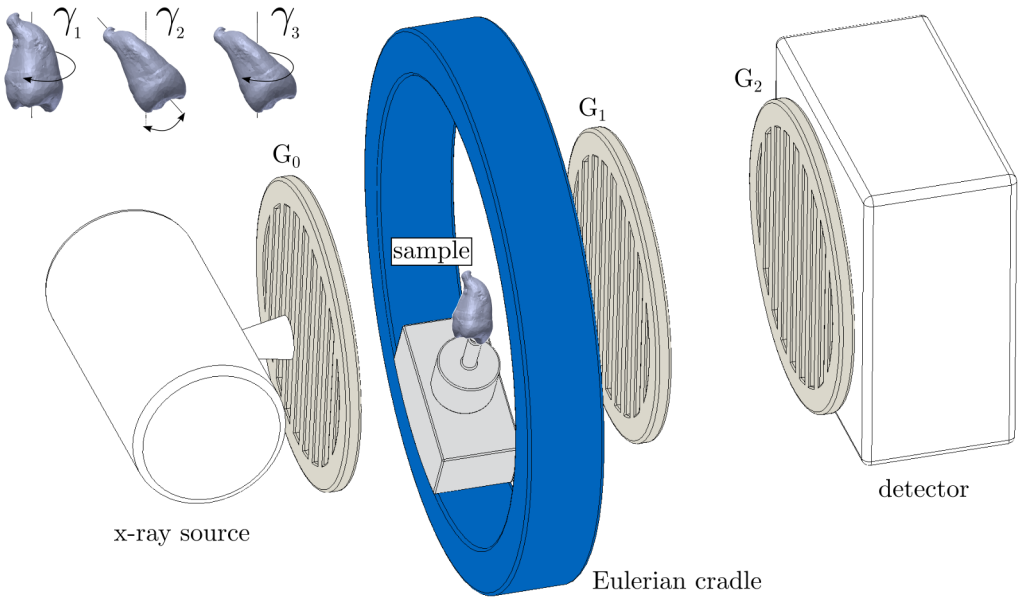

Figure 9.1: **Schematic overview of the experimental setup.** A microfocus x-ray source generates a polychromatic spectrum which is recorded by a flat-panel detector. Source grating G_0 provides enough spatial coherence to generate a self-interference effect after phase-grating G_1. The subsequent modulation is recorded by a phase-stepping procedure with attenuation grating G_2 and yields the attenuation, differential phase and dark-field image.

100% Araldite A overnight. Finally, the samples were embedded in Araldite B (10 g Araldite M, 10 g Hardener and 0.6 g Accelerator) and heated at 60° C for two days.

9.2.2 Setup Parameter

The experimental setup illustrated in Fig.9.1 consisted of a microfocus x-ray tube (X-ray WorX XWT-160-SE) and a flat panel detector (Varian 2520DX) with a pixel pitch of 127 μm. The tube voltage was 60 kV with a power of 20 W. A Talbot-Lau grating interferometer with a design energy of 45 keV allowed to measure dark-field images in addition to the conventional attenuation. As sketched in Fig. 9.1, the interferometer consists of two attenuation gratings (G_0 and G_2) with periods of 10 µm and a phase-shifting grating (G_1) with a period of 5 µm. The phase-grating consisted of Ni with a height of 8 µm which phase-shifts x-rays at the design energy by a factor of $\pi/2$. The gratings were symmetrically adjusted with an inter-grating distance of 92.7 cm, more details about the grating interferometer can be found in [Prade, 2015]. A single

dark-field image was measured with a phase-stepping procedure consisting of 5 separate acquisitions at different positions of phase-grating G_1 with an exposure time of 5 s each [Weitkamp, 2006].

9.2.3 X-ray Dark-Field Tomography

The sample was mounted in an Eulerian cradle which allowed almost free sample rotation in space according to the Eulerian angles γ_1, γ_2 and γ_3 as depicted in Fig. 9.1. To cover a large range of sensitivity directions, 1025 sample projections were measured in total. Their orientations were distributed according to an optimized acquisition scheme which covers a maximum of different scattering directions in the dark-field contrast modality [Sharma, 2017]. The anisotropic XDT was then reconstructed according to an algorithm provided by [Wieczorek, 2016]. From the reconstruction results, we used the mean scattering signal as well as the attenuation for our analysis.

9.3 Results

The first sample was an upper left third molar tooth of an adult male. In Fig. 9.2, slices through both the attenuation reconstruction (a-c) and the mean scattering (d-e) are shown. Both contrast modalities are simultaneously reconstructed from identical raw data, and hence perfectly registered to each other. The slice positions are indicated by colored lines, the data was windowed for maximal contrast. In the attenuation image, the main tooth regions such as enamel, dentin and pulp chamber can be easily distinguished. Cracks are visible in the axial slices, their position is indicated by white arrows. In contrast to the attenuation, there is little contrast between enamel and dentin in the mean scattering image, the pulp chamber has been masked using the attenuation data. However, the cracks already visible in the attenuation image are now the most prominent image feature. Moreover, additional cracks are indicated by green arrows. To get a quantitative comparison between both contrast modalities, two line-plots L1 and L2 are presented in f) and g), their position is indicated in the corresponding axial slices. The attenuation shown in blue is quite homogeneous, only a small intensity loss indicates the crack positions. In the mean scattering, however, crack positions can be easily identified. Quantitatively, we recall the visibility V, which is defined as

$$V = \frac{I_{\max} - I_{\min}}{I_{\max} + I_{\min}}\,, \tag{9.1}$$

where $I_{\max}$ and $I_{\min}$ correspond to the maximal and minimal intensity along the line-plot. With this definition, a peak with a low background level of zero leads to high visibility approaching 100 % whereas a homogeneous intensity distribution yields a low

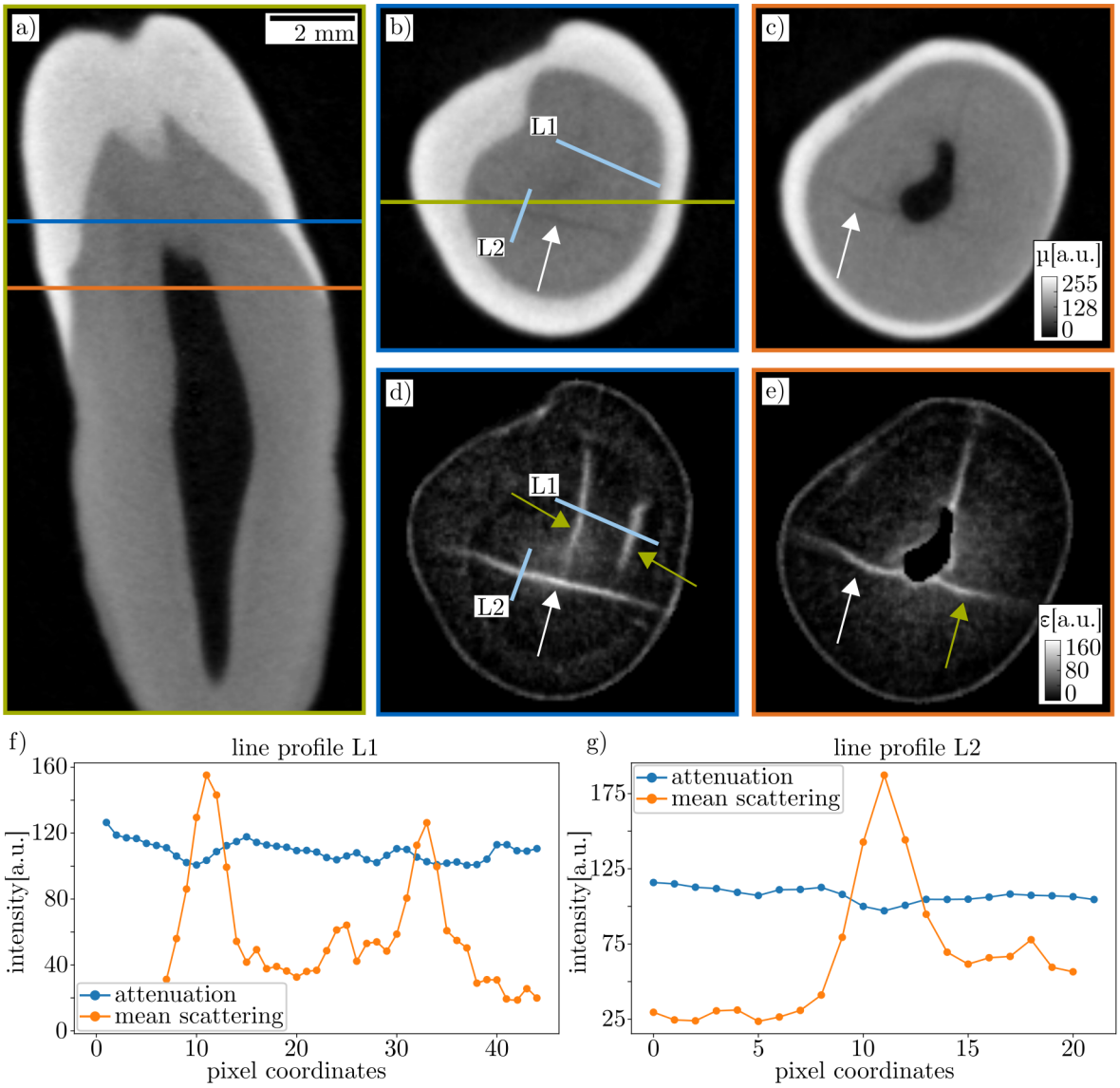

Figure 9.2: **Attenuation and mean scattering for a healthy tooth.** In a), a sagittal slice through the reconstruction depicts enamel, dentin and pulp, which are also visible in the axial slices in b) and c). The dentin region is homogeneous, a crack is indicated by a white arrow. The corresponding scattering signal is illustrated in d) and e) and shows the same crack (white arrow) as well as additional ones indicated by green arrows. Two line-plots L1 and L2 highlight the difference between both contrast modalities. The slice positions are indicated by colored lines, a scale bar indicates the approximate sample size.

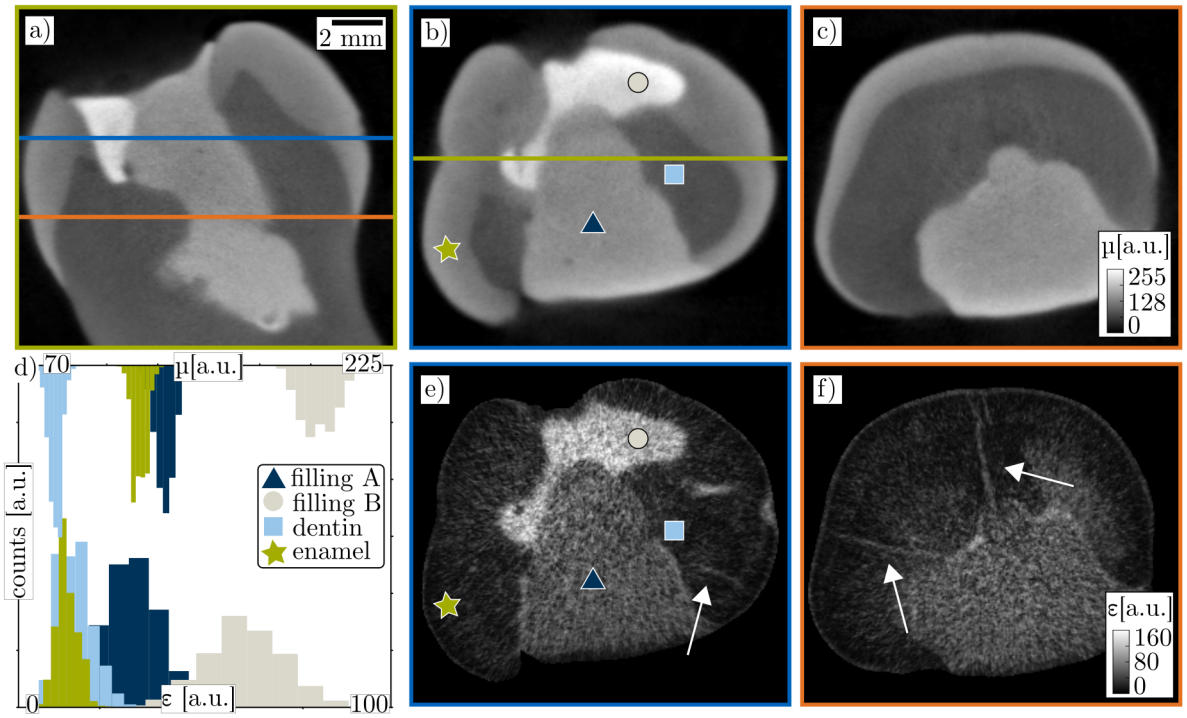

Figure 9.3: **Attenuation and mean scattering for a tooth with fillings.** A sagittal slice a) and two axial slices b-c) illustrate the attenuation signal. In d), histograms illustrate the attenuation and mean scattering strength for different tooth regions. The composite material filling and the glass ionomer cement (GIC) are depicted as well. In e-f), the mean scattering signal corresponding to the attenuation slices is shown. Some cracks are visible in this contrast modality and are oblique in the attenuation signal, as indicated by white arrows.

visibility. The line-plot L1 yields a low visibility of 11 % for the attenuation compared to 93 % for the scattering signal. For line-plot L2, the attenuation has a visibility of 9 % and the scattering a visibility of 78 %.

Figure 9.3 illustrates the results obtained with the second sample, an upper first molar, with two different fillings which are visible in the attenuation slices a-c) as bright regions. One consists of composite material as marked by a blue circle, it covers a part of the tooth crown. The other filling is composed of glass ionomer cement (GIC) as marked by a dark-blue square, it extends all the way to the tooth root. Quantitatively, Gaussian fit curves to the histograms shown in Fig. 9.3 d) yield the mean values and standard deviation for different tooth regions, the values are given in Tab. 9.1. The composite material filling attenuates most with a mean value of $\mu = 204 \pm 9$, GIC

Tooth Region	Attenuation [a.u.]	Mean Scattering [a.u.]
composite Material	204 ± 9	63 ± 12
Glass Ionomer Cement	129 ± 5	29 ± 8
Dentin	95 ± 3	12 ± 5
Enamel	116 ± 4	10 ± 3

Table 9.1: **Attenuation and scattering strength for different tooth regions.** The values are calculated from a Gaussian fit to a region of interest in the respective tooth region.

has a lower attenuation value of $\mu = 129 \pm 5$, which is close to the value of enamel ($\mu = 116 \pm 4$). In contrast to the attenuation, their mean scattering values are quite different: GIC has a mean scattering strength of $\epsilon = 29 \pm 8$, whereas enamel has $\epsilon = 10 \pm 3$. However, the mean scattering strengths for enamel and dentin are very close, which results in overlapping histograms for those tooth regions. In Fig 9.3 e) and f), three cracks are indicated by white arrows. They spread radially from GIC towards the surface. The third sample was a second premolar and is depicted in Fig. 9.4. It had a carious infection, which caused a smooth surface cavity, as can be seen in the attenuation slices in Fig. 9.4 a-c), their positions are again indicated by colored lines. The disease already penetrated the dentin region but did not spread to the pulp yet. In the second row (Fig. 9.4 d-f), the corresponding mean scattering slices detect the cavity and the affected dentin region as well. A decrease in scattering can be seen close to the enamel-dentin border, allowing them to be distinguished in the mean scattering signal. Additionally, a crack is visible extending from the enamel to the diseased tooth region. A closeup look allows a direct comparison between mean scattering signal and the attenuation, where the crack is not detected.

9.4 Discussion

Although CTS is very common, there is no generally accepted and concise diagnostic tool available. Currently applied methods often rely on the reproduction of symptoms, which leaves much space for ambiguities and interpretation by the practicians. Other imaging tools such as x-ray radiography rely on attenuation as contrast source which in turn strongly depends on the atomic number as well as the material density. Even though x-rays easily penetrate teeth, radiographs only detect the average attenuation coefficient along the beam direction while losing all in-depth information. More detailed information is retrieved by three-dimensional methods such as cone-beam computed tomography (CBCT) or XDT, which was used in this ex-vivo study. As can be seen in

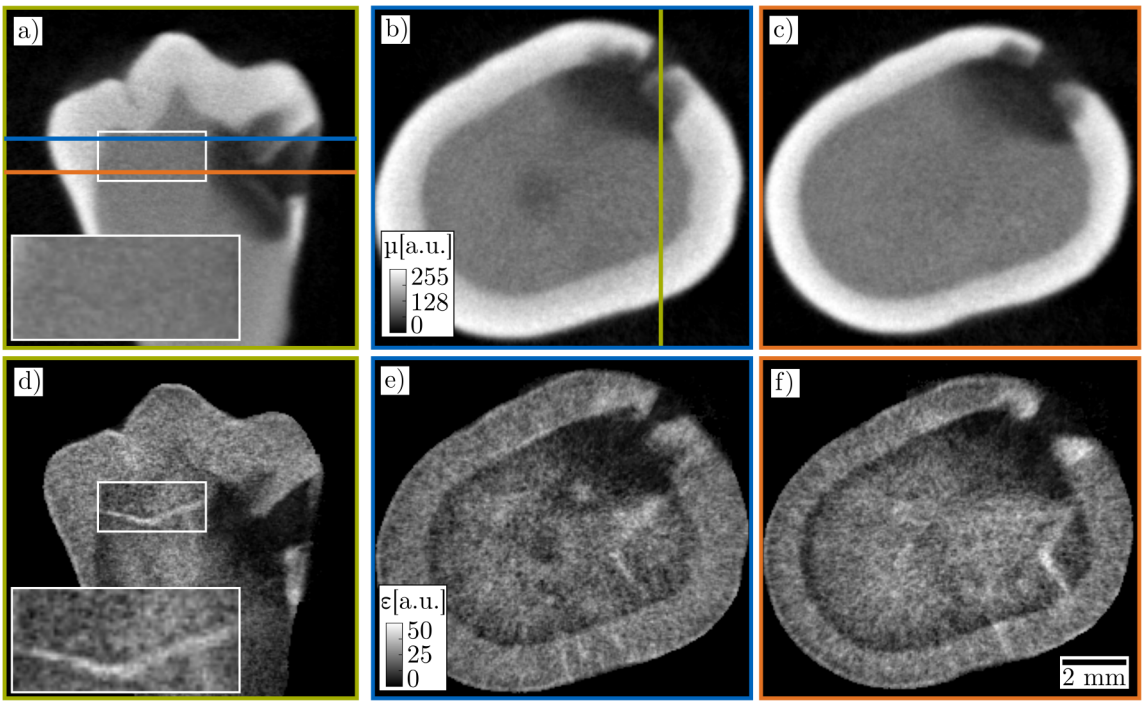

Figure 9.4: **Attenuation and mean scattering signal for a carious tooth.** Attenuation and mean scattering signal for a carious tooth. In the first row, a sagittal slice (a) and two axial slices (b-c) show a cavity in the enamel as well as the carious region within the dentin. The scattering signal (d-e) allows to identify those regions as well but additionally detects a crack (magnified region and white arrows). In the attenuation images, the crack is not visible.

Fig. 9.2, the attenuation reconstruction allows to distinguish between enamel, dentin and the pulp chamber due to their different density and material composition. Tooth cracks, however, dont change the intrinsic tooth structure but only cause a translocation. In projection geometry, such changes are only visible if the view is well aligned to the crack direction, which cant be assumed in general. In three-dimensional reconstructions, the crack detection depends upon the spatial resolution, which is limited to about 80m for some imaging systems [Tanimoto, 2009]. In Fig. 9.2, the reconstruction had a voxel size of (40 ± 3)µm, giving a lower limit to the spatial resolution. This allowed to identify several tooth cracks such as the one indicated by a white arrow in Fig. 9.2 b). The corresponding line-plot L2 shows a decrease of the attenuation signal, which is clear since the density decreases in the crack region. However, it is impossible to detect microcracks with a size smaller than the resolution such as the microcracks indicated by green arrows. XDT measures the mean scattering signal in addition to the attenuation, which is sensitive to gradients in electron density. As those gradients are especially high at boundaries between different materials, the mean scattering signal is well suited to detect morphological sample changes instead of material composition. Hence, the signal in a single voxel represents the mean isotropic scattering averaged over the spatial resolution. The origin of the scattering signal, however, may be structures that can be one order of magnitude smaller than the spatial resolution. The signal is thereby most sensitive to features comparable to the setup autocorrelation length, which is given by setup-specific parameters and in this study was lower than 2.5 µm [Prade, 2015]. This enables detection of microscopical structure changes including microcracks without directly resolving them. Since the morphology rapidly changes in a crack region, a strong scattering signal is detected for cracks on top of a relatively low background, as visible in Fig. 9.2, where the mean scattering signal allows to detect additional microcracks with respect to the attenuation signal. This explains the difference between both contrast modalities in the line-plots in Fig. 9.2 f-g), where the scattering signal has much higher visibilities of 78% and 93% compared to the attenuation signal with visibilities of 9% and 11%. If compromises regarding spatial resolution have to be made due to the increased specimens size, no microcracks are detected at all in the attenuation signal. Nevertheless, they remain still visible in the mean scattering signal. This is especially well depicted in Fig. 9.4 a) and d), where a region of interest shows a close-up view of the tooth crack. Figure 9.3 shows a typical tooth structure resulting from a root canal treatment (RCT). Part of the tooth crown is covered with composite material, the rest has been filled with glass ionomer cement (GIC). Its attenuation of $\mu = 129 \pm 5$ is quite similar to the attenuation of enamel ($\mu = 116 \pm 4$). However, they are easily distinguishable in the mean scattering strength contrast modality with a higher value of $\epsilon = 29 \pm 8$ for GIC compared to a value of $\epsilon = 10 \pm 3$ for enamel. For other materials such as enamel and dentin, the best contrast is provided by the attenuation signal whereas the mean scattering

provides no contrast, highlighting the complementarity of both contrast modalities. The sample presented in Fig. 9.4 suffered from dental caries, which caused a smooth surface cavity. As the disease progresses in the enamel, the surface region remains relatively well-mineralized [Hinds, 1942]. This can be seen in Fig. 9.4 b) and c), where the enamel surface has a higher attenuation coefficient close to the surface compared to the inner part. In the mean scattering signal, there is no difference between the surface and the inner part, which suggests that demineralization does not lead to an increased scattering signal. In the dentin region, the caries infection progresses through the dentinal tubules towards the pulp chamber, leading to the triangular shape visible in Fig. 9.4. In contrast to the enamel, dentin reacts to dental caries infection by the formation of sclerotic dentin. This reduces the size of the dentinal tubules with mineral materials from odontoblasts, which reduces the number of interfaces in the dentin and ultimately leads to a decreased scattering signal. In contrast to symptom reproducers, XDT provides in-depth information and does not rely on the subjective interpretation of a practitioner. Moreover, it can detect both large-scale cracks in the simultaneously reconstructed attenuation signal and microcracks in the scattering signal. Thermography and transillumination methods are capable to detect microscopic cracks as well but they do not provide three-dimensional information. Hence, they might miss cracks in certain cases. In addition, thermography relies upon the heat production due to friction within microcracks, which makes it difficult to detect larger cracks which in turn would require an additional imaging method [MatsushitaTokugawa, 2013].

However, several limitations must be overcome in order to apply XDT in clinical practice. Until now, the reconstruction algorithm requires sample projections from many different orientations, leading to a complex acquisition scheme and long acquisition times of several hours. In a future in-vivo application, the potential sample orientations would be limited which could be compensated by using prior knowledge about the sample. Moreover, the dose of this proof of principle study is not yet compatible to clinical dose levels. Dose-compatible measurements have been made already for other applications such as mammography or in-vivo lung imaging of pigs [Scherer, 2015b; Gromann, 2017]. In conclusion, we provided evidence in this ex-vivo study that XDT potentially is a powerful tool for the diagnosis of CTS. The simultaneous acquisition of both attenuation and scattering information provides complementary information, highlighting both the overall tooth structure and its morphology. Thereby, the mean scattering signal senses signals originating from structures one order of magnitude smaller than the imaging system resolution. Thus, it can detect tooth microcracks which are oblique in the attenuation signal. This could provide an evidence-based diagnosis tool for CTS already in an early stage and consequently help to reduce symptoms as well as increase treatment options.

10 Conclusion

In conclusion, this thesis provided a first step towards clinical applications of directional dark-field imaging. The theoretical foundations, implementation of a dedicated experimental setup and the experimental results are presented.

In chapter 2, a brief introduction of the interactions of x-rays with matter was given. This thesis mainly exploits additional contrast given by grating interferometry. Accordingly, grating-based phase-contrast imaging was introduced in chapter 4. The phase-stepping procedure and the signal extraction of attenuation, differential phase-contrast, and dark-field were described. A connection between the dark-field and small-angle x-ray scattering (SAXS) was sketched and motivated the possibility of direction-sensitive measurements. In two dimensions, x-ray vector radiography (XVR) was introduced in chapter 5. Using a simple phantom sample, the additional information given by the mean scattering, degree of anisotropy and direction of scattering was presented.

Chapter 3 investigated different ways to produce x-rays. In addition to conventional X-ray tubes and synchrotron sources, novel concepts such as liquid metal jet sources and Compact Light Sources (CLS) were highlighted. An emphasis was thereby on the Munich Compact Light Source (MuCLS), the first commercially sold CLS. It uses the principle of inverse Compton Scattering for the production of x-rays and is hence not subject to the same limitations as target-based sources. The source properties were derived from first principles and motivated the source design.

The high spatial coherence at the MuCLS compared to conventional x-ray tubes allowed the implementation of a simplified x-ray grating interferometer. Its design considerations were discussed in chapter 6. The interferometer performance was analyzed by means of the stepping curve visibility, and by a simulation study.

The grating interferometer was subsequently used to investigate bone microstructures. An *ex-vivo* human hand was scanned in chapter 7 to show the feasibility of this technique for extended samples in a realistic setting. Using XVR, we could provide evidence that additional image information is obtained by analyzing directional scattering information. For this sample, the degree of anisotropy was of particular diagnostic value since it was strongly influenced by changes in the trabecular microstructure. Thus, isotropic structures near the epiphysis could be easily distinguished from a more anisotropic structure in the diaphysis. This gave a hint that x-ray scattering might be a suitable tool for the detection of fine bone fractures, which are typically occult

on conventional x-ray radiographs. This hypothesis was tested in chapter 8 using an *ex-vivo* porcine rib model. We could demonstrate, for a limited number of samples, that microcracks not visible in the conventional attenuation lead to an increased mean scattering signal.

Another biological tissue was investigated in the last part of this thesis. Similar to the bone samples, the aim was to detect microscopic structural changes not visible in the attenuation signal. We provided evidence that x-ray dark-field tomography (XDT) is potentially a powerful tool for the diagnosis of the cracked-tooth syndrome (CTS). The simultaneous acquisition of both attenuation and scattering information provided complementary information, highlighting both the overall tooth structure and its morphology. Thereby, the mean scattering signal originating from structures one order of magnitude smaller than the imaging system resolution. Thus, it can detect tooth microcracks which are oblique in the attenuation signal.

Outlook

This thesis showed in proof-of principle studies that directional dark-field imaging could be potentially applied for medical imaging applications. On its way towards clinical applications, the applied dose is certainly one of the main challanges. As discussed in the previous chapters, an optimized setup should reduce the total exposure time applied to the sample to a minimum. This should be done either by decreasing the number of sample orientations or by reducing the exposure time. The aim of a future study should be to find an optimal solution for this tradeoff. Moreover, the number of phase-steps should be optimized. Using rotation-invariant information from attenuation to simultaneously reconstruct both the attenuation and the dark-field could also help to reduce the dose. The current studies were conducted on a limited number of samples. Therefore, a reader study including a larger amount of samples could show the added diagnostic value in a statistically relevant way.

For the measurements of human teeth, a large amount of different sample orientations were required. In the current form, an application for clinical imaging seems out of reach. However, a future setup could implement an acquisition scheme which does not aim to reconstruct fully three-dimensional imformation, but performs a task-based optimization of the acquisition scheme.

Bibliography

[AbouRass, 1983] Abou-Rass, M. Crack lines: the precursors of tooth fractures - their diagnosis and treatment. *Quintessence international, dental digest* **14,** 437–47 (1983) (Cited on pages 77, 78).

[Alberts, 2014] Alberts, B., Bray, D., Hopkin, K., Johnson, A. & Lewis, J. *Impact of adaptivity on the behavior of networks of workstations under bursty traffic* 4th ed. (CRC Press Inc., Boca Raton, 2014) (Cited on page 77).

[AlsNielsen, 2011] Als-Nielsen, J. & McMorrow, D. *Elements of Modern X-ray Physics* 2nd ed. (John Wiley & Sons, Ltd, Chichester, UK, 2011) (Cited on pages 5–7, 9–14, 16, 22, 27, 28).

[Andersson, 2008] Andersson, R., Van Heijkamp, L. F., De Schepper, I. M. & Bouwman, W. G. Analysis of spin-echo small-angle neutron scattering measurements. *Journal of Applied Crystallography* **41,** 868–885 (2008) (Cited on page 27).

[Attwood, 2016] Attwood, D. & Sakdinawat, A. *X-Rays and Extreme Ultraviolet Radiation* (Cambridge University Press, Cambridge, 2016) (Cited on page 5).

[Bacher, 1995] Bacher, W., Menz, W. & Mohr, J. The LIGA technique and its potential for microsystems-a survey. *IEEE Transactions on Industrial Electronics* **42,** 431–441 (1995) (Cited on page 41).

[Bader, 2008] Bader, J. D., Martin, J. A. & Shugars, D. A. Incidence rates for complete cusp fracture. *Community Dentistry and Oral Epidemiology* **29,** 346–353 (2008) (Cited on page 77).

[Bader, 1996] Bader, J. D., Shugars, D. A. & Roberson, T. M. Using crowns to prevent tooth fracture. *Community Dentistry and Oral Epidemiology* **24,** 47–51 (1996) (Cited on page 77).

[Baum, 2015] Baum, T. *et al.* X-ray dark-field vector radiography - A novel technique for osteoporosis imaging. *Journal of Computer Assisted Tomography* **39,** 286–289 (2015) (Cited on pages 2, 33, 63).

[Bech, 2009] Bech, M. *X-ray imaging with a grating interferometer* PhD thesis (University of Copenhagen, 2009) (Cited on pages 24–26, 33, 43, 44, 51).

[Becker, 1986] Becker, E., Ehrfeld, W., Hagmann, P., Maner, A. & Münchmeyer, D. Fabrication of microstructures with high aspect ratios and great structural heights by synchrotron radiation lithography, galvanoforming, and plastic moulding (LIGA process). *Microelectronic Engineering* **4,** 35–56 (1986) (Cited on page 41).

[Bennett, 2010] Bennett, E. E., Kopace, R., Stein, A. F. & Wen, H. A grating-based single-shot x-ray phase contrast and diffraction method for in vivo imaging. *Medical Physics* **37,** 6047–6054 (2010) (Cited on page 63).

[Berger, 2010] Berger, M. *et al. XCOM: Photon Cross Section Database (version 1.5) Available: http://physics.nist.gov/xcom* 2010 (Cited on page 67).

[Bille, 2002] Bille, J. & Schlegel, W. *Medizinische Physik 2* (eds Schlegel, W. & Bille, J.) (Springer Berlin Heidelberg, Berlin, Heidelberg, 2002) (Cited on page 66).

[Birnbacher, 2016] Birnbacher, L. *et al.* Experimental Realisation of High-sensitivity Laboratory X-ray Grating-based Phase-contrast Computed Tomography. *Scientific Reports* **6,** 24022 (2016) (Cited on page 40).

[Bonse, 1965] Bonse, U. & Hart, M. An X-ray Interferometer. *Applied Physics Letters* **6,** 155–156 (1965) (Cited on pages 2, 21).

[Braig, 2018] Braig, E.-M. *et al.* Simultaneous wood and metal particle detection on dark-field radiography. *European Radiology Experimental* **2,** 1 (2018) (Cited on page 76).

[Buhr, 2012] Buhr, H., Büermann, L., Gerlach, M., Krumrey, M. & Rabus, H. Measurement of the mass energy-absorption coefficient of air for x-rays in the range from 3 to 60 keV. *Physics in Medicine and Biology* **57,** 8231–8247 (2012) (Cited on page 67).

[Burger, 2017] Burger, K. *et al.* Increased cell survival and cytogenetic integrity by spatial dose redistribution at a compact synchrotron X-ray source. *PLOS ONE* **12** (ed Woloschak, G. E.) e0186005 (2017) (Cited on page 39).

[Buzug, 2008] Buzug, T. M. *Computed Tomography* (Springer Berlin Heidelberg, Berlin, Heidelberg, 2008) (Cited on pages 5, 6).

[Cameron, 1964] Cameron, C. E. Cracked-tooth syndrome. *The Journal of the American Dental Association* **68,** 405–411 (1964) (Cited on page 77).

[Cameron, 1976] Cameron, C. E. The cracked tooth syndrome: additional findings. *The Journal of the American Dental Association* **93,** 971–975 (1976) (Cited on page 77).

[Chapman, 1997] Chapman, D. *et al.* Diffraction enhanced x-ray imaging. *Physics in Medicine and Biology* **42,** 2015–2025 (1997) (Cited on page 21).

[Chi, 2017] Chi, Z. *et al.* Recent progress of phase-contrast imaging at Tsinghua Thomson-scattering X-ray source. *Nuclear Instruments and Methods in Physics Research Section B: Beam Interactions with Materials and Atoms* **402,** 364–369 (2017) (Cited on page 14).

[Culjat, 2005] Culjat, M. O. *et al.* Ultrasound crack detection in a simulated human tooth. *Dentomaxillofacial Radiology* **34,** 80–85 (2005) (Cited on page 78).

[Davis, 1995] Davis, T. J., Gao, D., Gureyev, T. E., Stevenson, A. W. & Wilkins, S. W. Phase-contrast imaging of weakly absorbing materials using hard X-rays. *Nature* **373,** 595–598 (1995) (Cited on page 21).

[De Marco, 2015] De Marco, F. & Pfeiffer, F. *Optimizing data processing for grating-based X-ray phase-contrast computed tomography* PhD thesis (Technical University of Munich, 2015), 109 (Cited on page 51).

[Diemoz, 2017] Diemoz, P. C. *et al.* Single-Shot X-Ray Phase-Contrast Computed Tomography with Nonmicrofocal Laboratory Sources. *Physical Review Applied* **7,** 044029 (2017) (Cited on page 76).

[Eakle, 1986] Eakle, W. S., Maxwell, E. H. & Braly, B. V. Fractures of posterior teeth in adults. *Journal of the American Dental Association (1939)* **112,** 215–218 (1986) (Cited on page 77).

[Eggl, 2017] Eggl, E. *Biomedical X-ray Imaging at the Munich Compact Light Source* PhD thesis (Technical University of Munich, 2017) (Cited on page 40).

[Eggl, 2018] Eggl, E. *et al.* Dose-compatible grating-based phase-contrast mammography on mastectomy specimens using a compact synchrotron source. *Scientific Reports* **8,** 15700 (2018) (Cited on page 39).

[Eggl, 2017] Eggl, E. *et al.* Mono-Energy Coronary Angiography with a Compact Synchrotron Source. *Scientific Reports* **7,** 42211 (2017) (Cited on page 39).

[Eggl, 2015] Eggl, E. *et al.* Prediction of Vertebral Failure Load by Using X-Ray Vector Radiographic Imaging. EN. *Radiology* **275,** 553–561 (2015) (Cited on pages 2, 33, 56, 63, 65, 73, 75).

[Eggl, 2016] Eggl, E. *et al.* The Munich Compact Light Source: initial performance measures. *Journal of Synchrotron Radiation* **23,** 91–100 (2016) (Cited on pages 9, 19).

[Fratzl, 1997] Fratzl, P., Jakob, H. F., Rinnerthaler, S., Roschger, P. & Klaushofer, K. Position-Resolved Small-Angle X-ray Scattering of Complex Biological Materials. *Journal of Applied Crystallography* **30,** 765–769 (1997) (Cited on pages 2, 21).

[Geurtsen, 1999] Geurtsen, W. & García-Godoy, F. Bonded restorations for the prevention and treatment of the cracked-tooth syndrome. *American journal of dentistry* **12,** 266–70 (1999) (Cited on page 77).

[Gradl, 2018] Gradl, R. *et al.* In vivo Dynamic Phase-Contrast X-ray Imaging using a Compact Light Source. *Scientific Reports* **8,** 6788 (2018) (Cited on page 39).

[Gradl, 2017] Gradl, R. *et al.* Propagation-based Phase-Contrast X-ray Imaging at a Compact Light Source. *Scientific Reports* **7,** 4908 (2017) (Cited on page 39).

[Gromann, 2017] Gromann, L. B. *et al.* In-vivo X-ray Dark-Field Chest Radiography of a Pig. *Scientific Reports* **7,** 4807 (2017) (Cited on pages 55, 76, 86).

[Hemberg, 2003] Hemberg, O., Otendal, M. & Hertz, H. M. Liquid-metal-jet anode electron-impact x-ray source. *Applied Physics Letters* **83,** 1483–1485 (2003) (Cited on page 12).

[Hetterich, 2017] Hetterich, H. *et al.* Dark-field imaging in coronary atherosclerosis. *European Journal of Radiology* **94,** 38–45 (2017) (Cited on page 55).

[Hiatt, 1973] Hiatt, W. H. Incomplete Crown-Root Fracture in Pulpal-Periodontal Disease. *Journal of Periodontology* **44,** 369–379 (1973) (Cited on pages 77, 78).

[Hinds, 1942] Hinds, E. Resistance of Enamel to Dental Caries. *Journal of Dental Research* **21,** 475–479 (1942) (Cited on page 86).

[Huang, 1998] Huang, Z. & Ruth, R. Laser-Electron Storage Ring. *Physical Review Letters* **80,** 976–979 (1998) (Cited on pages 1, 14).

[Imai, 2012] Imai, K., Shimada, Y., Sadr, A., Sumi, Y. & Tagami, J. Noninvasive cross-sectional visualization of enamel cracks by optical coherence tomography in vitro. *Journal of Endodontics* **38,** 1269–1274 (2012) (Cited on page 78).

[Iwanenko, 1944] Iwanenko, D. & Pomeranchuk, I. On the Maximal Energy Attainable in a Betatron. *Physical Review* **65,** 343–343 (1944) (Cited on page 12).

[Jensen, 2010a] Jensen, T. H. *et al.* Directional x-ray dark-field imaging of strongly ordered systems. *Physical Review B* **82,** 214103 (2010) (Cited on pages 33, 56).

[Jensen, 2010b] Jensen, T. H. *et al.* Directional x-ray dark-field imaging. *Physics in Medicine and Biology* **55,** 3317–3323 (2010) (Cited on pages 2, 33, 56).

[Jud, 2016] Jud, C. *et al.* Dentinal tubules revealed with X-ray tensor tomography. *Dental Materials* **32,** 1189–1195 (2016) (Cited on page 78).

[Jud, 2017] Jud, C. *et al.* Trabecular bone anisotropy imaging with a compact laser-undulator synchrotron x-ray source. *Scientific Reports* **7,** 14477 (2017) (Cited on pages 55, 65, 74).

[Jud, 2018a] Jud, C. *et al.* X-ray Dark-Field Tomography Reveals Tooth Cracks. *in preparation* (2018) (Cited on page 77).

[Jud, 2018b] Jud, C. *et al.* X-ray Vector Radiography Reveals Bone Microfractures: Demonstration using Ex-Vivo Porcine Rib Model. *IEEE Transactions on Medical Imaging, submitted* (2018) (Cited on page 65).

[Jun, 2016] Jun, M. K. *et al.* Detection and analysis of enamel cracks by quantitative light-induced fluorescence technology. *Journal of Endodontics* **42,** 500–504 (2016) (Cited on page 77).

[Kagias, 2016] Kagias, M. *et al.* Single shot x-ray phase contrast imaging using a direct conversion microstrip detector with single photon sensitivity. *Applied Physics Letters* **108,** 234102 (2016) (Cited on page 63).

[Kalyan Chakravarthy, 2012] Kalyan Chakravarthy, P. V., Telang, L. A., Nerali, J. & Telang, A. Cracked Tooth: A Report of Two Cases and Role of Cone Beam Computed Tomography in Diagnosis. *Case Reports in Dentistry* **2012** (ed Patterson, R. L.) 1–6 (2012) (Cited on page 78).

[Klein, 1929] Klein, O. & Nishina, Y. Über die Streuung von Strahlung durch freie Elektronen nach der neuen relativistischen Quantendynamik von Dirac. *Zeitschrift für Physik* **52,** 853–868 (1929) (Cited on page 7).

[Kuroda, 2011] Kuroda, R. *et al.* Quasi-monochromatic hard X-ray source via laser Compton scattering and its application. *Nuclear Instruments and Methods in Physics Research Section A: Accelerators, Spectrometers, Detectors and Associated Equipment* **637,** S183–S186 (2011) (Cited on page 14).

[Lauridsen, 2014] Lauridsen, T., Lauridsen, E. M. & Feidenhans'l, R. Mapping misoriented fibers using X-ray dark field tomography. *Applied Physics A* **115,** 741–745 (2014) (Cited on page 56).

[Loewen, 2003] Loewen, R. J. *A Compact Light Source: Design and Technical Feasibility Study of a Laser-Electron Storage Ring X-Ray Source* PhD thesis (Stanford University, 2003) (Cited on pages 14, 19).

[Lynch, 2002] Lynch, C. D. & McConnell, R. J. The cracked tooth syndrome. *Journal (Canadian Dental Association)* **68,** 470–5 (2002) (Cited on page 77).

[Lynch, 2011] Lynch, S. K. *et al.* Interpretation of dark-field contrast and particle-size selectivity in grating interferometers. *Applied Optics* **50,** 4310 (2011) (Cited on pages 26, 29).

[Malecki, 2013] Malecki, A. *et al.* Coherent Superposition in Grating-Based Directional Dark-Field Imaging. *PLoS ONE* **8** (ed Patterson, R. L.) e61268 (2013) (Cited on pages 2, 33, 34, 56, 66).

[Malecki, 2014] Malecki, A. *et al.* X-ray tensor tomography. *Epl* **105,** 38002 (2014) (Cited on pages 35, 78).

[Marschner, 2016] Marschner, M. *et al.* Helical X-ray phase-contrast computed tomography without phase stepping. *Scientific Reports* **6,** 23953 (2016) (Cited on page 51).

[MatsushitaTokugawa, 2013] Matsushita-Tokugawa, M. *et al.* Detection of Dentinal Microcracks Using Infrared Thermography. *Journal of Endodontics* **39,** 88–91 (2013) (Cited on pages 78, 86).

[Miao, 2016] Miao, H. *et al.* A universal moiré effect and application in X-ray phase-contrast imaging. *Nature Physics* **12,** 830–834 (2016) (Cited on page 63).

[Miao, 2015] Miao, H. *et al.* Enhancing Tabletop X-Ray Phase Contrast Imaging with Nano-Fabrication. en. *Scientific Reports* **5,** 13581 (2015) (Cited on page 63).

[Mohr, 2012] Mohr, J. *et al. High aspect ratio gratings for X-ray phase contrast imaging* in *AIP Conference Proceedings* **1466** (2012), 41–50 (Cited on page 41).

[Momose, 2003] Momose, A. *et al.* Demonstration of X-Ray Talbot Interferometry. *Japanese Journal of Applied Physics* **42,** L866–L868 (2003) (Cited on pages 21, 22).

[Nobel Prize, 1901] Nobelprize.org. Nobel Media AB 2014. *The Nobel Prize in Physics 1901* <http://www.nobelprize.org/nobel_prizes/physics/laureates/1901/> (1901) (Cited on page 1).

[Olivo, 2013] Olivo, A. *et al.* Low-dose phase contrast mammography with conventional x-ray sources. *Medical Physics* **40,** 090701 (2013) (Cited on page 76).

[Paganin, 2002] Paganin, D., Mayo, S. C., Gureyev, T. E., Miller, P. R. & Wilkins, S. W. Simultaneous phase and amplitude extraction from a single defocused image of a homogeneous object. *Journal of Microscopy* **206,** 33–40 (2002) (Cited on page 21).

[Paganin, 2006] Paganin, D. M. *Coherent x-ray optics* 411 (Oxford University Press, 2006) (Cited on page 44).

[Pfeiffer, 2006] Pfeiffer, F., Weitkamp, T., Bunk, O. & David, C. Phase retrieval and differential phase-contrast imaging with low-brilliance X-ray sources. *Nature Physics* **2,** 258–261 (2006) (Cited on pages 2, 21).

[Pfeiffer, 2008] Pfeiffer, F. *et al.* Hard-X-ray dark-field imaging using a grating interferometer. *Nature Materials* **7,** 134–137 (2008) (Cited on pages 2, 21, 26).

[Pogorelsky, 2016] Pogorelsky, I. in, 133–138 (Springer, Cham, 2016) (Cited on page 14).

[Potdevin, 2012] Potdevin, G. *et al.* X-ray vector radiography for bone micro-architecture diagnostics. *Physics in Medicine and Biology* **57,** 3451–3461 (2012) (Cited on pages 2, 33, 56).

[Prade, 2015] Prade, F., Yaroshenko, A., Herzen, J. & Pfeiffer, F. Short-range order in mesoscale systems probed by X-ray grating interferometry. *Epl* **112,** 68002 (2015) (Cited on pages 27, 79, 85).

[Revol, 2012] Revol, V., Kottler, C., Kaufmann, R., Neels, A. & Dommann, A. Orientation-selective X-ray dark field imaging of ordered systems. *Journal of Applied Physics* **112,** 114903 (2012) (Cited on pages 2, 33, 34, 56, 66).

[Roh, 2006] Roh, B. D. & Lee, Y. E. Analysis of 154 cases of teeth with cracks. *Dental Traumatology* **22,** 118–123 (2006) (Cited on page 77).

[Schaff, 2015a] Schaff, F. *et al.* Correlation of X-Ray Vector Radiography to Bone Micro-Architecture. *Scientific Reports* **4,** 3695 (2015) (Cited on pages 3, 33, 56, 65, 73, 75).

[Schaff, 2015b] Schaff, F. *et al.* Six-dimensional real and reciprocal space small-angle X-ray scattering tomography. *Nature* **527,** 353–356 (2015) (Cited on page 2).

[Scherer, 2015a] Scherer, K. *et al.* Non-invasive Differentiation of Kidney Stone Types using X-ray Dark-Field Radiography. *Scientific Reports* **5,** 9527 (2015) (Cited on page 55).

[Scherer, 2015b] Scherer, K. *et al.* Toward clinically compatible phase-contrast mammography. *PLoS ONE* **10** (ed Orgel, J. P.) e0130776 (2015) (Cited on pages 55, 63, 76, 86).

[Schoonjans, 2011] Schoonjans, T. *et al.* The xraylib library for X-ray-matter interactions. Recent developments. *Spectrochimica Acta - Part B Atomic Spectroscopy* **66,** 776–784 (2011) (Cited on page 67).

[Sharma, 2017] Sharma, Y., Schaff, F., Wieczorek, M., Pfeiffer, F. & Lasser, T. Design of Acquisition Schemes and Setup Geometry for Anisotropic X-ray Dark-Field Tomography (AXDT). *Scientific Reports* **7,** 3195 (2017) (Cited on pages 78, 80).

[Slaton, 2003] Slaton, C. C. *et al.* Identification of resected root-end dentinal cracks: A comparative study of visual magnification. *Journal of Endodontics* **29,** 519–522 (2003) (Cited on page 77).

[Stampanoni, 2011] Stampanoni, M. *et al.* The first analysis and clinical evaluation of native breast tissue using differential phase-contrast mammography. *Investigative Radiology* **46,** 801–806 (2011) (Cited on page 55).

[Standring, 2008] Standring, S. *et al. Gray's Anatomy* 40th ed. (Elsevier, 2008) (Cited on page 62).

[Stelljes, 2016] Stelljes, I. *Roentgendiagnostik: Haeufigkeit und Strahlenexposition* <http://www.bfs.de/DE/themen/ion/anwendung-medizin/diagnostik/roentgen/haeufigkeit-exposition.html> (2016) (Cited on page 55).

[Stepanek, 1998] Stepanek, J. Parametric study of laser Compton-backscattering from free relativistic electrons. *Nuclear Instruments and Methods in Physics Research Section A: Accelerators, Spectrometers, Detectors and Associated Equipment* **412,** 174–182 (1998) (Cited on page 16).

[Strobl, 2014] Strobl, M. General solution for quantitative dark-field contrast imaging with grating interferometers. en. *Scientific Reports* **4,** 7243 (2014) (Cited on pages 2, 21, 26–29, 31).

[Strobl, 2008] Strobl, M. *et al.* Neutron dark-field tomography. *Physical Review Letters* **101** (2008) (Cited on page 33).

[Sun, 2011] Sun, C. & Wu, Y. K. Theoretical and simulation studies of characteristics of a Compton light source. *Physical Review Special Topics - Accelerators and Beams* **14,** 044701 (2011) (Cited on page 15).

[Talbot, 1836] Talbot, H. LXXVI. ¡i¿Facts relating to optical science. No. IV¡/i¿. *Philosophical Magazine Series 3* **9,** 401–407 (1836) (Cited on pages 2, 21, 22).

[Talim, 1974] Talim, S. T. & Gohil, K. S. Management of coronal fractures of permanent posterior teeth. *The Journal of Prosthetic Dentistry* **31,** 172–178 (1974) (Cited on page 77).

[Tanaka, 2013] Tanaka, J. *et al.* Cadaveric and in vivo human joint imaging based on differential phase contrast by X-ray Talbot-Lau interferometry. *Zeitschrift fur Medizinische Physik* **23,** 222–227 (2013) (Cited on pages 55, 65).

[Tang, 2009] Tang, C. *et al.* Tsinghua Thomson scattering X-ray source. *Nuclear Instruments and Methods in Physics Research Section A: Accelerators, Spectrometers, Detectors and Associated Equipment* **608,** S70–S74 (2009) (Cited on page 14).

[Tanimoto, 2009] Tanimoto, H. & Arai, Y. The effect of voxel size on image reconstruction in cone-beam computed tomography. *Oral Radiology* **25,** 149–153 (2009) (Cited on pages 78, 85).

[Thüring, 2013a] Thüring, T. *et al.* Energy resolved X-ray grating interferometry. *Applied Physics Letters* **102,** 191113 (2013) (Cited on pages 63, 76).

[Thüring, 2013b] Thüring, T. *et al.* Human hand radiography using X-ray differential phase contrast combined with dark-field imaging. *Skeletal Radiol.* **42,** 827–35 (2013) (Cited on page 55).

[Variola, 2011] Variola, A. *The ThomX Project* in *2nd International Particle Accelerator Conference (IPAC'11)* (2011), 1903–1905 (Cited on page 14).

[Variola, 2014] Variola, A., Haissinski, J., Loulergue, A. & Zomer, F. *ThomX Technical Design Report* tech. rep. (2014) (Cited on page 14).

[Wei, 2006] Wei, C. J. *et al.* Systematic analysis of missed extremity fractures in emergency radiology. *Acta Radiologica* **47,** 710–717 (2006) (Cited on page 55).

[Weitkamp, 2006] Weitkamp, T., David, C., Kottler, C., Bunk, O. & Pfeiffer, F. *Tomography with grating interferometers at low-brilliance sources* in *SPIE Optics + Photonics* (ed Bonse, U.) (International Society for Optics and Photonics, 2006), 63180S (Cited on pages 23, 40, 80).

[Weitkamp, 2005] Weitkamp, T. *et al.* X-ray phase imaging with a grating interferometer. *Optics Express* **13,** 6296 (2005) (Cited on pages 2, 21).

[Wen, 2013] Wen, H. *et al.* Subnanoradian X-ray phase-contrast imaging using a far-field interferometer of nanometric phase gratings. *Nature Communications* **4,** 2659 (2013) (Cited on page 63).

[Wen, 2010] Wen, H. H., Bennett, E. E., Kopace, R., Stein, A. F. & Pai, V. Single-shot x-ray differential phase-contrast and diffraction imaging using two-dimensional transmission gratings. *Optics Letters* **35,** 1932 (2010) (Cited on pages 63, 76).

[Wieczorek, 2016] Wieczorek, M., Schaff, F., Pfeiffer, F. & Lasser, T. Anisotropic X-Ray Dark-Field Tomography: A Continuous Model and its Discretization. *Physical Review Letters* **117,** 158101 (2016) (Cited on pages 78, 80).

[Willer, 2018] Willer, K. *et al.* X-ray dark-field imaging of the human lung - A feasibility study on a deceased body. *PLOS ONE* **13** (ed Nolan, A.) e0204565 (2018) (Cited on pages 55, 76).

[Willmott, 2011] Willmott, P. *An Introduction to Synchrotron Radiation* (John Wiley & Sons, Ltd, Chichester, UK, 2011) (Cited on page 5).

[Wolf, 2015] Wolf, J. *et al.* Lens-term- and edge-effect in X-ray grating interferometry. *Biomedical Optics Express* **6,** 4812 (2015) (Cited on pages 26, 35).

[Yang, 2012] Yang, Y. & Tang, X. The second-order differential phase contrast and its retrieval for imaging with x-ray Talbot interferometry. *Medical Physics* **39,** 7237–7253 (2012) (Cited on page 26).

[Yaroshenko, 2013] Yaroshenko, A. *et al.* Pulmonary Emphysema Diagnosis with a Preclinical Small-Animal X-ray Dark-Field Scatter-Contrast Scanner. *Radiology* **269,** 427–433 (2013) (Cited on page 55).

[Yashiro, 2015a] Yashiro, W. & Momose, A. Effects of unresolvable edges in grating-based X-ray differential phase imaging. *Optics Express* **23,** 9233 (2015) (Cited on page 26).

[Yashiro, 2015b] Yashiro, W., Vagovič, P. & Momose, A. Effect of beam hardening on a visibility-contrast image obtained by X-ray grating interferometry. EN. *Optics Express* **23,** 23462 (2015) (Cited on page 26).

[Yashiro, 2011a] Yashiro, W. *et al.* Distribution of unresolvable anisotropic microstructures revealed in visibility-contrast images using x-ray Talbot interferometry. *Physical Review B - Condensed Matter and Materials Physics* **84,** 094106 (2011) (Cited on page 26).

[Yashiro, 2011b] Yashiro, W. *et al. Microstructure Analysis Using Visibility Contrast in X-ray Talbot Interferometry* in *AIP Conference Proceedings* **1365** (2011), 321–324 (Cited on pages 2, 21, 26, 33).

List of Figures

List of Tables

Publications and Scientific Presentations

Publications as first author

Jud, C., Schaff, F., Zanette, I., Wolf, J., Fehringer, A. & Pfeiffer, F. Dentinal tubules revealed with X-ray tensor tomography. *Dental Materials* **32**, 1189-1195 (2016)

Jud, C., Braig, E., Dierolf, M., Eggl, E., Günther, B, Achterhold, K., Gleich, B., Rummeny, E., Noël, P., Pfeiffer, F. & Muenzel, D. Trabecular bone anisotropy imaging with a compact laser-undulator synchrotron source. *Scientific Reports* **7**, 14477 (2017)

Jud, C., Dierolf, M., Günther, B., Achterhold, K., Gleich, B., Rummeny, E, Pfeiffer, F. & Pfeiffer, D. X-ray Vector Radiography Reveals Bone Microfractures: Demonstration Using Ex-Vivo Procine Rib Model. *submitted to IEEE Transactions on Medical Imaging*

Jud, C., Sharma, Y., Günther, B., Weitz, J., Pfeiffer, F. & Pfeiffer, D. X-ray Dark-Field Tomography Reveals Tooth Cracks. *manuscript in preparation*

Publications as co-author

Schaff, F., Bech, M., Zaslansky, P., **Jud, C.**, Liebi, M., Guizar-Sicairos, M. & Pfeiffer, F. Six-dimensional real and reciprocal space small-angle X-ray scattering tomography. *Nature* **527**, 353-356 (2015)

Vogel, J., Schaff, F., Fehringer, A., , **Jud, C.**, Wieczorek, M., Pfeiffer, F. & Lasser, T. Constrained X-ray tensor tomography reconstruction. *Optics Express* **23**, 15134-15151 (2015)

Eggl, E., Dierolf, M., Achterhold, K., **Jud, C.**, Günther, B., Braig, E., Gleich, B. & Pfeiffer, F. The Munich Compact Light Source: Initial performance measures. *Journal of synchrotron Radiation* **23**, 91-100 (2016)

Eggl, E., Grandl, S., Sztrókay-Gul, A., Dierolf, M., **Jud, C.**, Heck, L., Burger, K., Günther, B., Achterhold, K., Mayr, D., Wilkens, J.J., Auweter, S.D., Gleich, B., Hellerhoff, K., Reiser, M. F., Pfeiffer, F. & Herzen, J. Dose-compatible grating-based phase-contrast mammography on mastectomy specimens using a compact synchrotron source. *Scientific Reports* **8**, 15700 (2018)

Gradl, R., Morgan, K.S., Dierolf, M., **Jud, C.**, Hehn, L., Günther, B., Moller, W., Kutschke, D., Yang, L., Stoeger, T., Pfeiffer, D., Gleich, B., Achterhold, K., Schmid, O., & Pfeiffer, F. Dynamic in vivo chest x-ray dark-field imaging in mice. *accepted in IEEE Transactions on Medical Imaging*

Wieczorek, M., Schaff, F., **Jud, C.**, Pfeiffer, D., Pfeiffer, F. & Lasser, T. Brain Connectivity Exposed by Anisotropic X-ray Dark-field Tomography. *Scientific Reports* **8**, 14345 (2018)

Hehn, L., Gradl, R., Andrej, V., Günther, B., Dierolf, M., **Jud, C.**, Willer, K., Allner, S., Hammel, J.U., Hessler, R., Morgan, K.S., Herzen, J., Hemmert, W. & Pfeiffer, F. Propagation-based phase-contrast tomography of a guinea pig inner ear with cochlear implant using a model-based iterative reconstruction algorithm. *Biomedical Optics Express* **9**, 5530 (2018)

Braig, E., Böhm, J., Dierolf, M., **Jud, C.**, Günther, B., , Mechlem, K., Allner, S., Sellerer, T., Achterhold, K., Gleich, B., Noël, P., Pfeiffer, D., Rummeny, E., Herzen, J. & Pfeiffer, F. Direct quantitative material decomposition employing grating-based X-ray phase-contrast CT. *Scientific Reports* **8**, 16394 (2018)

Günther, B., Hehn, L., **Jud, C.**, Hipp, A., Dierolf, M. & Pfeiffer, F. Full-Field Structured-Illumination Super-Resolution X-ray Transmission Microscopy. *under Review in Nature Communications*

Heck, L., Dierolf, M., **Jud, C.**, Eggl, E., Sellerer, T., Mechlem, K., Günther, B., Achterhold, K., Gleich, B., Metz, S., Pfeiffer, D., Noël, P., Pfeiffer, F. & Herzen, J. Contrast-enhanced Spectral Mammography with a Compact Synchrotron Source. *manuscript in preparation*

Oral presentations

Dentinal tubules revealed with X-ray Tensor Tomography, *X-ray and Neutron Phase Imaging with Gratings (XNPIG), Bethesda, USA, September 2015*

Dentinal tubules revealed with X-ray Tensor Tomography, *BioMedical Applications for X-ray Phase Contrast Imaging (IMXP), Garmisch-Patenkirchen, Germany, January 2016*

Trabecular bone anisotropy imaging with a compact laser-undulator synchrotron x-ray source, *BioMedical Applications for X-ray Phase Contrast Imaging (IMXP), Garmisch-Patenkirchen, Germany, January 2017*

X-ray Vector Radiography of Fractured Bones, *BioMedical Applications for X-ray Phase Contrast Imaging (IMXP), Garmisch-Patenkirchen, Germany, January 2018*

Poster presentations

Trabecular bone anisotropy imaging with a compact laser-undulator synchrotron x-ray source, *The international society for optics and photonics (SPIE). Medical Imaging, Orlando, USA, February 2017*

Acknowledgements

This work was only possible with the help of many people. I would like to thank...

- Franz Pfeiffer for giving me the opportunity to work on this PhD topic. Your lecture on Biomedical Physics and your passion to bring phase-contrast imaging towards a clinical application were truly inspiring. Being part of the very first installation of a commercially sold compact synchrotron was a unique experience I am very grateful for.
- Daniela Pfeiffer for closely supporting all my projects. Your medical expertise and advice made my projects in this form possible in the first place.
- Florian Schaff for introducing me to this chair and the field of directional dark-field imaging.
- Tobial Lasser and the whole directional dark-field group, namely Yash Sharma, Mathias Wieczorek, and Florian Schaff. Our meetings provided a very fruitful environment and pushed me further in my work.
- Elena Eggl for the nice collaboration in building the setup, especially for designing the grating interferometer and helping to get it stable.
- Klaus Achterhold and Nelly De Leiris for helping me with all my administrative stuff.
- Elena Eggl and Lorenz Birnbacher for helping me to get the human samples.
- Danays Kunka, Pascal Meyer and Jürgen Mohr from the Karlsruhe Nano Micro Facility at KIT for the excellent optical gratings.
- The Virtual institute, for the nice meetings and fruitful discussions as well as the PhD meeting.
- Lyncean Technologies Inc. for the technical support of the MuCLS both remotely and during the regular service-visits.
- Benedikt Günther for running and maintaining the MuCLS together with Martin Dierolf. Without your effort, many experiments would not have been possible.

- Martin Dierolf, Lorenz Birnbacher, Florian Schaff, and Mark Müller for proof-reading this thesis.
- Martin Dierolf for his restless support in keeping literally everything running. Your detailed knowledge about the MuCLS is one main reason it is functional most of the time and becoming more and more user-friendly. The extensive proof-reading of my publications and this thesis were extremely helpful, the discussions during our MuCLS-meetings helped me to set the right goals. Your continued support and advice have been indispensable to this work.
- All people who keep our nice IT-infrastructure up and running.
- The whole MuCLS-team for their professional and moral support.
- The whole group for providing this nice working atmosphere. Especially Stefan for the enjoyable table-kicker matches, Regine for keeping up the motivation to work out, and all people that contributed to our cooking events.

Lastly, I want to thank my friends and my family for their priceless support during my studies and for always being there for me.